Structural Dynamics of the Calmodulin-Ryanodine Receptor Interaction Using Bifunctional Spin Labels and EPR

A DISSERTATION
SUBMITTED TO THE FACULTY OF THE GRADUATE SCHOOL
OF THE UNIVERSITY OF MINNESOTA
BY

Cheng Her

IN PARTIAL FULFILLMENT OF THE REQUIREMENTS
FOR THE DEGREE OF
DOCTOR OF PHILOSOPHY

David D. Thomas, Advisor

August 2018

ACKNOWLEDGEMENTS

Throughout these past few years I have been very fortunate to work alongside many exceptional and talented people. Without a doubt, the work here could not have been completed without all the support, guidance and assistance I have received.

I would first like to extend my sincerest gratitude to my thesis advisor **Dr. David Thomas**. His commitment to mentorship is unparalleled, and I will always remember the countless hours he put into guiding and supporting me in my research projects. Dave, thank you for always being patient with me, for allowing me to be a part of this wonderful family you have created, and for raising me well these last five years.

Next, I would like to thank my committee members: **Dr. John Lipscomb, Dr. Joe Metzger and Dr. Dawn Lowe**. Thank you for all your support and guidance throughout the years, and for agreeing to stick with me until the very end.

To the greatest peptide chemist alive, **Dr. Christine Karim**, thank you for all that you have taught me, and for always being there when I needed moral and emotional support. I will always see you as a role model and aspire to be as wise as you.

To two of the world's greatest EPR spectroscopists, **Dr. Andrew Thompson** and **Dr. Jesse McCaffrey**, thank you for all that you have taught me. Physics is not my strength, so thank you for always being patient with me whenever I had questions, and for explaining complicated answers in ways that are (relatively) easy to understand. I feel very fortunate that you two were around to help me in my projects. Those papers would not have been published without your help, so thank you.

To two of the world's leading experts in ryanodine receptors, **Dr. Robyn Rebbeck** and **Dr. Razvan Cornea**, huge thanks to you both for all the insightful discussions throughout the years. Also thank you so much for leading the RyR group!

To **Octavian Cornea**, our lab administrator, thank you for being the backbone of the lab, and for helping everyone with their papers and grant applications! Also, thank you for being a great friend to me and everyone else. Your cheerful and casual personality make you a fun person to have conversations with.

To **Sarah Blakely** and **Destiny Ziebol**, our lab managers, thank you so much for your assistance in everything. For sure, the lab would collapse without you two around.

Last but not least, I would like to thank everyone else in the DDT Lab for helping maintain a supportive and positive environment throughout the years. I would not have done my graduate research anywhere else, so thank you.

DEDICATION

To my family: Dad, Mom, Tswj Fwm, Sue, Xong, Tong, Moha, Xai and Johnny.
Thanks for all your support and love.

And to Nou.
For helping me get this far.

ABSTRACT

Muscle contraction and relaxation are regulated by changes in intracellular calcium levels. To facilitate muscle contraction, calcium is released from the intracellular calcium reservoir into the cytosol by the homotetrameric calcium channel known as the ryanodine receptor (RyR). The sarcoplasmic reticulum membrane-embedded RyR is a target for many small molecule and protein modulators, including the ubiquitously expressed calcium binding protein calmodulin (CaM). CaM can bind four calcium ions via its four EF-hand motifs and has calcium-dependent effects on RyR. It is well established that CaM potentiates channel opening below μM calcium and inhibition above μM calcium. Despite this, the structural mechanism of the calcium-dependent CaM-mediated RyR regulation remain poorly understood.

The primary goal of the work presented here is to elucidate the structural mechanisms of the CaM-RyR interaction, using bifunctional spin labels and electron paramagnetic resonance (EPR). In the first study, we investigated the structural dynamics of a spin labeled ryanodine receptor peptide (RyRp) bound to CaM using EPR (Chapter 4). By detecting the rotational dynamics of specific sites along the backbone, we show that the interaction of RyRp with CaM is non-uniform along the peptide, and the primary effect of calcium is to increase the interaction of the N-lobe of CaM with RyRp. In the second study (Chapter 5), we placed spin probes on both CaM and RyRp and investigated the calcium-dependent structural changes of the complex using a distance measurement EPR technique known as double electron-electron resonance (DEER). Our

DEER distance results provide support for the conformational selection mechanism of CaM binding to RyRp (i.e. the binding of RyRp shifts CaM to pre-existing structural states). We discovered differential Ca effects on the two lobes of CaM with respect to RyRp binding. More specifically, we discovered that Ca was required for complete interaction of the N-lobe with RyRp, while the C-lobe bound RyRp independent of Ca. These findings are consistent with results from Chapter 4 and provide support for the hypothesis that CaM functions as a subunit of RyR through binding of the C-lobe, and complete interaction of the N-lobe of CaM (in response to increased cytosolic Ca levels) is responsible for maximum inhibition of RyR. Thus, our results provide novel insight into the structural mechanism of CaM-mediated RyR regulation while showcasing an innovative approach with wide applicability to other biological systems.

TABLE OF CONTENTS

LIST OF TABLES

LIST OF FIGURES

LIST OF EQUATIONS

LIST OF ABBREVIATIONS

Å	Angstrom
Abu	α-amino-n-butyric acid
apoCaM	Ca-free calmodulin
B	magnetic field strength
BSL	3,4-bis-(methanethiosulfonyl-methyl)-2,2,5,5-tetramethyl -2,5-dihydro-1h-pyrrol 1-yloxy spin label
CaM	calmodulin
Ca	calcium ion (+2 charge)
CaCaM	Ca-saturated calmodulin
CaMKII	calcium/calmodulin-dependent protein kinase II
CD	circular dichroism
CryoEM	Cryo-electron microscopy
CW-EPR	continuous wave electron paramagnetic resonance
DEER	double electron-electron resonance
DHPR	dihydropyridine receptor
DTT	dithiothreitol
E	energy
EC	excitation-contraction
EGTA	ethylene glycol tetraacetic acid
EPR	electron paramagnetic resonance
ESI-MS	electron spray ionization mass spectrometry
Fmoc	fluoroenylmethyloxycarbonyl
FRET	fluorescence resonance energy transfer
FWHM	full width at half maximum
g_e	electron g factor
HEPES	4-(2-hydroxyethyl)-1-piperazineethanesulfonic acid
HPLC	high performance liquid chromatography
IASL	iodoacetamide spin label
I_{Ca}	L-type calcium channel
IPTG	isopropyl thiogalactose
K_d	dissociation constant
kDa	kiloDaltons
mlck	myosin light chain kinase
MOPS	3-morpholinopropane-1-sulfonic acid
MSL	maleimide spin label
MTSL	methanethiosulfonate spin label
NCX	Na-Ca exchanger
NMR	nuclear magnetic resonance
NOE	Nuclear Overhauser effect
PKA	protein kinase A
PLB	phospholamban
RyR	ryanodine receptor
RyRp	peptide corresponding to CaM-binding site on RyR1 (3614-3643)

S	order parameter
SDS	sodium dodecyl sulfate
SERCA	sarco(endo)plasmic reticulum calcium adenosine triphosphatase
SPPS	solid phase peptide synthesis
SR	sarcoplasmic reticulum
ST-EPR	saturation transfer EPR
T	hyperfine splitting constant
TFA	trifluoroacetic acid
TFE	2,2,2-trifluoroethanol
TM	transmembrane
TOAC	2,2,6,6-tetramethyl-N-oxyl-4-amino-4-carboxylic acid
Δ_L	low field linewidth
μ_β	Bohr magneton
σ	standard devieation
μ	magnetic dipole moment
ν	radiation frequency
τ_R	rotational correlation time

CHAPTER 1: CALCIUM-REGULATED MUSCLE PHYSIOLOGY

1.1 ROLE OF CALCIUM IN MUSCLE FUNCTION

The processes of muscle contraction and relaxation at the cellular level are highly complex and tightly regulated. Muscle contraction is primarily governed by excitation-contraction (EC) coupling, which is generally defined as a physiological phenomenon that converts an electrical stimulus into a mechanical response. In this case, an action

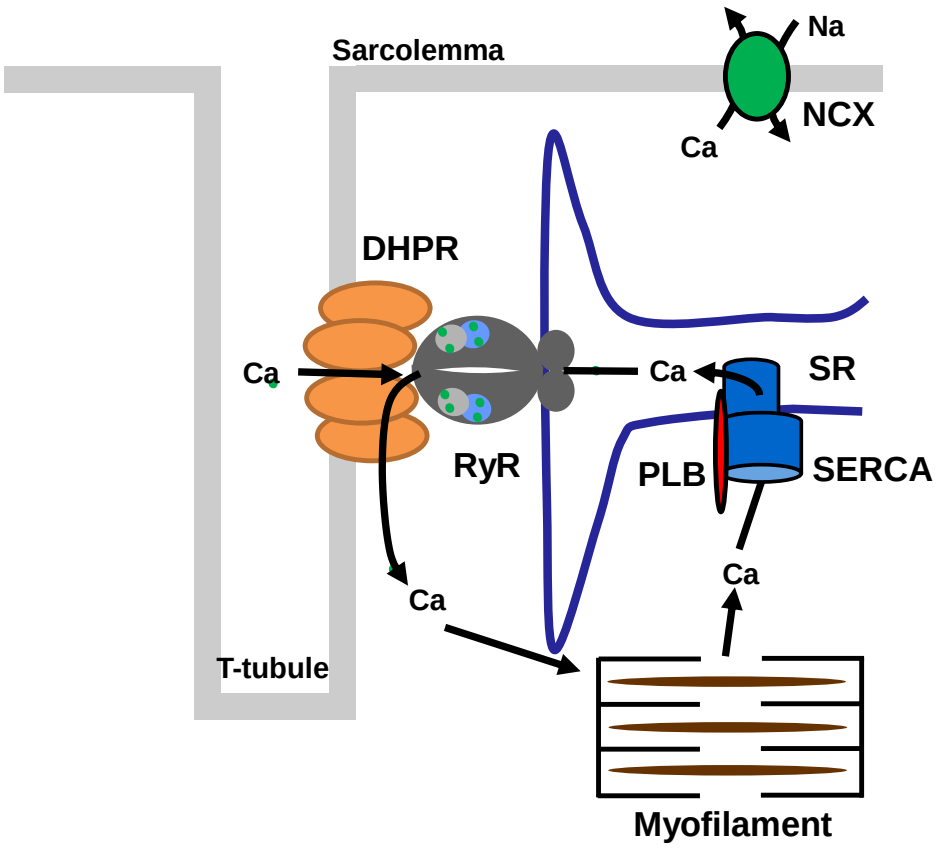

Fig. 1. Diagram of intracellular Ca transport. Ca transported through the L-type calcium channels (DHPR in figure) during action potential activates sarcoplasmic reticulum (SR) membrane-bound ryanodine receptors (RyR), which in turn releases Ca from the SR the cytosol. Increased cytosolic Ca levels stimulate contraction at the myofilaments. To facilitate muscle relaxation, calcium is taken back into the SR by the calcium ATPase SERCA, which is regulated by PLB or removed out of the cell by the Na-Ca exchanger (NCX).

potential (electrical signal) depolarizes the sarcolemma of muscle cells eventually leading to muscle contraction at the myofilaments (mechanical response). Fig. 1 is a diagram showing the essential players in intracellular calcium transport, more specifically, those involved in excitation contraction coupling (see section 1.2). The role of Ca is to bridge the two processes: depolarization of the sarcolemma eventually leads to Ca release via the ryanodine receptor (RyR) from the intracellular Ca storage organelle, the sarcoplasmic reticulum (SR), into the cytosol where they bind and induce contraction at the myofilaments. Thus, increased cytosolic Ca concentration is associated with the contractile state of muscle. In order for relaxation to occur, cytosolic Ca must be decreased. This process is predominantly achieved by pumping Ca back into the SR or out of the cell, by the SR membrane-embedded protein pump sarcoendoplasmic reticulum Ca-ATPase (SERCA) and Na-Ca exchanger (NCX), respectively. Remarkably, SERCA alone is responsible for about 70% of the Ca removed from the cytosol in human [1]. Thus, calcium homeostasis is crucial and mishandling of Ca can lead to harmful and very often deadly heart and muscle conditions.

1.2 EXCITATION-CONTRACTION COUPLING

As mentioned in section 1.1, the process of EC coupling comprises a series of events leading up to muscle contraction (Fig. 1). The process begins when an electrical impulse from an associated motor neuron depolarizes the sarcolemma, activating membrane-bound voltage-gated Ca channels known as dihydropyridine receptors (DHPR) or L-type Ca channels (I_{Ca}). In both skeletal and cardiac muscle tissues, the downstream effect of membrane depolarization is the rapid efflux of Ca from the SR, but

their mechanism varies. In skeletal muscle, the DHPR is physically coupled to RyR, and membrane depolarization causes a conformational change in the DHPR that is allosterically coupled to the opening of the channel. In cardiac muscle, RyR activation is instead induced by a small but significant influx of Ca from the extracellular environment through the DHPR causing opening of RyR in a process known as calcium-induced calcium release. Ca diffuses to the myofilament where they bind and induce contraction. The myofilament apparatus, consisting of myosin, actin and the tropomyosin-troponin complex, is the contractile unit responsible for force generation of the myocyte. In the relaxed state, the myosin-actin interface is blocked by the tropomyosin-troponin complex. Ca binding to troponin relieves this and triggers mechanical contraction as the myosin binds and generates force onto the thin filaments.

CHAPTER 2: REGULATION OF THE RYANODINE RECEPTOR BY CALMODULIN

2.1 CALMODULIN: STRUCTURE, FUNCTION, AND DISEASE

Many extracellular signals are relayed into intracellular responses through an increase in the cytosolic Ca levels. Elevated cytosolic Ca concentration leads to binding of Ca by regulatory proteins, which in turn activate a wide variety of intracellular processes by interacting with downstream targets. One of these regulators is calmodulin (CaM, Fig. 2), a ubiquitously expressed 16.7 kDa, 148 amino acid protein that regulate many crucial cellular pathways in eukaryotes such as gene transcription, apoptosis, metabolism, neurotransmitter secretion, myofilament contraction and many others [2]. CaM can bind to its targets when not bound to Ca (apoCaM), bound to Ca (CaCaM), or constitutively at both low and high Ca concentrations.

The binding of Ca drastically alters the conformation of CaM. Solution NMR and X-ray crystallography studies have shown that CaM consists of two similar globular terminal lobes termed the N- and C-lobes which are connected by a central flexible linker (Fig. 2) [5, 3, 6-8]. Each domain contains two EF-hand motifs, each capable of binding

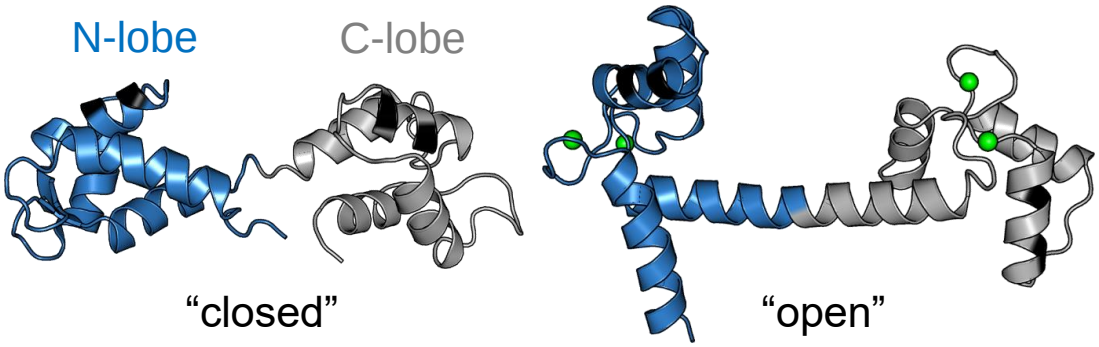

Fig. 2. Ribbon diagram representation of CaM. Structures of apoCaM (left) and CaCaM (right) were determined from NMR and x-ray crystallography, respectively [3, 4]. Ca ions are shown as green spheres.

one Ca ion with the C-lobe having approximately 10-fold higher affinity than the N-lobe [9]. In the classical picture, apoCaM exists in the “closed” state where the central linker is partially unfolded and the N- and C-lobes are collapsed towards the center [4]. Binding of four Ca at each of the EF-hands induces a large conformational change resulting in the “open” state of CaM in which the central linker becomes folded and the two lobes are spaced far apart [3]. As a consequence of this structural rearrangement, methionine-rich hydrophobic patches are exposed on each domain of CaM that promote binding to a wide array of targets.

NMR studies in solution have shown that CaM is a remarkably dynamic protein both in the presence and absence of Ca. ^{15}N NMR relaxation experiments and analysis of inter-residue NOE signals indicate that the central linker (residues 76 to 80) between the two terminal domains of CaM exhibit high flexibility, suggesting that the two domains tumble independently in solution [10, 6, 4]. This hypothesis is further supported by NMR residual dipolar coupling experiments which demonstrate that the N- and C-lobes have different anisotropies [8], and molecular dynamics (MD) simulations which demonstrate that the central linker undergoes drastic bending and unfolding motions, such that the two terminal lobes experience significant variations in the inter-domain distances and angles [11, 12].

The essential role of CaM as a Ca sensor has been well established for over half a century and both structural and biochemical data have provided insight into the mechanism by which it mediates the activity of downstream targets. Classically, the function of CaM is thought to involve Ca-dependent activation of Ca/CaM protein kinases where an increase in cytosolic Ca concentrations induces a conformational

change in CaM that allow it to bind to an auto-inhibitory region of these kinases and thereby activate them [13]. More recently, studies have demonstrated an equally important role for CaM in regulating the activity of ion channels. Unlike the Ca-dependent activation of the protein kinases, both apoCaM and CaCaM can bind and regulate ion channels.

2.2 THE RYANODINE RECEPTOR

The main calcium channel in the SR of skeletal and cardiac muscle is the RyR (Fig. 3), named after the plant alkaloid ryanodine to which it binds with high affinity. There are three main mammalian isoforms, with RyR1 and RyR2 being highly expressed in the skeletal and cardiac tissues, respectively. RyR3 is variably expressed in different tissues but was first discovered in the brain. RyR1 and RyR2 are responsible for the release of Ca from the SR into the cytoplasm following an action potential in skeletal and cardiac tissues, respectively, while RyR3 is essential to various neuronal functions. RyR is a homo-tetramer consisting of four subunits of ~560 kDa each, making it the largest known ion channel. The subunits form a quadrilateral around a central pore, creating a passage for Ca ions to flow through. RyR is embedded in the SR membrane, with approximately 80% of the protein in the cytoplasmic side (Fig. 3).

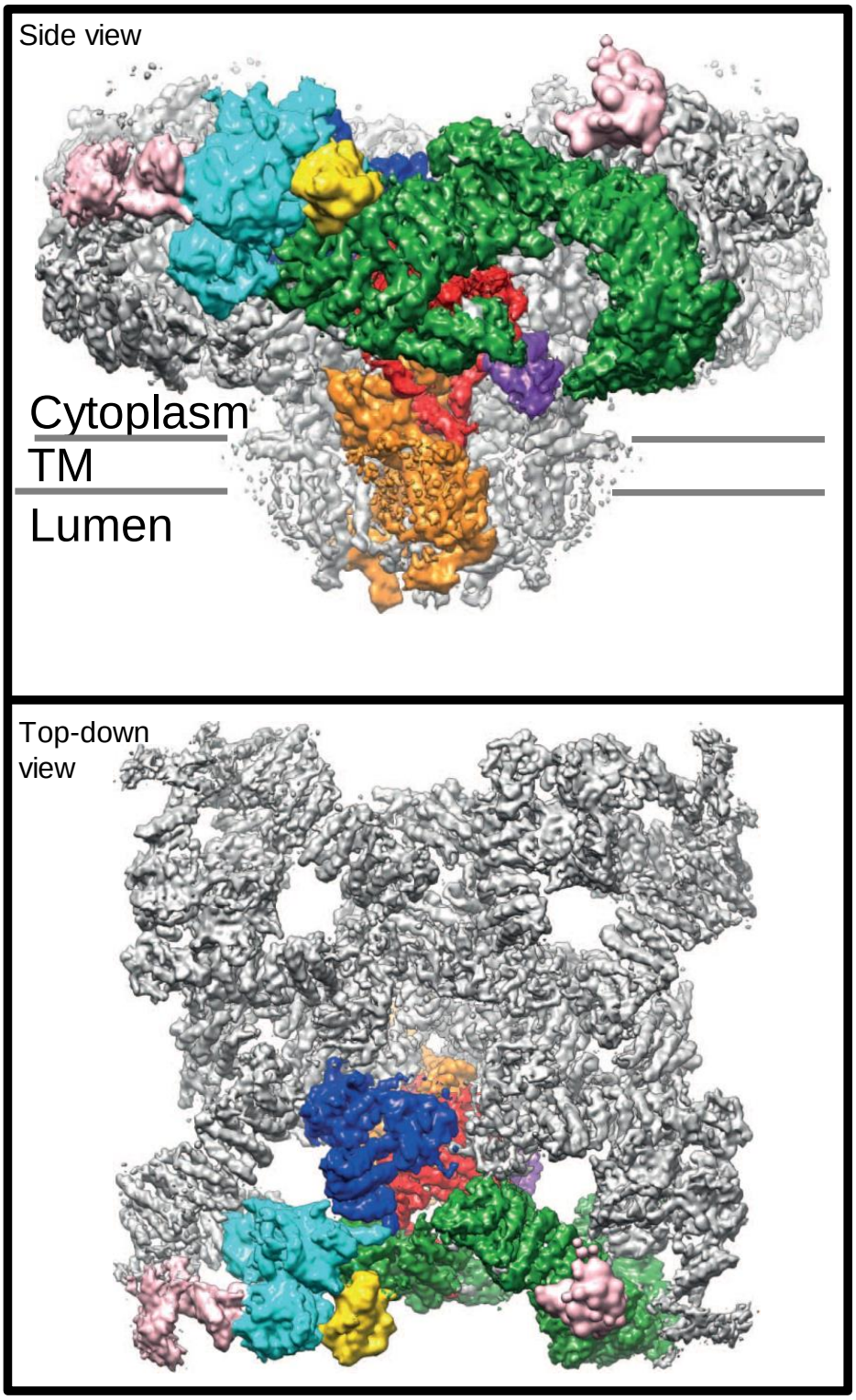

Fig. 3. CryoEM reconstruction of the intact mammalian skeletal ryanodine receptor at 4.8 Å resolution [14]. The colored regions depict different domains of a single protomer. Side view (top panel) reveals that most of the channel is located on the cytosolic side. Top-down view (bottom panel) shows how four protomers are oriented to form a functioning channel.

The structure of the intact ryanodine receptor was first investigated over a decade ago using cryo-electron microscopy (cryoEM) to a resolution of approximately 10 Å [15-17]. Since then, advances in the field of cryoEM have allowed the structure of RyR to be resolved to an remarkably improved resolution of below 4.8 Å (Fig. 3) [14, 18, 19]. These cryoEM maps reveal a large cytoplasmic region embedded into the SR membrane through a much smaller transmembrane domain. Many cellular agents and modulators interact with the cytoplasmic side of the channel, translating them to opening or closing of the small channel pore region. Such modulators include CaM, FKBP, FKBP12.6, CaM kinases, PKA and others.

2.3 CALMODULIN-MEDIATED RYANODINE RECEPTOR REGULATION

The DHPR and RyR channels are both regulated by other proteins that function as secondary modulators of EC-coupling. Of particular relevance and interest is CaM, which is capable of binding and regulating both the DHPR and RyR channels at low and high cytoplasmic Ca levels. CaM binds to the skeletal RyR with high affinity both in the presence and absence of Ca [20, 21]. Investigations involving [^{35}S]CaM revealed a single high-affinity CaM-binding site per RyR1 protomer [22-24], and cryoEM reconstruction shows that CaM binds within a cleft near the cytoplasmic face of the channel [15]. Measurements of SR Ca flux, ryanodine binding assays and single channel recordings have shown that CaM binding on RyR1 has opposite effects on channel activity: at low Ca levels CaM has an activating effect on RyR1, while at high Ca, CaM functions as an inhibitor [25, 21, 26]. The presence of CaM mainly shift the Ca-dependence of RyR1 activity towards a lower concentration such that RyR1 activates and inactivates at a lower

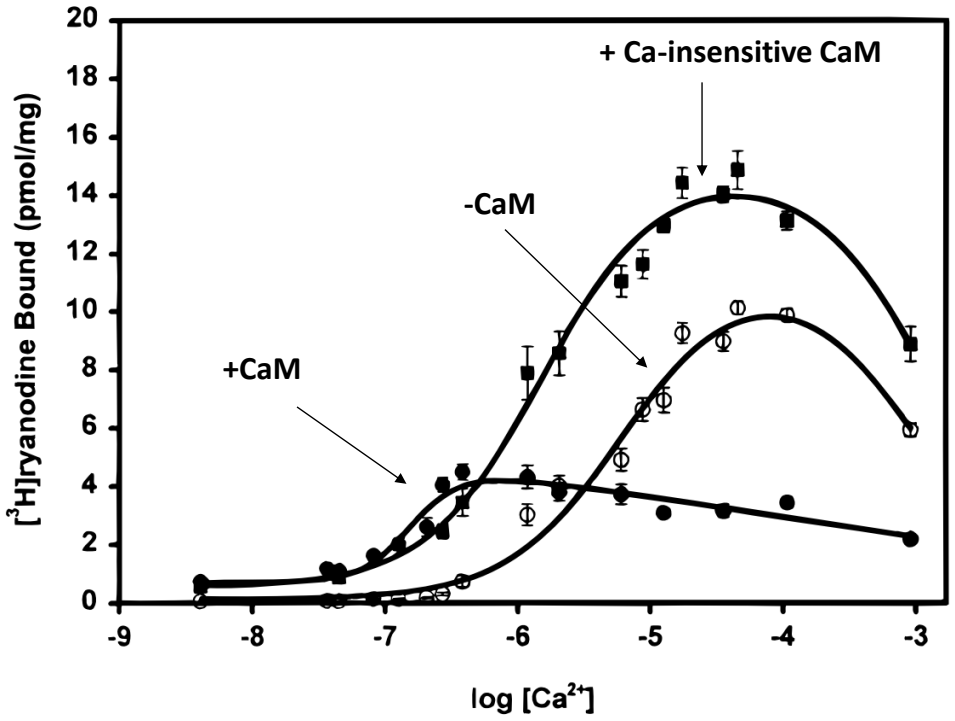

Fig. 4. The effect of CaM on the Ca-dependence of RyR1 activity. The activity of RyR1 in the absence (open circles) or presence (closed circles) of CaM was measured by detecting the amount of bound [^{3}H]ryanodine, which has been shown to bind preferentially to the open state of the channel [27]. Figure adapted from [28].

Ca concentration than in the absence of CaM (Fig. 4). CaM-bound RyR1 opens and closes at physiological Ca levels associated with muscle contraction, thus CaM functions effectively as a feedback regulator of Ca levels making RyR1 more sensitive to Ca. Results from kinetics studies suggest that CaM may be constitutively bound to RyR throughout the EC-coupling process, as the dissociation rates of apoCaM and CaCaM are slower than the time-scale of a muscle contraction event [21].

As mentioned earlier, cryoEM studies and experiments utilizing [^{35}S]CaM have shown that one CaM binds per subunit of RyR at all Ca concentrations. It has also been shown that the binding sites of apoCaM and CaCaM are distinct but overlapping and located in a cleft in the cytoplasmic region [15]. A high-affinity CaM-binding site on RyR1 was identified by tryptic digestion and peptide mapping [22, 28, 29]. It has been

discovered that both apoCaM and CaCaM was able to protect the same residues (R3630 and R3637) from proteolytic cleavage, suggesting that this region contained the CaM-binding site both in the presence and absence of Ca [22]. Subsequent studies of CaM binding to various synthetic peptides derived from sequences around the R3630 and R3637 region revealed that a peptide corresponding to the 3614-3643 on RyR1 (RyRp) interacted with both apoCaM and CaCaM with high affinity [29]. Additionally, the affinities of CaM for RyRp and the intact RyR channel are comparable, furthering suggesting that this site corresponds to the main primary binding site for CaM. Furthermore, mutagenesis experiments involving point mutations within the 3614-3643 region affected CaM's regulation of RyR at low and high Ca concentration [31, 32]. More specifically, the mutation F3636A resulted in inhibition of RyR1 by CaM at low Ca (instead of activation), and W3620A resulted in decreased CaCaM binding and inhibition of the channel. Lastly, the 3614-3643 site of RyR1 is extremely well conserved across various vertebrates and isoforms (**Fig. 5**), further solidifying this site of RyR1 as a high-affinity binding site for apoCaM and CaCaM.

Fig. 5. Sequence alignment of mammalian RyR1 at the 3614-3643 site and several other homologs. The proposed CaM-binding site 3614-3643 in RyR1 is extremely conserved across human, rat and zebrafish, and human RyR2 and RyR3 sequences. Residues that are identical in at least four sequences are bolded. Figure reprinted from [30].

The interaction of RyRp with CaM was further investigated by NMR and x-ray crystallography. In a 2006 paper [30], Maximciuc et al. reported the crystal structure of CaCaM in complex with RyRp to a resolution of 2.0 Å (Fig. 6). In this structure, the two lobes of CaM makes contact with the helical RyRp, embracing it in a "compact" conformation with respect to the lobe separation. They also discovered residues in the RyRp sequence crucial to the interaction with CaM, including W3620 and F3636, which forms a "1-17" hydrophobic anchor for each of the CaM lobes to bind [30]. These are the same residues that were previously found to affect CaM's ability to regulate RyR1 in mutagenesis experiments [31, 32]. Interestingly, the two lobes comes together to adopt a compact conformation but do not come close enough to physically make contact with one another as with the case of other CaM/target peptide structures such as that of CaM

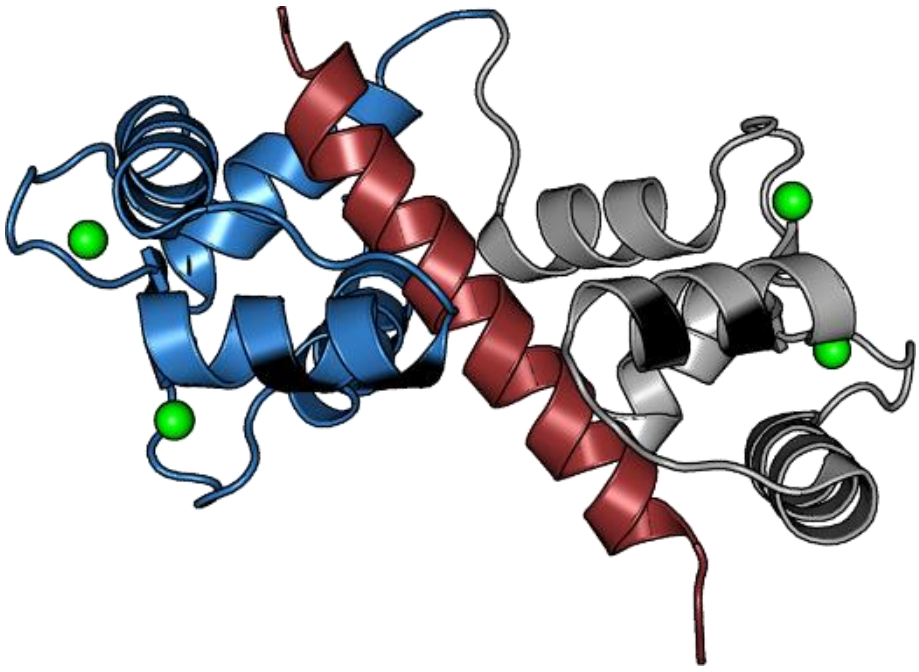

Fig. 6. Crystal structure of CaCaM in complex with RyRp at 2.0 Å resolution. The structure reveals that the N-lobe (blue) and C-lobe (gray) of CaM are brought in together by RyRp (maroon) to adopt a "compact" structure. Ca ions are shown as green sphere. Figure adapted from [30].

bound to myosin light chain kinase peptide [33]. Consistent with this, NMR relaxation and residual dipolar coupling experiments confirm the existence of the crystal structure in solution but also reveal significant domain motion [30].

CHAPTER 3: ELECTRON PARAMAGNETIC RESONANCE

3.1 SITE-DIRECTED SPIN LABELING

Electron paramagnetic resonance (EPR) is a spectroscopic technique utilized for measuring the structure, dynamics and local environment of proteins and molecules through a stable unpaired electron. EPR detects the absorption of microwave radiation by the sample at specific resonances. Since most naturally occurring proteins lack a free radical, a spin label containing an unpaired electron must be attached to the protein in order to make it EPR-active in a process known as site-directed spin labeling (SDSL). Spin labels typically consist of five or six membered rings with a nitroxide bond containing the unpaired electron in a p-orbital (Fig. 7). Typically, the SDSL method requires cysteines for site-specific attachment of the spin labels. Therefore, any native cysteines in a protein of interest must be mutated to another amino acid, usually alanine, using site-directed mutagenesis to prevent unspecific attachment of the spin label. The most widely used spin labels are thiol reactive (Fig. 7), thus cysteine must be introduced at site of interest in a protein for SDSL. It must be noted that the mutated protein should maintain its function and structural integrity, which can be easily checked with an activity assay and circular dichroism experiment, respectively. With the case of monofunctionally attached spin labels (MSL, MTSSL, IASL) this is usually less of a concern since only one cysteine is needed. These monofunctionally attached spin labels often are limited in their accuracy and precision of measuring protein structures and dynamics because of their flexible linkage. As will be discussed later in Section 3.5, these limitations of monofunctional spin labels can be virtually eliminated by using bifunctionally attached spin labels (TOAC and BSL).

3.2 PRINCIPLES OF EPR

Every types of spectroscopic techniques fundamentally rely on detecting the absorption of energy by the sample of interest. For example, UV/Vis spectroscopy relies on excited electronic states and infrared spectroscopy on infrared radiation. EPR utilizes microwave frequencies to flip the spin states of unpaired electrons. Spin is an intrinsic quantum mechanical property of an unpaired electron that is quantized (adopts discrete values of spin states). For an unpaired electron, these states are in one of two orientations:

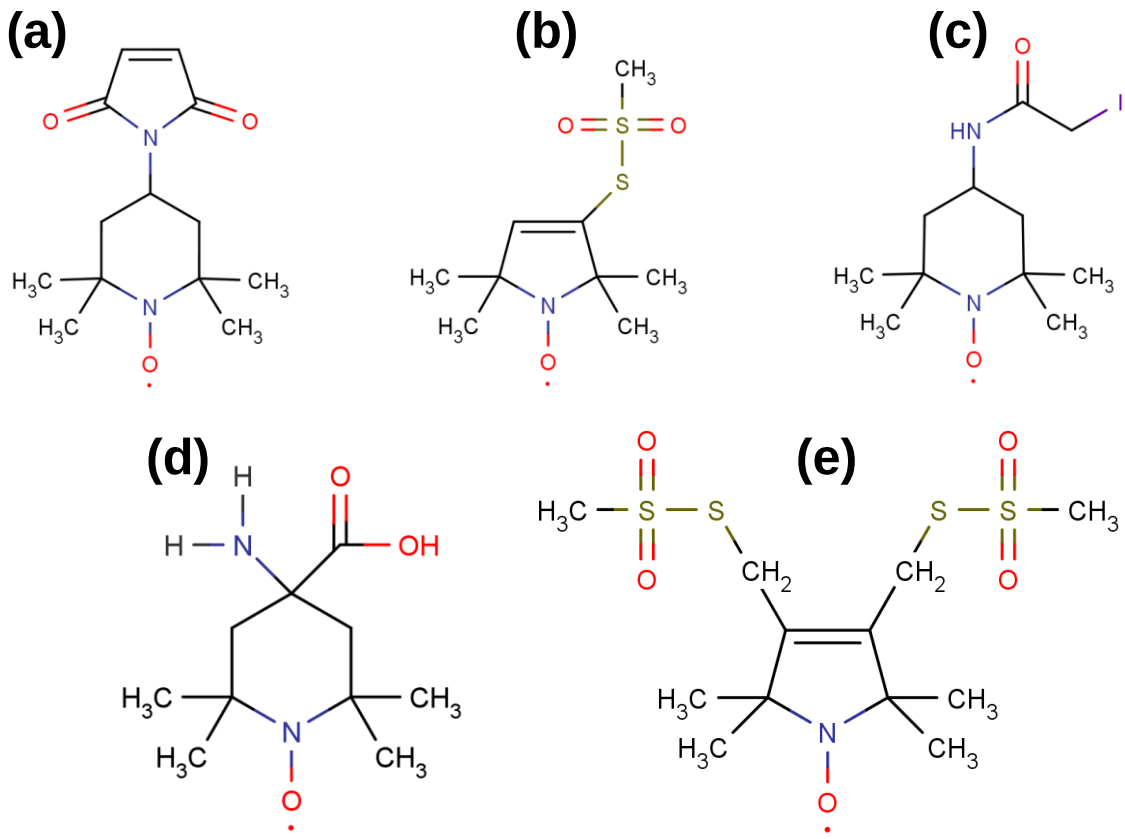

Fig. 7. Chemical structures of commonly used nitroxide spin labels**.** Maleimide spin label (MSL, a), methanethiosulfante spin label (MTSL, b), and iodoacetamide spin label (IASL, c). These labels are attached monofunctionally to proteins via a disulfide linkage with a single cysteine side chain. The other two labels which are less commonly used, 2,2,6,6,-tetramethyl-N-oxyl-4-amino-4-carboxylic acid (TOAC, d) and 3,4-bis-(methanethiosulfonyl-methyl)-2,2,5,5-tetramethyl-2,5-dihydro-1h-pyrrol-1-yloxy (BSL, e) are attached bifunctionally. TOAC is an paramagnetic unnatural amino acid that can only be incorporated through peptide synthesis, while BSL require two cysteines at i and i+4 for proper attachment.

"spin up" (m_s = +1/2) or "spin down" (m_s = -1/2). These electron spin states are degenerate in the absence of an external magnetic field (B_0 = 0), but separate into different energy states in the presence of a magnetic field in a phenomenon known as the Zeeman Effect (Fig. 8a). The extent of the splitting, which is proportional to the external magnetic field strength, allows absorption to occur when the resonance condition is satisfied. The energy of a photon is the product of its frequency (ν) and the Plank's constant (*h*), and absorption occurs when the following requirement is satisfied:

$$\Delta E = h\nu = g_e \mu_B B_0 \qquad \text{Eq. 1}$$

where *g* is the so-called g-factor (g_e = 2.0023 for free electron), μ_B is the Bohr magneton and B_0 is the external magnetic field strength. Eq. 3 specifies the resonance condition, where microwave radiation is only absorbed when their energy exactly matches the spin separation of the unpaired electron established by the external magnetic field (Fig. 8b).

Similar to electrons, nuclei also have a quantized intrinsic spin angular momentum with a magnetic moment. In the case of nitroxide spin labels, ^{14}N possesses a nuclear spin of I = 1, therefore it may adopt spin states of m_I = -1, 0, or +1. This allows the nuclei to generate an additional magnetic field that can interacts with and influences the unpaired electron. The interaction of the nitrogen magnetic field with the unpaired electron is known as the hyperfine interaction (Fig. 9), and further splits the two energy levels of the unpaired electron caused by the Zeeman Effect. The result is that there are three possible spin transition, each with its own resonance requirement, leading to the typically observed nitroxide spectrum with three peaks.

3.3 SENSITIVITY TO ROTATIONAL DYNAMICS

Of particular relevance to this thesis project, EPR is extremely sensitive to rotational dynamics. The simplest scenario to consider involves isotropic rotational tumbling, which can be related to a rotational correlation time (τ_R). When the motion is sufficiently slow in the rigid limit of CW-EPR with $\tau_R \geq 10^{-6}$ seconds, the spins are excited and relaxes before significant changes in their spatial position can occur and therefore the apparent resonances are unaffected. At the other end of the continuum, when the rate of motion becomes fast with $\tau_R \leq 10^{-12}$ seconds (fast limit), all the contributions of the anisotropies are averaged out and the EPR spectrum becomes insensitive to any motional changes. Therefore, the sensitive region of conventional EPR

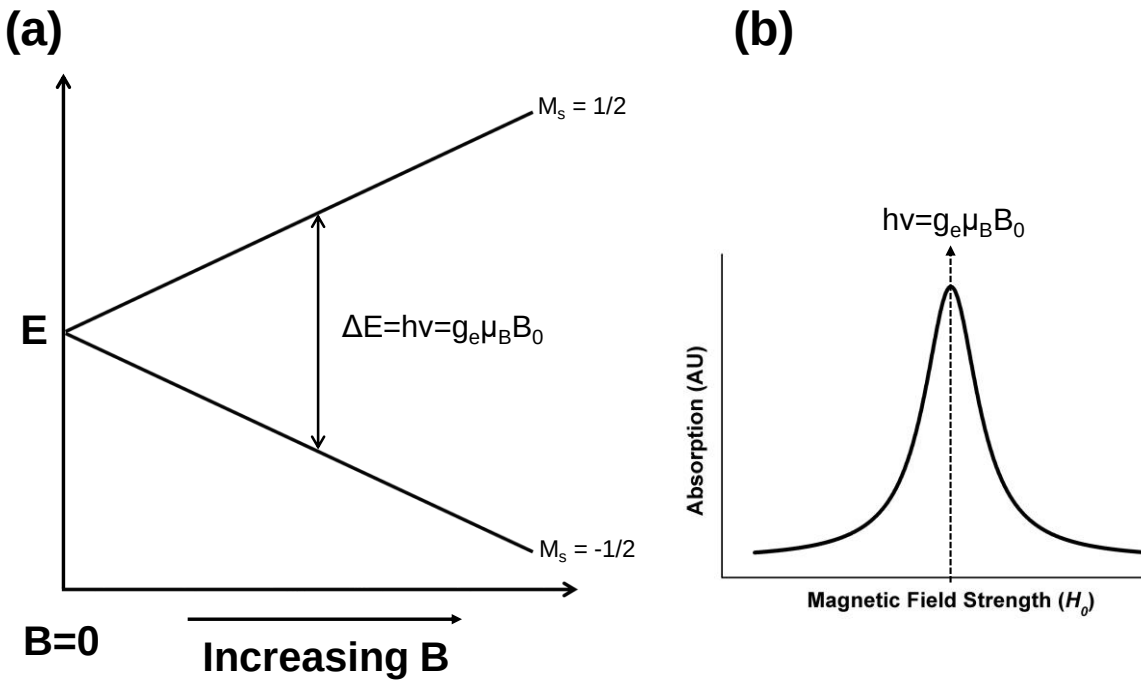

Fig. 8. The Zeeman Effect (a). An unpaired electron possesses two spin states ($m_s = \pm 1/2$). In the absence of an external magnetic field there is no separation in energy of the two spin states. In the presence of an external magnetic field, the Zeeman Effect occurs and separates the two spin states into discrete energy levels proportional to the magnetic field strength. In order for absorption of microwave photon to occur, the resonance condition must be satisfied (b).

to rotational dynamics lies with $10^{-12} \leq \tau_R \leq 10^{-6}$ seconds.

As mentioned earlier, for rotational motion slower than microseconds, conventional EPR spectrum is at the rigid limit ("powder spectrum") and loses sensitivity to changes in rotational motion. This is often the case when trying to study very large proteins, or membrane-embedded proteins. These slower motions can be detected using a technique called saturation transfer EPR (ST-EPR). In contrast to conventional EPR, ST-

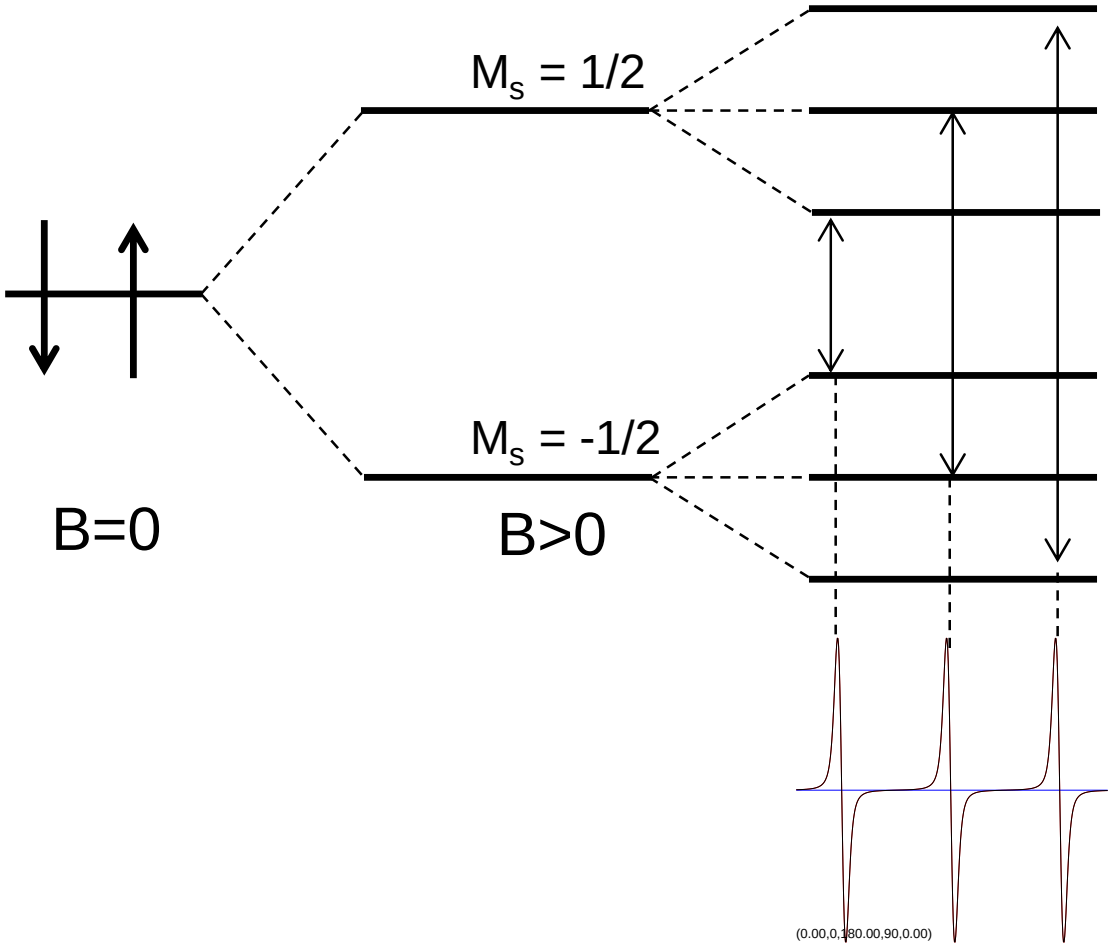

Fig. 9. The hyperfine interaction. The Zeeman Effect splits up the spin states into two energy levels. Because of interaction between the electron spin and nitrogen nuclear spin, the energy levels are further split such that there are three possible spin transitions. Each spin transition has its own resonance condition, resulting in the typical EPR nitroxide spectrum with three lines.

EPR uses a much higher microwave power to saturate the spins in the samples, disrupting the Boltzmann equilibrium. The rotational diffusion then causes saturation to diffuse to other positions in the EPR spectrum, relieving the saturation at specific spectral position in the experiment. Thus, conventional EPR is typically used for measuring motion in the range of $10^{-12} \leq \tau_R \leq 10^{-6}$ seconds, and ST-EPR for $10^{-6} \leq \tau_R \leq 10^{-3}$ seconds (Fig. 10).

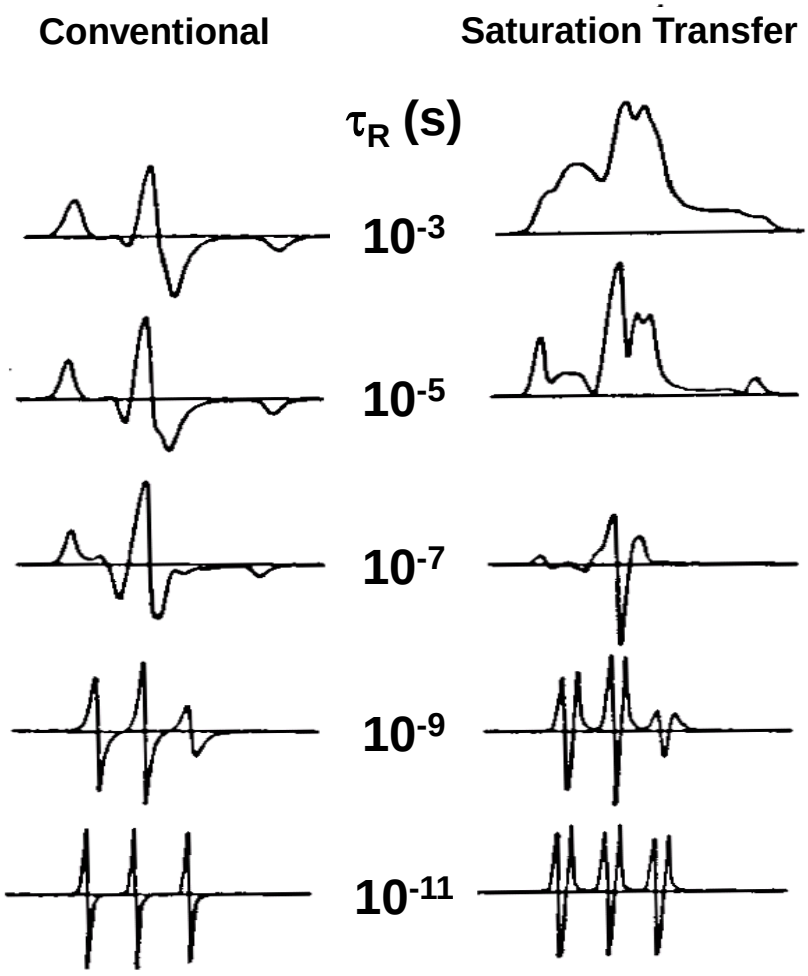

Fig. 10. EPR sensitivity to rotational dynamics. Conventional EPR has sensitivity to rotational motion in the range of $10^{-12} \leq \tau_R \leq 10^{-6}$, while saturation transfer EPR is sensitive to motion s lower than microsecond. When both techniques are used together, EPR can measure an broad range of dynamics.

3.4 DOUBLE ELECTRON-ELECTRON RESONANCE

EPR can also be used to measure more complicated protein systems to obtain more information regarding the system of interest. When two spin labels are present in a sample, the distance distribution between the labels can be measured using a pulsed EPR technique known as double electron-electron resonance (DEER, Fig. 11). Because the labels are placed at very specific sites, any changes in the observed distance distribution is directly correlated to changes in the structure of the protein. DEER is an extremely complicated process both in terms of experiment and data analysis, but can reveal highly valuable information regarding protein of interest. This technique is analogous to Forster

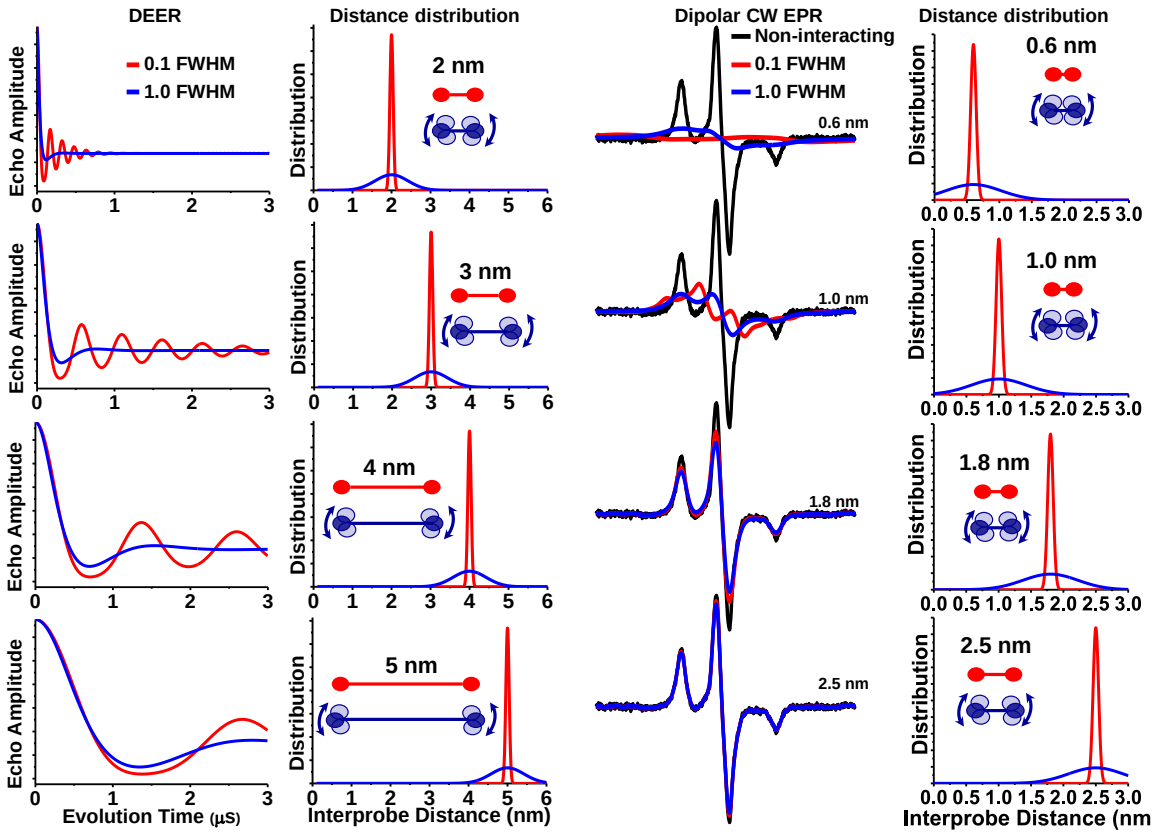

Fig. 11. Simulated data showing the sensitivity of DEER and dipolar CW-EPR to spin-spin distance and disorder. DEER is most sensitive to distances between 2.0 and 6.0 nm, while dipolar CW-EPR is sensitive to distances between 0.6 and 2.5 nm. A combined use of both techniques allow for measurement of spin-spin distances over a broad range. Low disorder systems, red. High disorder systems, blue.

resonance energy transfer (FRET) in fluorescence, but most sensitive to distances between 1.5 and 6.0 nm so it lacks the range of distance sensitivity of FRET. For shorter distances, dipolar CW-EPR that rely on detecting broadening of the CW spectrum can be used. Compared to FRET, DEER also has superior resolution due to its feature-rich waveform and advantages of smaller labels. Additionally, DEER employs the same label at both sites so the labeling experiment is much easier than FRET. Fig. 11 demonstrate the sensitivity of both DEER and dipolar CW-EPR to distance and disorder.

3.5 ADVANTAGES OF THE BIFUNCTIONAL SPIN LABEL AND TOAC

Understanding the conformational dynamics of the label is crucial to all types of site-directed spectroscopy. In the case of spin labels, the most widely used thiol-reactive nitroxide probes (Fig. 7a-c) are monofunctionally attached to protein at a single cysteine site. While these spin labels require only a single mutation, provided there are no native cysteines in the protein, and are relatively simple to use, they are not without their limitations. EPR is sensitive to motion of the spin label and not the protein. Therefore, singly flexible linkages of monofunctionally attached spin labels lead to ambiguity in the EPR spectrum such that the true dynamics of the protein is masked by the intrinsic motion and flexibility of the spin label. This problem can be eliminated with a spin label

that becomes immobilized on the protein backbone. Such is the case with two spin labels that were previously introduced: BSL and TOAC (Fig. 7d and e). Unlike the standard spin labels, BSL is bifunctionally attached at two cysteines at i and i+4 and attains rigid and stereospecific attachment to the protein (Fig. 12). TOAC also attain stereospecific and rigid attachment as it is incorporated directly into the peptide backbone. However, TOAC is a paramagnetic amino acid so it currently can only be introduced through peptide synthesis and thus limited to smaller proteins and peptides.

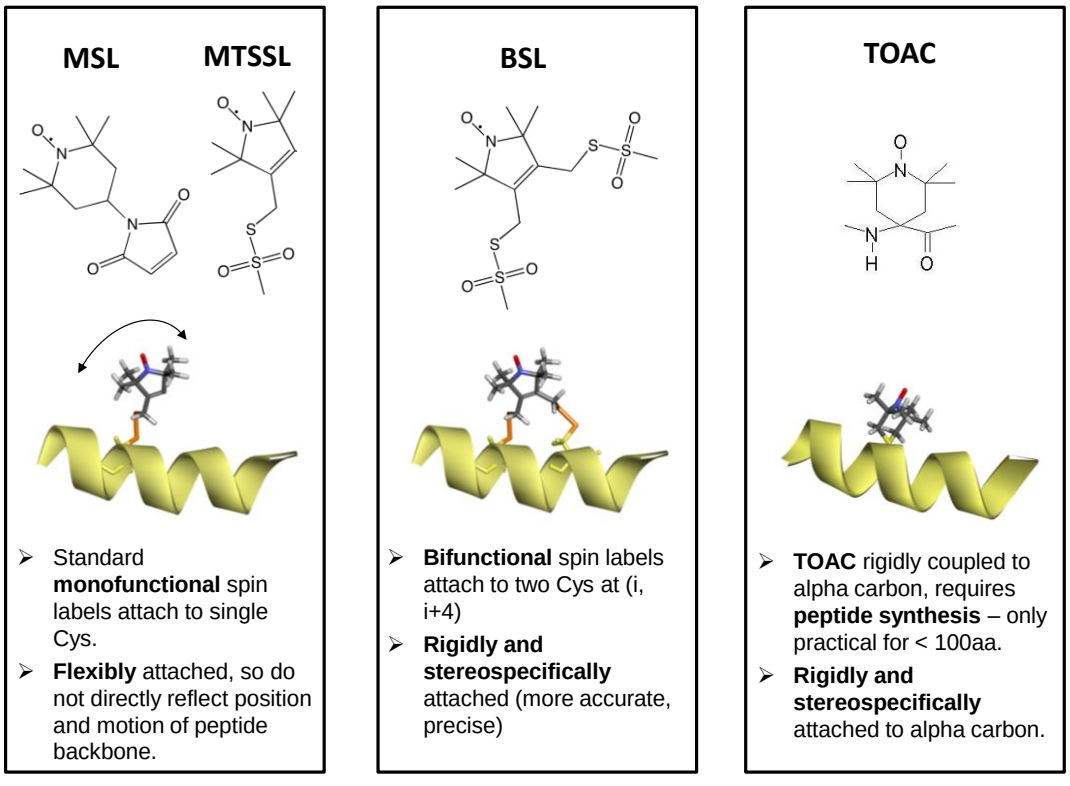

Fig. 12. Cartoon representation showing the rigid and stereospecific attachments of BSL and TOAC. This is in contrast to MSL and MTSSL which are flexibly attached and can lead to ambiguity in the EPR spectrum. BSL requires two cysteines at i and i+4, while TOAC is an unnatural amino acid so it can only be introduced through peptide synthesis.

CHAPTER 4: CALCIUM-DEPENDENT STRUCTURAL DYNAMICS OF A SPIN-LABELED RYANODINE RECEPTOR PEPTIDE BOUND TO CALMODULIN

Cheng Her, Jesse E. McCaffrey, David D. Thomas, and Christine B. Karim

Department of Biochemistry, Molecular Biology and Biophysics, University of Minnesota, Minneapolis, MN 55455

Published in *Biophysical Journal*, 2016, Vol. 111, pp. 2387-2394

4.1 CHAPTER SUMMARY

We have used chemical synthesis, electron paramagnetic resonance (EPR), and circular dichroism (CD) to detect and analyze the structural dynamics of a ryanodine receptor (RyR) peptide bound to calmodulin (CaM). The skeletal muscle calcium release channel RyR1 is activated by Ca-free CaM and inhibited by Ca-bound CaM. To probe the structural mechanism for this regulation, wild-type RyRp and four spin-labeled derivatives were synthesized, each containing the nitroxide probe TOAC (2,2,6,6-tetramethyl-piperidine-1-oxyl-4-amino-4-carboxylic acid) substituted for a single amino acid. In TOAC, the probe is rigidly and stereospecifically coupled to the α-carbon, enabling direct detection by EPR of peptide backbone structural dynamics. In the absence of CaM, CD indicates a complete lack of secondary structure, while 40% trifluoroethanol (TFE) induces > 90% helicity and is unperturbed by the spin label. The EPR spectrum of each spin-labeled peptide indicates nanosecond dynamic disorder that is substantially reduced by TFE, but a significant gradient in dynamics is observed, decreasing from N to C terminus, both in the presence and absence of TFE. When bound to CaM, the probe nearest RyRp's N terminus shows rapid rotational motion consistent with peptide

backbone dynamics of a locally unfolded peptide, while the other three sites show substantial restriction of dynamics, consistent with helical folding. The two N-terminal sites, which bind to the C-lobe of CaM, do not show a significant Ca-dependence in mobility, while both C-terminal sites, which bind to the N-lobe of CaM, are significantly less mobile in the presence of bound Ca. These results support a model in which the interaction of RyR with CaM is non-uniform along the peptide, and the primary effect of Ca is to increase the interaction of the C-terminal portion of the peptide with the N-terminal lobe of CaM. These results provide new insight into the Ca-dependent regulation of RyR by CaM.

4.2 INTRODUCTION

The Ca-binding protein calmodulin (CaM) functions as a regulator of many crucial Ca-dependent cellular and molecular processes, including the release of Ca from sarcoplasmic and endoplasmic reticulum (SR/ER) to initiate muscle contraction [13, 34]. CaM achieves this regulation by binding to the tetrameric SR Ca-release channel, the ryanodine receptor (RyR). The function of CaM on RyR is isoform-specific. In skeletal muscle, RyR1 is activated by Ca-free CaM (apoCaM) and inhibited by Ca-bound CaM (CaCaM) [35], while in cardiac muscle, RyR2 is inhibited by CaM independently of Ca binding [36, 37]. Mutagenesis studies identified Met residues of CaM that are critical for the functional interaction of CaM with RyR1 [38].

It has been proposed that modification of CaM by oxidation or mutation alters CaM's functional interaction with RyR and contributes to RyR dysfunction during oxidative stress [38, 39], and electron paramagnetic resonance (EPR) has revealed that Met oxidation induces structural perturbation of CaM [39]. Several studies have shown that a disturbed CaM/RyR2 interaction plays a key role in arrhythmia and heart failure [32, 40, 41]. CaM binding properties of the RyR's have focused on RyR1. It has been reported that apoCaM and CaCaM bind with nanomolar affinity (similar to that of the full-length channel) to a synthetic peptide matching amino acids 3614-3643 of RyR1 (RyRp) [22, 29], while other studies suggest that the affinity is much lower (micromolar) in the apo-state [42, 43]. In the present paper, the position number in the 31-residue RyRp starts from 1 at the N-terminus (3614 in full-length receptor) to 31 at the C-terminus (RyRp sequence in *Materials and Methods*). In the crystal structure of RyRp bound to CaCaM (Fig. 13), RyRp adopts an α-helical conformation in which Trp7 and Phe23 serve as

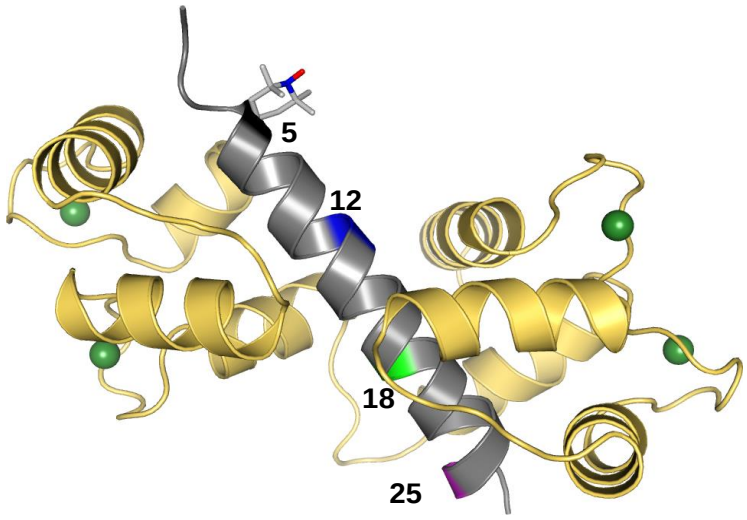

Fig. 13. Ribbon diagram showing CaCaM/TOAC-RyRp complex [30] (2bcx) (CaM yellow, RyRp grey, Ca dark green). The TOAC spin labeling position is shown as stick model at position 5, and highlights show positions 12 (blue), 18 (green), 25 (magenta). The unpaired electron is located between the nitrogen (blue) and oxygen (red).

hydrophobic anchors [30]. The crystal structure revealed antiparallel binding of the two proteins in which RyRp N-terminal residues 2-15 bind to CaM C-lobe, while the RyRp C-terminal residues 16-24 contact the CaM N-lobe [30]. Trypsin cleavage, alkylation [22], and site-directed mutagenesis [31] suggested that apoCaM and CaCaM bind to the same RyR1 region that includes Cys22 [44] and Leu11 in RyRp [31]. A recent fluorescence anisotropy study proposed a model in which the C-domain of CaM is bound to the RyRp site in the presence and absence of Ca, but the N-domain of CaM is bound only in the presence of Ca [42]. There is currently limited information on the structure and dynamics of the isolated RyRp, the apoCaM/RyRp complex, and the CaCaM/RyRp complex in solution. Boschek et al. [45] detected frequency-domain fluorescence of the native Trp residue in RyRp, so the data only report side-chain dynamics at a single site. In the present study, we used TOAC to probe directly the backbone dynamics at four different positions. Consistent with our results, Boschek et al. [45] found that RyRp is intrinsically unstructured in solution, and there is some indication of structural disorder even when bound to Ca-bound CaM.

In the present study, we have used solid-phase peptide synthesis (SPPS), circular dichroism (CD), and electron paramagnetic resonance (EPR) to detect the structural dynamics of RyRp, bound to apoCaM and bound to CaCaM in solution. EPR is a powerful technique for investigating structural changes in proteins and protein/enzyme complexes in response to regulatory modifications [46-48]. In these studies, peptides are typically prepared by Fmoc solid-phase peptide synthesis (SPPS) [49], which permits the incorporation of non-natural amino acids into the peptide sequence, including the spin-labeled amino acid TOAC (2,2,6,6-tetramethylpiperidine-1-oxyl-4-amino-4-carboxylic

acid). TOAC contains a compact probe that rigidly couples to the α-carbon and reports the accurate position, orientation, and dynamics of the peptide backbone by EPR spectroscopy [50, 51, 46, 52].

In the present paper, we present structural dynamics information for the isolated RyRp and the CaM/RyRp complex. We synthesized *wt*-RyRp and four TOAC-spin-labeled RyRp derivatives. EPR was performed to determine the nanosecond rotational dynamics of TOAC-RyRp, focusing on the effects of CaM binding in the presence and absence of Ca. CD spectroscopy was used to detect changes in the secondary structure of isolated RyRp, assisting in the interpretation of EPR data and serving as a control for the effects of spin labeling. The results provide new insight into the Ca-dependent regulation of RyR by CaM.

4.3 METHODS

Peptide synthesis

The 31-residue *wt* RyRp sequence KSKKAVWHKLLSKQRRRAVVACFRMTPLYNL [30] and four TOAC-RyRp derivatives (with TOAC substituted for Ala5, Ser12, Ala18, and Met25, respectively) were synthesized by SPPS using 9-fluorenylmethoxycarbonyl (Fmoc) protected amino acids [53]. The TOAC positions on RyRp were chosen in locations where little or no contact with CaM is made, based on the Ca-bound crystal structure of the complex [30]. For the TOAC-RyRp derivatives, Cys22 was replaced with α-amino-n-butyric acid (Abu), which is isosteric with Cys [54, 55], in order to prevent chemical artifacts during synthesis or disulfide-induced dimerization after synthesis [56, 52]. Mutation of Cys3635

(Cys22 in RyRp) to Ala in the intact receptor showed no effect on CaM binding [57]. It is sometimes stated that TOAC and Abu tend to affect the α-helical content of peptides [58, 59], but it has been shown that single-TOAC or Abu substitutions do not cause CD-detectable changes in secondary structure [60], and this is verified below in Fig. 14. All five peptides were synthesized using a Symphony automated peptide synthesizer (Protein Technologies, Inc.) at a 50 μmol scale, using a six-fold excess of Fmoc-amino acids (200 mM) relative to the Fmoc-Rink amide MBHA resin (0.32 meq/g). Coupling was performed using 1:1:2 amino acid/ HCTU/ NMM in DMF. The final cleavage of *wt*-RyRp from the resin and side-chain protecting groups was automatically performed on the instrument with 82.5% TFA, 5% phenol, 5% H_2O, 5% thioanisole, and 2.5% EDT (Reagent K) [61, 56]. Cleavage of TOAC-RyRp was performed with 95% TFA, 2.5% TIS, 2.5% H_2O. After cleavage, peptides were precipitated with cold ether and collected by centrifugation. The crude peptides were purified by HPLC on a semi-preparative C_8 column (Vydac 208TP, 300 Å, 250 x 10 mm, 10 μm particles) using a gradient from solvent A (0.1 % TFA in H_2O) to solvent B (0.1 % TFA in acetonitrile) at 3 mL/min flow rate. Fractions containing peptides were lyophilized and stored at -20 ˚C.

Peptide Analysis by Mass Spectrometry

A Waters Acquity UPLC/Synapt G2 QTOF mass spectrometer (Waters Corporation, Milford, MA) was used. A Waters Acquity BEH C_4 column (300 Å, 100 x 2.1 mm; 1.7 μm particles) at 20 ˚C was used during the 15 min gradient from solvent A (0.1 % formic acid in H_2O) to B (0.1 % formic acid in acetonitrile). The mass spectrometer was operated in the ESI positive mode, recording from *m/z* 100 to *m/z* 1500, with a scan time of 0.2 seconds. The data was processed using MassLynx V4.1 software

from Waters Laboratory Informatics. The deconvoluted mass spectra of all five RyRp showed one major peak at the predicted molecular mass for *wt*-RyRp at 3729.3 Da (calculated 3729.5 Da), 5-TOAC-RyRp at 3838.43 Da (calculated 3837.8 Da), 12-TOAC-RyRp at 3820.7 Da (calculated 3821.8 Da), 18-TOAC-RyRp 3838.1 Da (calculated 3837.8 Da), 25-TOAC-RyRp 3778.5 Da (calculated 3777.8 Da). The observed values are fully consistent with the calculated masses. The deconvoluted mass spectrum of 12-TOAC-RyRp is shown as an example in the supporting material (Fig. S1 in the Supporting Material).

Preparation of CaM and CaM/RyRp complexes

Wt-CaM was expressed and purified as previously described [62]. All samples contained 0.40 mM TOAC-RyRp in 20 mM MOPS, pH 7.4. For experiments involving CaM, TOAC-RyRp samples were first exchanged into 20 mM MOPS, 5 mM $CaCl_2$ or 5 mM EGTA, pH 7.4 using a 3K MWCO Amicon Ultra-0.5 Centrifugal Filter (EMD Millipore). 2.7 μM of RyRp was then slowly added to 5.4 μM or 10.8 μM of CaM at 4˚C. A 10K MWCO Amicon Ultra-4 Centrifugal Filter was used to concentrate the samples to a final concentration of 0.40 mM TOAC-RyRp and 0.8 mM or 1.6 mM CaM for EPR experiments. The low micromolar concentrations used, and the substantial excess of CaM over RyRp, were essential to avoid aggregation, which was not observed upon concentration after mixing. Since all K_d values for Ca binding to CaM are in the micromolar range and K_d values for Ca binding to EGTA are in the nanomolar range [63], 5 mM EGTA is sufficient to produce apoCaM in our conditions.

EPR spectroscopy and data analysis

EPR spectra were acquired with a Bruker EleXsys E500 (9.5 GHz) spectrometer equipped with the ER 4122 SHQ cavity, using field modulation at 100-kHz with 1 G amplitude. The time constant and conversion time were 20.48 ms. The microwave power was 1.26 mW, which is low enough to avoid saturation. 20 μL of TOAC-RyRp or CaM/TOAC-RyRp sample were loaded into a 25 μL Wiretrol glass capillary with 0.855 mm inner diameter and 1.372 mm outer diameter (Drummond Scientific). EPR spectra were background-corrected and normalized to the spin concentration by dividing by the double integral. Spectra of the isolated TOAC-RyRp were analyzed to determine the rotational correlation time,

$$\tau_R = z\Delta H_0([h_0/h_{-1}]^{1/2}-1), \qquad \text{Eq. 2}$$

where z = 6.5x10^{-10}s/G, ΔH_0 = width of the center-field peak in G, h_0 = height of the center-field peak, and h_{-1} = height of the high-field peak [64]. The EPR spectrum of TOAC-RyRp bound to CaM was analyzed to determine the rotational correlation time using Equation 2,

$$\tau_R = a[1-(T_{//}'/T_{//})]^b, \qquad \text{Eq. 3}$$

where a = 0.54 ns, b = -1.36, $T_{||}'$ = splitting between the outer extrema, and $T_{||}$ = the rigid-limit value of $T_{||}'$ [65]. All EPR spectra were also analyzed using the LabView program MultiComponent [66] to determine rotational correlation times of each spectral component and their mole fractions. In the fitting of CaM-bound data, the rotational correlation times of the fast components were held fixed to values determined from spectra of isolated RyRp.

Circular Dichroism

CD spectra were acquired at 22 °C with a JASCO J-815 spectrophotometer, scanning from 190 nm to 260 nm with a scan rate of 50 nm/min, 0.1 nm bandwidth. Spectra were signal-averaged five times and baseline subtracted. Reported spectra are expressed as mean residue ellipticity, [θ]. Linear combinations of α-helix, β-sheet and random coil bases spectra were used to determine secondary contributions from fits to acquired CD spectra [67, 68]. Samples for CD consisted of 25 μM RyRp in 10 mM Na_2HPO_4 pH 7.4 loaded into quartz cuvettes with a path length of 0.1 cm.

4.4 RESULTS

Random coil to α-helix transition of RyRp as shown by CD

The CD spectra of *wt*-RyRp and TOAC-RyRp at positions 5, 12, 18 and 25 in Na_2HPO_4 buffer are shown (Fig. 14). The spectra of all five samples indicate a random coil conformation in buffer (black symbols), characterized by a strong negative CD band

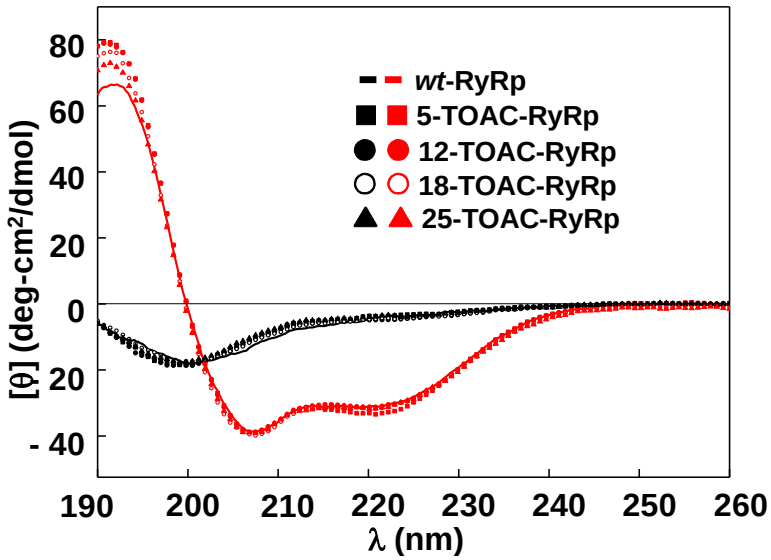

Fig. 14. CD spectra of RyRp (wt) and its spin-labeled derivatives. Peptide in buffer alone shown in black and in 40 % TFE v/v in red.

near 200 nm. Analysis indicates 0% helical content. Next, we wanted to investigate whether RyRp could adopt an α-helix conformation. TFE favors conversion of unstructured regions of peptides to α-helical structures [69]. CD was used to detect the secondary structural change of *wt*-RyRp and TOAC-RyRp derivatives in buffer/TFE mixtures. Stepwise addition of TFE from 0% to 60% v/v induced a shift from random coil to α-helical conformation. No changes in CD were observed beyond 40% TFE. All five RyRp displayed CD spectra at 40% TFE characteristic of α-helical structure with an upward band at 190 nm and two negative bands near 208 and 222 nm (red symbols). Analysis of these CD spectra at 40% TFE indicates greater than 90% α-helical content (Table 1). We conclude that the isolated RyRp is unstructured in buffer and primarily helical in 40% TFE, with no effect of TOAC spin-labeling.

EPR spectra of isolated TOAC-spin-labeled RyRp

The EPR spectra of RyRp with TOAC attached at positions 5, 12, 18 and 25 (Fig. 15, black; Table 1) show narrow peaks, indicative of large-amplitude nanosecond rotational dynamics, consistent with the unfolded structures indicated by CD in Fig. 14. However, EPR reveals additional information – there is a gradient of nanosecond

Table 1. Parameters from CD and EPR analysis of wt-RyRp and TOAC-RyRp in 0% and 40% TFE as indicated. Reported τ_R are means and standard error from three independent experiments.

TOAC position.	% α-helix (0% TFE)	% α-helix (40% TFE)	τ_R(ns)[a] (0% TFE)	τ_R(ns)[a] (40% TFE)	τ_R(ns)[b] (0% TFE)	τ_R(ns)[b] (40% TFE)
none	0	94.1 ± 0.4	-	-		
5	0	97.2 ± 0.5	0.35 ± 0.02	1.62 ± 0.05	0.22 ± 0.08	1.29 ± 0.11
12	0	97.3 ± 0.6	0.65 ± 0.01	1.68 ± 0.04	0.66 ± 0.33	1.66 ± 0.05
18	0	92.8 ± 1.2	0.92 ± 0.03	2.70 ± 0.02	1.09 ± 0.31	2.23 ± 0.07
25	0	90.6 ± 1.5	1.22 ± 0.01	3.81 ± 0.05	1.08 ± 0.15	3.39 ± 0.04

[a]Determined as from Eq. 2. [b]Determined using MultiComponent.
Each value is given as mean and standard error (n = 3). These values are plotted in Fig. S19.

rotational dynamics across the backbone of the peptide with shortest rotational correlation time at position 5 and longest at 25 (Table 1). RyRp is completely unfolded (disordered) and highly mobile at its N terminus, while this disorder and mobility decreases steadily toward the C terminus.

The addition of 40% TFE caused an increase in the correlation time in all four TOAC-RyRp (Fig. 15 red), consistent with the α-helix formation indicated by CD in Fig. 14, and again EPR detects an additional gradient of decreasing mobility (increasing

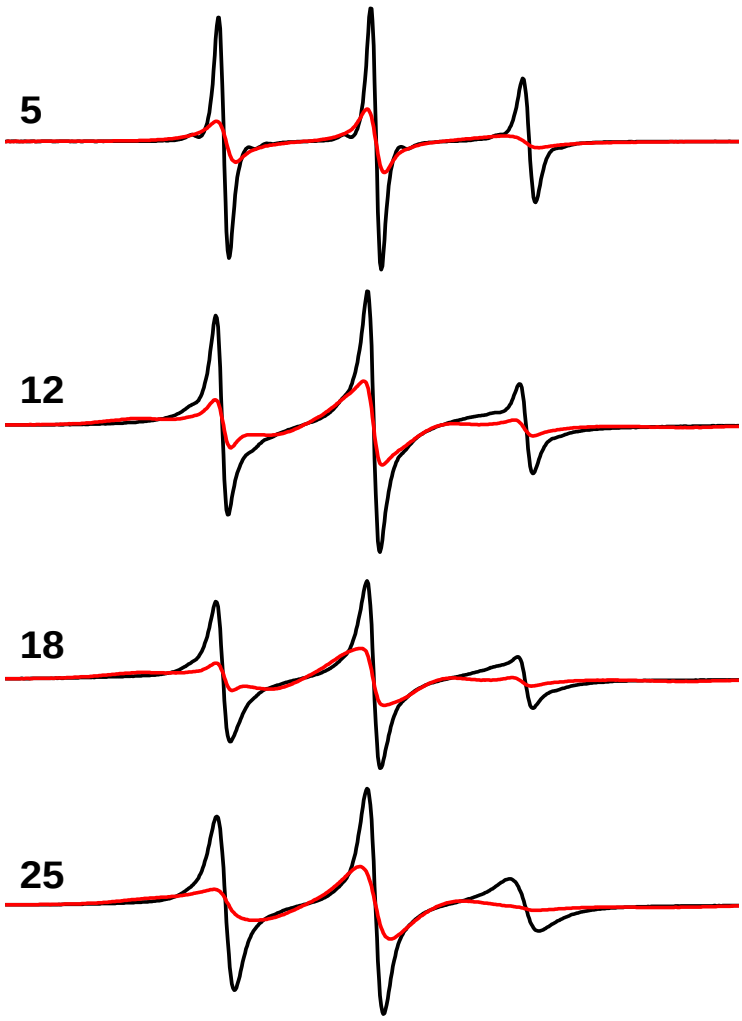

Fig. 15. EPR spectra of TOAC-RyRp in 20 mM MOPS, pH 7.4 are shown in black and in 40 % TFE v/v in red. The position of the TOAC label in the RyRp sequence is indicated at left. Spectra were obtained with a 80-G scan at 22 ˚C and normalized to the spin concentration by dividing by the double integral.

structural order) toward the C terminus (Table 1). The increase in the rotational correlation time in the 40% TFE samples is not due entirely to an increase in viscosity, as demonstrated in Table S3. Viscosity increases by less than 2-fold when going from 0% to 40% [70], but the increase in correlation time due to 0% TFE was greater than 2-fold in all cases, strongly suggesting that TFE increases RyRp folding.

EPR spectra of TOAC-spin labeled RyRp bound to CaM

In order to gain structural insight into the binding of RyRp by CaM, we used EPR to measure the rotational dynamics of each of the four TOAC-RyRp derivatives bound to CaM in the absence (Fig. 16, black) and presence (Fig. 16, red) of saturating Ca. The spectra reveal dramatic differences in nanosecond rotational dynamics, with narrow spectra indicating dynamic disorder, and broad spectra indicating slower and more restricted motion. TOAC at the N-terminal position 5 shows a single component with narrow peaks indicating that TOAC remains remarkably mobile even after CaM binding. Ca only slightly decreases the mobility as shown by slight broadening of the EPR line-shape. TOAC at position 12 shows two spectral components, ordered and disordered, demonstrating two conformations at this local region of RyRp bound to apoCaM and CaCaM. The spectrum of TOAC at the C-terminal positions 18 and at 25 bound to apoCaM is similar to that at the 12 position, indicating two resolved spectral components. In contrast, when bound to Ca- CaM TOAC at 18 and 25 shows a nearly complete shift to the broad component, corresponding to highly restricted motion, implying both helical order and strong binding to CaM

Quantitative analysis of rotational dynamics of TOAC-RyRp/CaM

We analyzed the EPR spectra of TOAC-RyRp bound to CaM (Fig. 16) in more quantitative detail using the program MultiComponent [66] (results summarized in Table 2). We assumed the presence of several (one to three) structural states in each sample, each characterized by a rotational correlation time τ_{Ri} and a mole fraction X_i. We varied the number of components needed to obtain the best fit. The fast component (τ_{R1}) was fixed in both apoCaM and CaCaM spectra because varying it did not improve the fit.

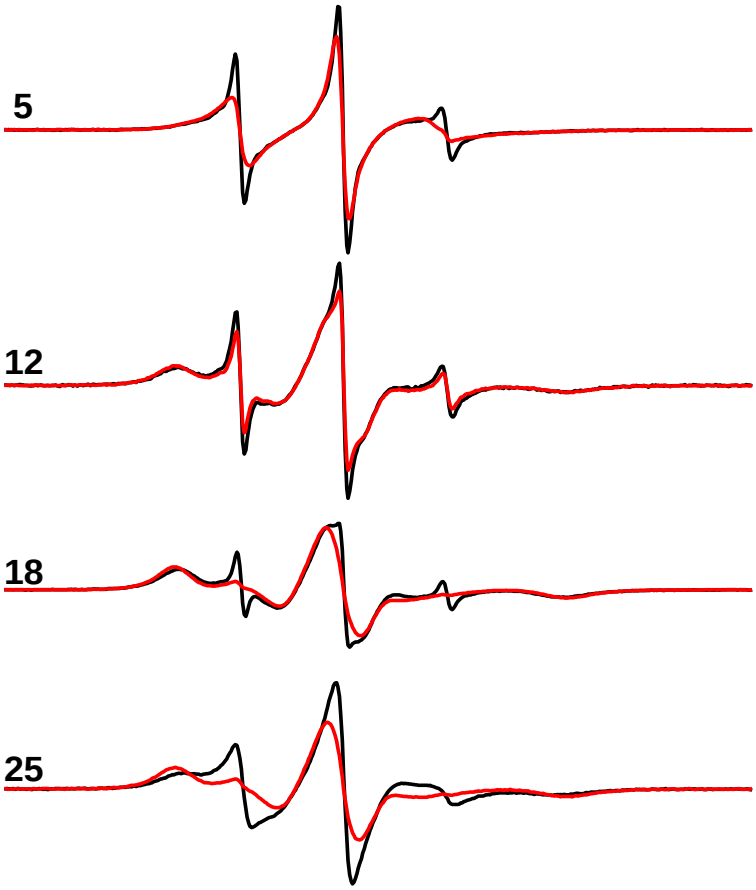

Fig. 16. EPR spectra of TOAC-RyRp bound to CaM in the absence (black) and presence (red) of saturating Ca. The concentrations of TOAC-RyRp and CaM were 0.4 mM and 1.6 mM, respectively. Spectra corresponding to 0.4 mM TOAC-RyRp and 0.8 mM CaM were identical to the spectra shown in this figure, indicating that all RyRp was bound to CaM. The position of the TOAC label in the RyRp sequence is indicated at left. Spectra were obtained with a 120-G scan at 22 ˚C and normalized to the spin concentration by dividing by the double integral.

Consistent with the appearance of the EPR lineshapes, each TOAC-RyRp spectrum was best fitted with a two-component model consisting of dynamically disordered and ordered populations (Fig. S21). In each case, the slower (more ordered) component accounts for more than 80% of the population, and the correlation time of that component (τ_{R2}) is in good agreement with that determined empirically from the maximum spectral splitting (τ_{RS}). The 12-, 18-, and 25-TOAC region of the peptide bound to apoCaM exists

in equilibrium between a low-mobility (more ordered and folded) state and a locally unfolded state, as indicated by the large differences between the correlation times of each component, τ_{R1} and τ_{R2} (Table 2), while the probe at position 5 shows much more mobility (dynamic disorder). In our analysis of EPR spectra, we report results for a simple isotropic diffusion model (order parameter 0), because the fits were not improved by allowing non-zero order parameters.

Table 2. Parameters from EPR analysis of TOAC-RyRp bound to apoCaM and CaCaM.

TOAC RyRp Position	apoCaM				CaCaM			
	τ_{RS}[a] (ns)	τ_{R1}[b] (ns)	τ_{R2}[b] (ns)	X_2[b]	τ_{RS}[a] (ns)	τ_{R1}[b] (ns)	τ_{R2}[b] (ns)	X_2[b]
5	1.37 ± 0.55	0.22	1.52 ± 0.12	0.90 ± 0.03	1.40 ± 0.10	0.22	1.48 ± 0.16	0.99 ± 0.03
12	10.20 ± 0.52	0.66	9.95 ± 0.65	0.84 ± 0.05	11.47 ± 1.77	0.66	12.48 ± 0.88	0.89 ± 0.04
18	8.80 ± 0.80	1.09	10.28 ± 1.35	0.91 ± 0.04	12.12 ± 1.45	1.09	13.57 ± 2.91	0.98 ± 0.01
25	6.39 ± 0.89	1.08	4.67 ± 0.88	0.87 ± 0.02	11.71 ± 1.30	1.08	9.76 ± 1.93	0.98 ± 0.02

[a]τ_{Rs}, rotational correlation time determined empirically from splitting of the restricted/ordered component (Eq. 2). [b]The other parameters, τ_{R1} (rotational correlation time of mobile/disordered component), τ_{R2} (rotational correlation time of restricted/ordered component), and X_2 (mole fraction of the restricted/ordered component), were obtained from a two-component fit using MultiComponent. τ_{R1} values were held fixed to values determined from fits of isolated TOAC-RyRp. Each value is mean and standard error from multiple experiments (n = 3-4).

The primary effect of Ca is to shift the equilibrium toward the more mobile (less folded) component, and to uniformly immobilize the three C-terminal probes (at positions 12, 18, and 25). This effect was most pronounced at position 25 (near the C terminus of RyRp), where the mole fraction X_2 of the immobile component increased from 0.87 to 0.98, and its correlation time τ_{R2} increased from 6.4 to 9.8 ns.

4.5 DISCUSSION

The x-ray crystal structure of the CaM/RyRp complex reveals that when Ca is bound to CaM, the CaM-RyRp interaction occurs in an antiparallel fashion with the N-lobe of CaM making contact with the C-terminal half of RyRp [30]. However, before the present study, there was no structural information on this interaction in the absence of Ca, and there was no information about the structural dynamics of this system. The present study fills those gaps.

Our results indicate that the N-terminal portion of RyRp is remarkably flexible and dynamically disordered even when CaM is bound, as shown by EPR of TOAC at position 5 (Fig. 16). At the other three positions, the peptide backbone is in equilibrium between two clearly resolved structural components, dynamically disordered and ordered (Fig. 16). The narrow spectral component of 12-TOAC RyRp, which indicates nanosecond dynamic disorder, remained present even after addition of excess CaM (see legend to Fig. 16). This observation can be explained by one of two possibilities: 1) there is a small fraction of 12-TOAC RyRp that is not binding to CaM, or 2) there is a small fraction of 12-TOAC RyRp that is locally unfolded at this region even when bound to CaM. The observation that the narrow spectral component did not decrease upon addition of more CaM (from 2CaM:1RyRp to 4CaM:1RyRp) indicates that there is no unbound 12-TOAC RyRp. This conclusion is also supported by the lack of unbound TOAC-labeled peptide in the filtrate after ultrafiltration of the CaM/RyRp sample. Thus we conclude that the narrow spectral component at position 12 in (Fig. 16) corresponds to a dynamically disordered population that represents bound but locally unfolded peptide. The results of CaM-bound 5- and 12-TOAC RyRp (N-terminal half of RyRp) are largely

unaffected by the addition of Ca, suggesting that Ca has a minimal effect on the interaction of this region with the C-lobe of CaM.

The largest effect of Ca on CaM bound RyRp occurs at the two C-terminal positions, 18 and 25, which bind to the N-lobe of CaM. In these cases, in the absence of Ca the EPR spectra show both mobile and immobile components, corresponding to dynamically disordered and ordered states at these local regions on RyRp (Fig. 16), but in the presence of Ca there is an almost complete shift to the ordered state, indicating complete immobilization and ordering of the TOAC spin label by CaM N-lobe binding (Fig. 16). This disorder-to-order transition was reversed by removing Ca. Thus, the results from Fig. 16 indicate that in the absence of Ca, CaM binding to RyRp exists in a structural equilibrium between a state where only the C-lobe of CaM is bound and one where both lobes are bound. The N-lobe of CaM is more loosely bound to RyRp C-terminal region in the absence of Ca, while the C-lobe binding to RyRp N-terminal is unaffected by Ca. Consistent with our results, Xiong et al. showed that a truncated CaM representing the N-lobe (amino acids 1-79) had very low affinity for RyRp at low Ca conditions and that binding was detected under high Ca, whereas the C-lobe of CaM (amino acids 78-149) bound well to RyRp under both Ca conditions [71].

Our results support the model proposed by Newman et al., in which the C-lobe of CaM is bound to RyRp in the apo and Ca-bound state and the N-lobe required Ca for binding to the same site on RyR [72]. Newman et al. and others [73, 74, 72, 75] further proposed that CaM N-lobe may be bound to an alternative non-contiguous site on RyR in the absence of Ca and that Ca binding transitions the N-lobe to bind to the 3614-3643 site. Although we did not study any other CaM-binding RyR peptides, our results do not

entirely dismiss this idea. By directly detecting the dynamics of RyRp, we have refined this model and further proposed a structural basis for the binding of CaM to RyRp. In the presence of CaM but absence of Ca, the complex exists in structural equilibrium between a major structural state where both lobes are bound and RyRp is mostly structured, and a minor one where only the C-lobe is bound and RyRp is mostly unstructured. Addition of Ca shifts the equilibrium to the state where both lobes are bound and RyRp mostly structured, but a small fraction of the complex containing unstructured RyRp at the 12-TOAC region remains. The N-terminal region detected by 5-TOAC remained flexible relative to the other regions on RyRp, indicating that it falls outside of the CaM binding site. Our results indicate that the CaM/RyRp complex is dynamic. The structural dynamics reported here support CaM C-domain association with RyR in the absence of Ca, positioning CaM to respond more quickly to the changes in cytosolic Ca levels.

The observation that the two lobes of CaM can function independently suggests that the binding is more complex. The ordered component in the apoCaM-bound data (Fig. 16, black) may reflect local order due to binding of the C-lobe to RyRp at the C-terminal region. Future studies are needed to consider an alternative model in which the C-lobe of apoCaM can bind to either the N-terminal or C-terminal regions.

4.6 CONCLUSION

We have used peptide synthesis, CD and EPR to detect the Ca-dependent structural dynamics of RyRp bound to CaM, using a spin label that reports directly the dynamics of the peptide backbone. We found that RyRp is unstructured in solution, exhibits a gradient of decreasing nanosecond dynamic disorder from the N-terminal region to the C-terminal region, and attains maximum helical content (>90%) upon

addition of 40% TFE. This random coil to α-helix transition was detected by both CD and EPR. EPR shows that the binding of RyRp to CaM causes effects that are Ca-dependent and nonuniform along the peptide. The primary effect of Ca on the bound complex was to increase the effect of the N-lobe of CaM on immobilization of the C-terminal portion of the peptide. These results are consistent with a model in which the N-lobe of CaM is the main sensor responsible for Ca-dependent interaction with the RyR.

4.7 SUPPLEMENTAL INFORMATION

Fig. S17. The 31-residue wt-RyRp sequence and four TOAC (τ) derivatives. B. Ala5TOAC C. Ser12TOAC D. Ala18TOAC, and E. Met25TOAC were synthesized. Cys22 (red) was replaced with α-amino-n-butyric acid (X), which is isosteric to Cys.

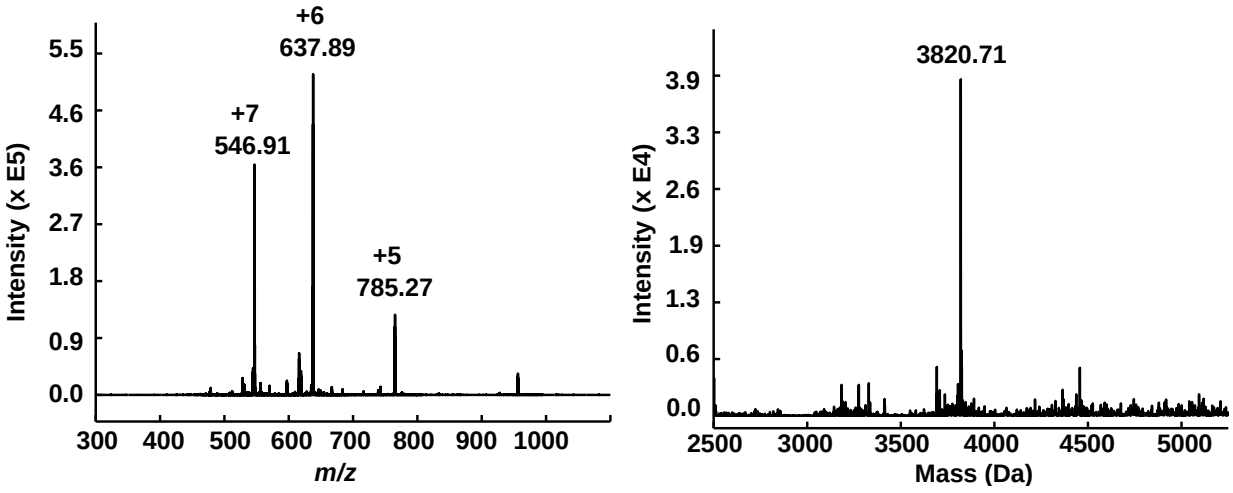

Fig. S18. Mass-to-charge (m/z) spectrum of 12-TOAC RyRp showing three different charged states (left). Deconvoluted mass spectrum showing a single high intensity peak at 3820.71, consistent with the calculated mass of 3821.8 (right).

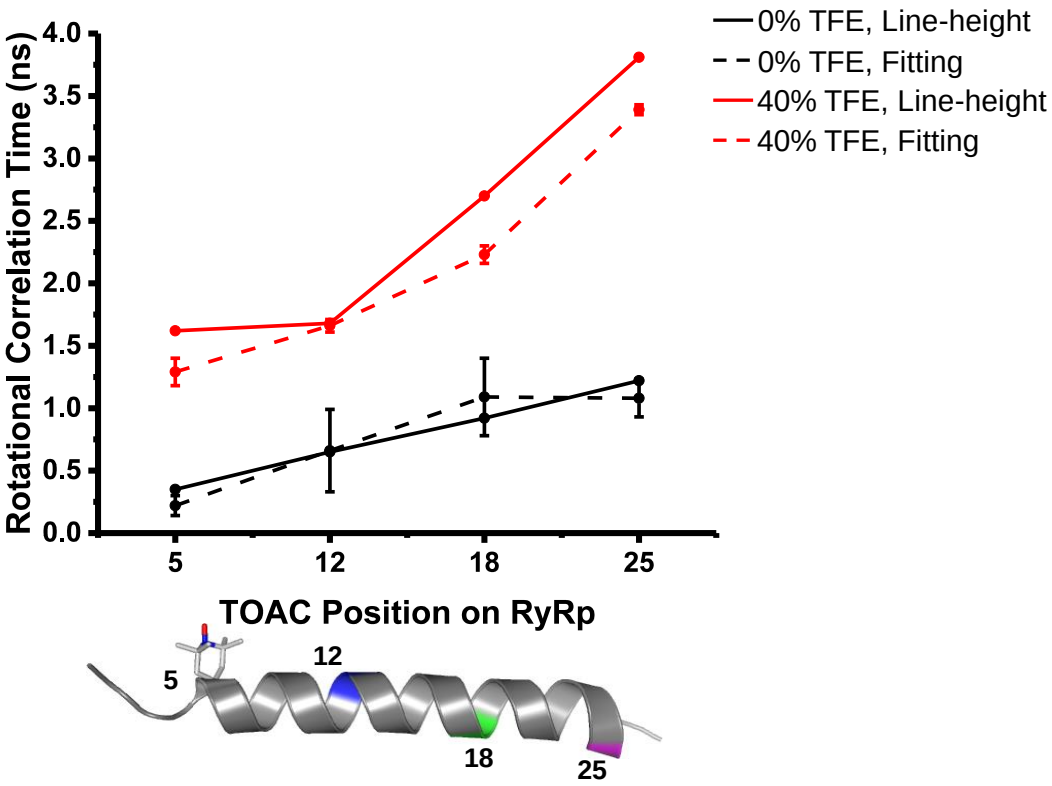

Fig. S19. Rotational correlation times of isolated TOAC-RyRp in 0% TFE (black) and 40% TFE (red) as a function of TOAC position on RyRp. Values were determined from line-height ratio method using Eq. 2 (solid) and spectral simulation and fitting using MultiComponent (dashed). Data are means and standard errors of three experiments.

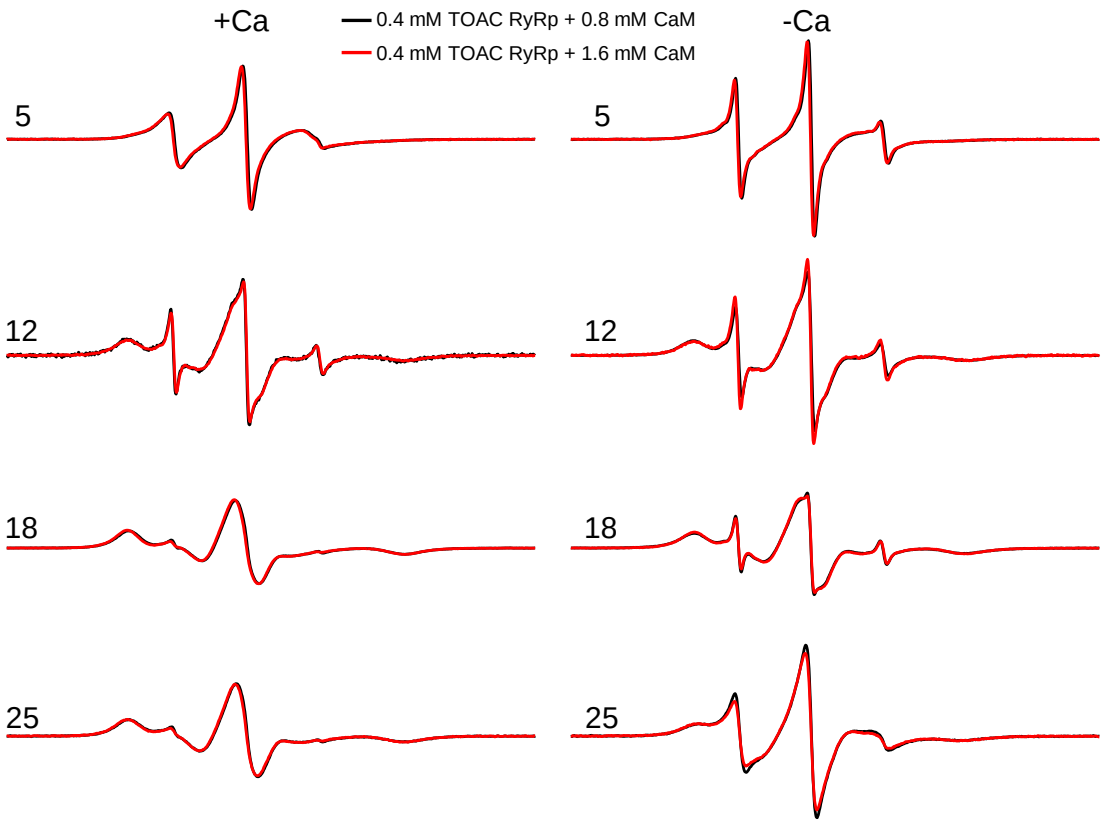

Fig. S20. Overlay of EPR spectra revealing that 2x molar excess CaM is sufficient to bind all TOAC RyRp. Data corresponding to 0.4 mM TOAC RyRp and 0.8 mM CaM (black) with 0.4 mM TOAC RyRp and 1.4 mM CaM (red) in the presence of 5 mM Ca (left) or 5 mM EGTA (right). All spectra were obtained with a 120-G scan at 22 °C and normalized to the spin concentration by dividing by the double integral.

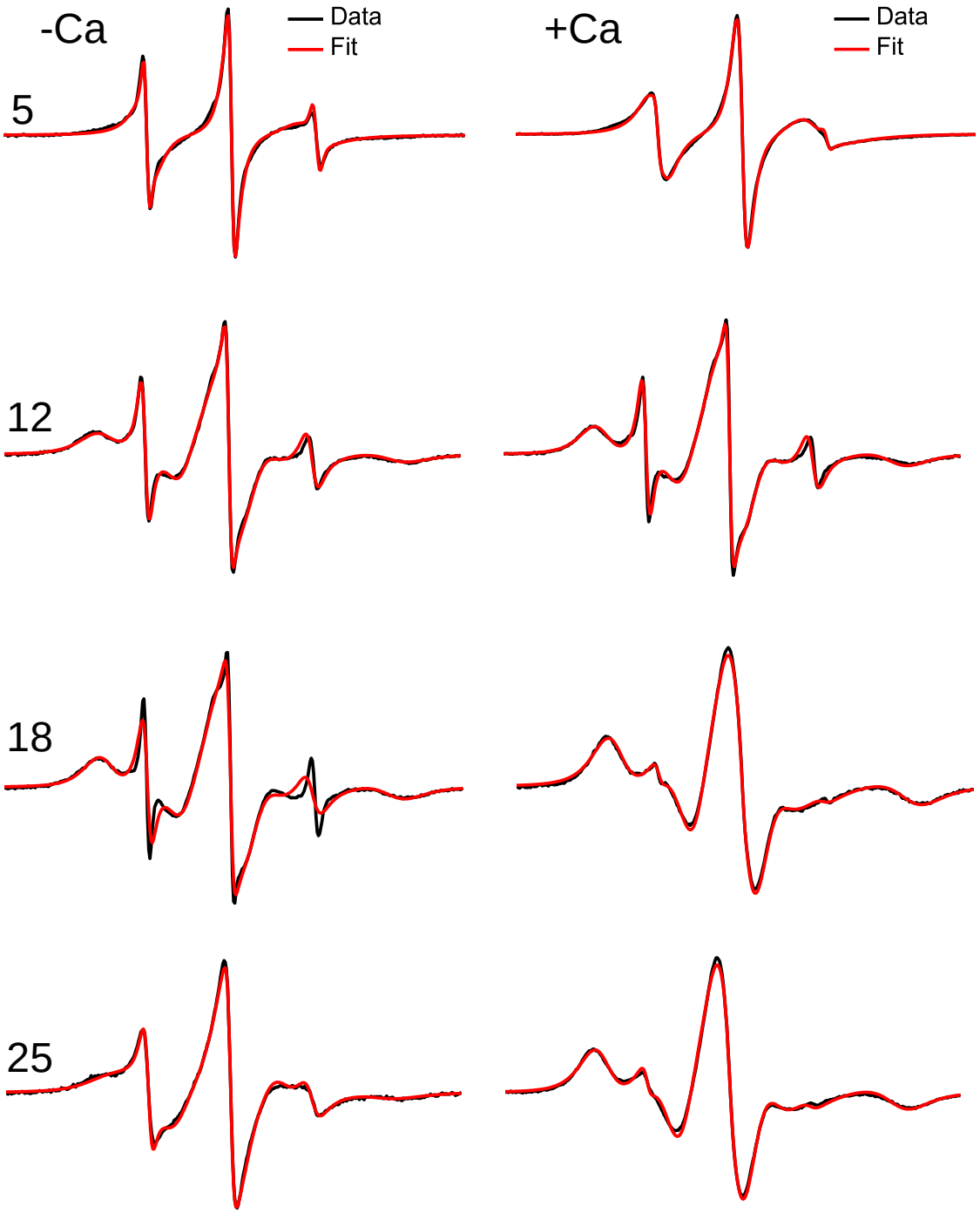

Fig. S21. Overlay of 5-, 12-, 18-, and 25-TOAC RyRp data and best fits. Data spectra (black) and best fits (red) in the presence of EGTA (left) and Ca (right). Fits were performed assuming a 2-component model as described in *Materials and Methods*. Scan width = 90 G.

Table S3. The effect of 40% TFE on viscosity (η) and rotational correlation times (τR) of TOAC RyRp derivatives calculated from line-height ratio and data fitting using MultiComponent.

	TFE	Line-Height τ_R (ns)[a]				Fitting τ_R (ns)[b]				η
	%	5-TOAC	12-TOAC	18-TOAC	25-TOAC	5-TOAC	12-TOAC	18-TOAC	25-TOAC	(cP)
	0	0.35±0.02	0.61±0.01	0.92±0.03	1.22±0.01	0.22±0.08	0.65±0.33	1.09±0.31	1.08±0.15	0.889
	40	1.62±0.05	1.68±0.04	2.70±0.02	3.81±0.05	1.29±0.11	1.66±0.05	2.23±0.07	3.39±0.04	1.64
Ratio		4.64	2.75	2.93	3.12	5.86	2.55	2.04	3.14	1.83

[a] Defined in Eq. 2. [b]Parameters were obtained from analysis of EPR spectra by MultiComponent as described in *Materials and Methods*. Reported values are means and standard errors of three experiments.

CHAPTER 5: STRUCTURAL DYNAMICS OF CALMODULIN-RYANODINE RECEPTOR INTERACTIONS: ELECTRON PARAMAGNETIC RESONANCE USING STEREOSPECIFIC SPIN LABELS

Cheng Her, Andrew R. Thompson, Christine B. Karim and David D. Thomas

Department of Biochemistry, Molecular Biology and Biophysics, University of Minnesota, Minneapolis, MN 55455

Published in *Nature Scientific Reports,* 2018, 8:10681

5.1 CHAPTER SUMMARY

We have used electron paramagnetic resonance, with rigid and stereospecific spin labels, to resolve structural states in calmodulin (CaM), as affected by binding of Ca and a CaM-binding peptide (RyRp) derived from the ryanodine receptor (RyR), the Ca channel that triggers muscle contraction. CaM mutants containing a pair of cysteines in the N-lobe and/or C-lobe were engineered and labeled with a stereospecifically bound bifunctional spin label (BSL). RyRp was synthesized with and without TOAC (a stereospecifically attached spin-labeled amino acid) substituted for a single amino acid near the N-terminus. Intramolecular DEER distance measurements of doubly-labeled BSL-CaM revealed that CaM exists in dynamic equilibrium among multiple states, consistent with open, closed, and compact structural models. Addition of RyRp shifted the equilibrium partially toward the compact state in the absence of Ca, and completely toward the compact state in the presence of Ca, supporting a conformational selection model. Inter-protein distance measurements show that Ca stabilizes the compact state primarily by inducing ordered binding of the CaM N-lobe to RyRp, while only slightly affecting the C-lobe. The results provide insight into the structural mechanism of CaM-mediated RyR regulation, while demonstrating the power of using two types of rigidly and stereospecifically bound spin labels.

5.2 INTRODUCTION

Calmodulin (CaM) is a 148-amino acid Ca-binding protein that functions as a regulator of many crucial Ca-dependent cellular and molecular processes, including the release of Ca from sarcoplasmic reticulum (SR) to initiate muscle contraction [13, 78]. CaM consists of two canonical EF-hand lobes tethered by a flexible helical linker [6]. The two lobes share high sequence homology (75%) and structural similarity in the presence [3, 8, 79] and absence of Ca [80, 77, 81]. However, the differences in the two lobes result in distinct biochemical properties. The C-lobe coordinates Ca ions with 10-fold higher intrinsic affinity[82, 83]. The flexible linker between the two lobes enables flexibility that facilitates interaction with a diverse array of targets. One CaM target of growing interest is the tetrameric sarcoplasmic reticulum Ca release channel, the ryanodine receptor (RyR). CaM directly binds to RyR and influences channel opening probability in an isoform-specific manner. In skeletal muscle (RyR1) CaM potentiates channel opening below μM Ca and inhibits above μM Ca; in the cardiac isoform (RyR2) CaM is inhibitory at all Ca levels [26, 25, 21]. The goal of the present study is to increase our understanding of the structural changes involved in the Ca-dependent regulation of RyR1. Three high-resolution structural models relating to this problem have been characterized. The X-ray crystal structure of CaCaM revealed an open extended conformation with the N- and C-lobes separated by a folded α-helix central linker region [3] (Fig. 22a). The solution NMR structure of apoCaM showed a more closed structure, with the central helix partially unfolded [77] (Fig. 22b). The X-ray crystal structure of CaCaM complexed with a peptide constituting the CaM binding site on RyR (CaCaM/RyRp), showed an even more compact structure, in an anti-parallel configuration [30] (Fig. 22c).

However, these high-resolution structures leave significant gaps in our understanding of this important system. First, there is no high-resolution structure of the apoCaM/RyRp complex (Fig. 22d and f). Second, it is likely that the structural states in solution are more complex than depicted in Fig. 22, with multiple structural states being occupied at equilibrium, as suggested by NMR data on apoCaM [77, 81, 84, 8, 85].

Structure determination by X-ray crystallography requires trapping a single

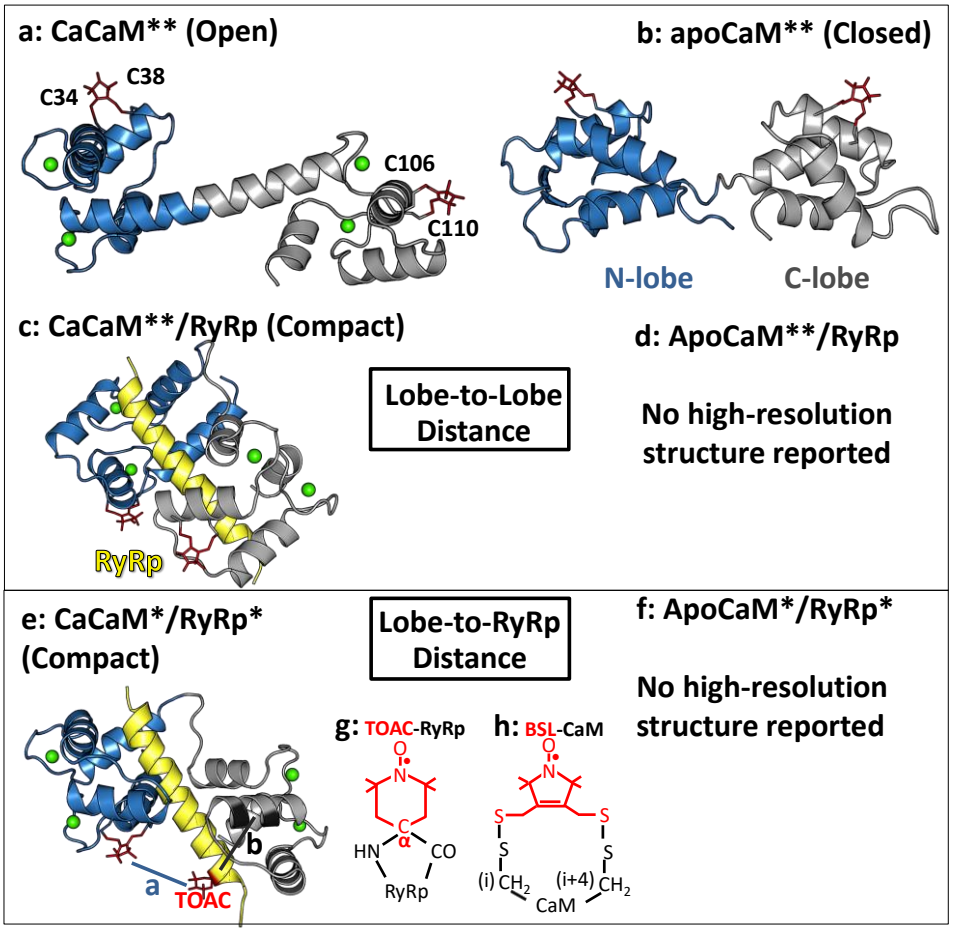

Fig. 22. Strategy for spin-spin distance measurements. (a-d) CaM lobe-to-lobe intramolecular distances. (e-f): CaM lobe-to-RyRp intermolecular distances. Ribbon diagrams produced with PyMOL (www.pymol.org) show CaM N-lobe blue, CaM C-lobe gray, RyRp yellow, spin labels (modeled as in [76]) red. (a) CaCaM (PDB: 1CLL) [3]. (b) apoCaM (PDB: 1CFD) [77]. (c and e): CaCaM/RyRp complex (PDB: 2BCX) [30]. (d and f) No high-resolution structures have been reported for apoCaM/RyRp complex. **For a-d, CaM was labeled with BSL (h) in the N lobe (T34C, S38C) and in the C-lobe (R106C, T110C). *For e and f, RyRp was labeled with TOAC (g) at position 5, and CaM was labeled with BSL (h) in the N lobe (distance a) or C lobe (distance b).

structural state. While NMR can provide evidence for structural heterogeneity and dynamics, reliable structure determination by NMR typically requires population of a single well-defined structural state. CaM is a flexible signaling protein with a versatile repertoire of structural and functional states, influenced by the binding of Ca and target proteins. The challenge remains to detect and resolve these dynamic structural changes. Distance measurements between spin or fluorescent probes can resolve multiple protein structural states, based on specific techniques in EPR (DEER, double electron-electron resonance, e.g. [86]) or fluorescence (TR-FRET, time-resolved fluorescence resonance energy transfer; e.g. [87]).

We previously used DEER to measure the distribution of interspin distances on CaM spin-labeled at positions T117C (C-lobe) and T34C (N-lobe). That work showed that both in the presence and absence of bound Ca, CaM simultaneously populates both closed (4 nm lobe separation) and open (6 nm lobe separation) structural states, with Ca shifting the equilibrium to the open state [39]. However, it was not possible to compare the structures in that work rigorously with the previously obtained high-resolution structures, because the spin labels used were conventional probes flexibly attached to single Cys residues.

Therefore, in the present study we have employed “stereospecific” spin labels that offer rigid and specific attachment relative to the peptide backbone. For RyRp, we used solid-phase peptide synthesis to incorporate TOAC, a spin-labeled amino acid in which the nitroxide-containing piperidine ring includes the α-carbon (Fig. 1g) and thus directly reports backbone structural dynamics [88, 47, 89]. Although TOAC is an unnatural amino acid from the family of Cα,α-disubstituted glycines [90], it has been shown to have

very useful applications for analyzing peptide backbone dynamics [88, 47, 89, 91]. In recent work, we used EPR of TOAC to detect the Ca-dependent structural dynamics of spin-labeled RyRp bound to CaM [91]. We showed that the structural dynamics of the CaM-bound RyRp is Ca-dependent and non-uniform along the peptide. While compact and immobilized, TOAC requires incorporation via peptide synthesis, which is usually not feasible for molecular weights above 6 kDa.

Therefore, in the present study, to incorporate spin labels stereospecifically into the 16.7 kDa CaM protein, we used mutagenesis to express double-Cys mutants in the N-lobe and C-lobe and labeled each site with a bifunctional spin label (BSL, 3,4-bis-(methanethio-sulfonylmethyl)-2,2,5,5-tetramethyl-2,5-dihydro-1H-pyrrol-1-yloxy) (Fig. 22h). BSL, like TOAC, offers rigid and specific attachment relative to the peptide backbone [92]. When attached to a helix with Cys residues engineered at i and i+4, BSL attains a well-defined orientation with respect to the helix axis [93], allowing for precise measurement of helix orientation in an oriented sample [76]. The conformational restriction afforded by the second Cys linker also allows for precise (sub-nanometer accuracy) measurement of distance distributions in dipolar EPR experiments, virtually eliminating contributions from probe flexibility in the measured distance distributions [94]. The present study is the first report in which TOAC and BSL have been used together to measure distances within a protein complex.

The principal technique used in the present study is DEER, which is most sensitive to interspin distances from 2 to 8 nm but has been shown to successfully measure distances up to 16 nm [95]. DEER has sufficient resolution to detect multiple distances simultaneously, quantitating their mean values, disorder, and populations [96,

97]. Here we have used DEER to determine (a) the intramolecular lobe-to-lobe distance between the two BSL as a function of Ca and RyRp binding (Fig. 22a-d), and (b) the intermolecular distance between singly labeled N-lobe or C-lobe BSL-CaM and TOAC-labeled RyRp (Fig. 22e and f). This study also employed continuous wave (CW) dipolar EPR, which is sensitive to distances between 0.8 and 2.0 nm [98], to provide additional information on shorter distances. The results provide new structural insight into the Ca-dependent interactions of CaM and RyR.

5.3 RESULTS

Distance Prediction and Data Simulation from CaM Structural Models Reveal Ideal BSL Sites for DEER. To determine optimal labeling sites for this study, DEER simulations were performed with BSL attached to different pairs of double-Cys mutations in the N- and C-lobes of CaM. The goal was to select a pair of BSL labeling sites to distinguish the previously proposed structural models: closed by NMR [77], open by X-ray crystallography [3], and compact by X-ray crystallography [30]. To achieve this, we required each BSL-labeled Cys residue to be on a stable α-helix and solvent-exposed, as shown in the proposed structural models (Fig. 22a-c). Fig. 23 shows simulated DEER data for the optimized pair of BSL labeling sites in CaM, based on spin-labeled structural models in Fig. 22. The open model (5.7 nm) generates a DEER waveform with a slow decay and oscillation. The closed model (4.3 nm) generates a faster decay, and the compact model (2.6 nm) yields the fastest, consistent with a short distance on the lower end of DEER's sensitivity range. All three structural states should be clearly distinguishable and resolved by DEER (Fig. 23).

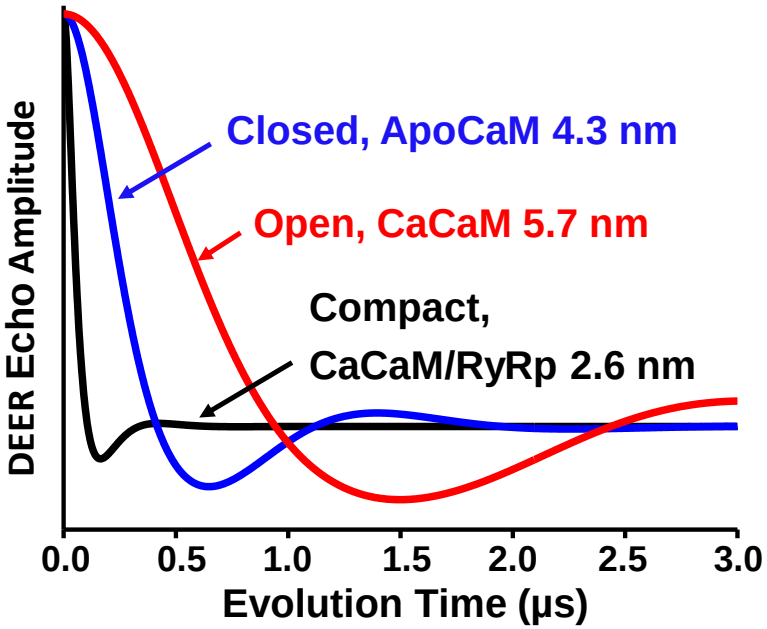

Fig. 23. Simulations of DEER waveforms, based on distance predictions from structural models in Fig. 22, show that the three structural states of CaM should be clearly distinguished and resolved, with labeling sites at T34CS38C in the N lobe and R106CT110C in the C lobe. Each simulation assumed a Gaussian distance distribution with a width (FWHM) of 1.0 nm.

DEER Resolves Ca-dependent Structural States of CaM in Solution. We measured four different conditions of double-labeled BSL-CaM with predicted lobe-to-lobe internitroxide distances in the range of 2–6 nm (Fig. 2). Fig. 24a shows the results (data in black) of the background-corrected echo decay along with the corresponding best fits (blue for apoCaM and red for CaCaM). Fig. 24b shows the distance distributions computed via Tikhonov regularization. ApoCaM (Fig. 24a, blue) yields a DEER waveform with a single predominant oscillation frequency, indicating a single major population. Calculation of the apoCaM distance distribution (Fig. 24b, blue) reveals the

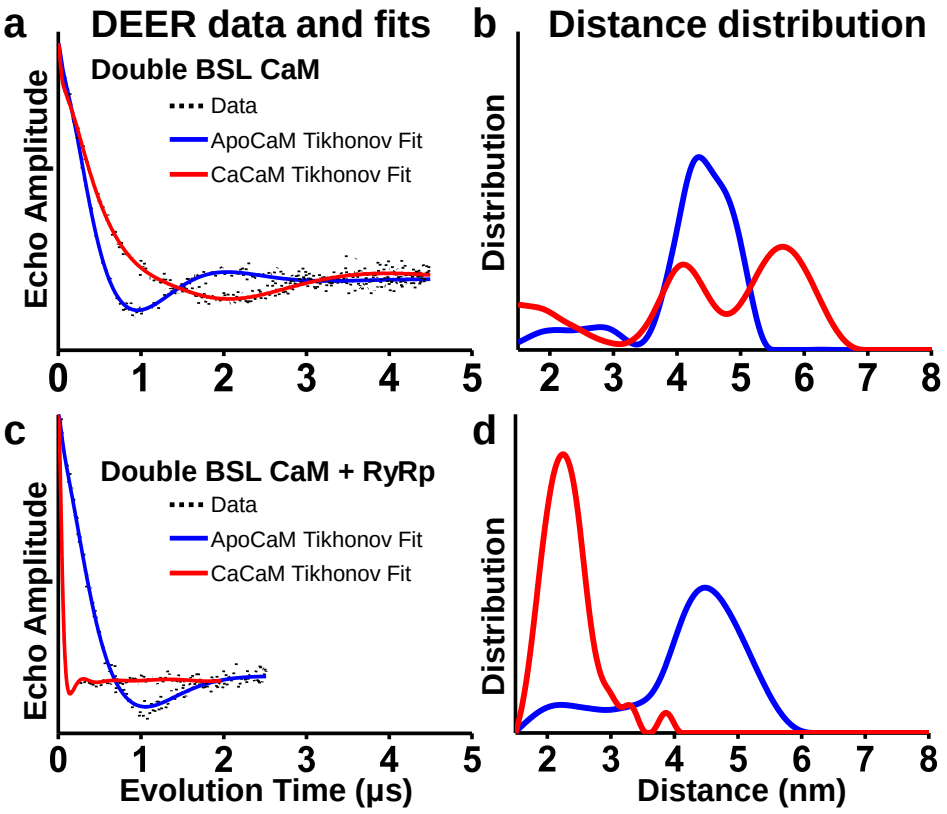

Fig. 24. Intramolecular (lobe-to-lobe within CaM) DEER distance measurements resolving the Ca-dependent structural states (compact, closed and open) of double-labeled BSL-CaM**,** in the absence of Ca (blue, apo) or presence of saturating Ca (red). CaM was labeled at positions T34CS38C in the N-lobe and R106CT110C in the C-lobe. (a,b) DEER waveforms (black), best fits and distance distributions from Tikhonov regularization (blue/red) for double BSL-CaM (Fig. 22a,b). (c,d) DEER waveforms (black), best fits and distance distributions from Tikhonov regularization (blue/red) for the complex of double BSL-CaM and RyRp (Fig. 22c,d).

existence of one predominant population, having a distance centered between 4 and 5 nm, in excellent agreement with the predicted distance of 4.3 nm (Fig. 23, blue, from the NMR structure [77]). The fit also revealed a small fraction with a center distance between 2 and 3 nm, suggesting that apoCaM exists in equilibrium between the closed and compact states (2.6 nm, Fig. 23 black). The addition of Ca resulted in a DEER waveform with a much slower initial decay and longer period of oscillation (Fig. 24a, red), clearly indicating an increased distance. Analysis (Fig. 24b, red) confirms that the most populated component corresponds to a much longer distance (between 5 and 6 nm), in excellent agreement with the open structural state (5.7 nm, Fig. 23 red, from the crystal structure of CaCaM [3]). The width of this peak is relatively broad, perhaps from the central linker being highly mobile and allowing for the two lobe domains to tumble almost independently of one another as previously reported [6]. The width (and mole fraction) of this portion of the distribution is tightly coupled to choice of background component and is therefore less certain than the distance (Fig. S29). Furthermore, two additional structural states are clearly resolved by DEER, one at ~4 nm, in good agreement with the predicted closed state (4.3 nm, Fig. 23 blue); and another ~2 nm (near the short distance limit of DEER), in good agreement with the predicted compact state (2.6 nm, Fig. 23, black). *Thus DEER reveals for the first time that in the presence of Ca, CaM exists in equilibrium among all three previously detected structural states*. This is the first evidence for CaCaM having a significant population in the closed state (previously observed only for the NMR structure of apoCaM [3]), or the compact state (previously observed only once for the crystal structure of CaCaM alone [79] and CaM bound to a target peptide such as RyRp [30]**)**.

RyRp Binding to CaM Occurs through a Conformational Selection Mechanism. The above results strongly support a *conformational selection* mechanism, in which CaM binding to a target protein occurs through ‘‘selection’’ of pre-existing CaM conformations [99]. To test this hypothesis further, with respect to the CaM/RyR interaction, we performed DEER measurements on double labeled BSL-CaM bound to unlabeled RyRp (Fig. 24c and d). In the absence of Ca, the DEER waveform is unaffected by RyRp binding (Fig. 24c, blue). Analysis (Fig. 24d, blue) confirmed that apoCaM remains predominantly in the closed state (4-5 nm), consistent with the closed state observed in the absence of RyRp (4-5 nm, Fig. 24b, blue). A much more dramatic effect of RyRp is observed in the presence of Ca: the DEER waveform shows a much faster initial decay (Fig. 24c red) than in the absence of RyRp (Fig. 24a, red), indicating a substantial decrease in the interlobe distance. Indeed, the observed waveform is in excellent agreement with that predicted (Fig. 23 black, 2.6 nm) by the compact state of the CaCaM/RyRp complex (Fig. 22c). Thus our DEER results clearly support a conformational selection mechanism, in which the addition of RyRp to CaCaM shifts the structural equilibrium toward the compact state, with little to no effect on apoCaM.

Ca Stabilizes the Compact State by Increasing Binding of the CaM N-lobe to RyRp. To further characterize the conformational selection mechanism of CaM binding to RyRp, we used DEER and dipolar CW-EPR to measure the Ca-dependent distance distribution between BSL on the N-lobe and TOAC on RyRp. Fig. 25a shows the results (data in black) of the background-corrected DEER echo decays along with the corresponding best fits (blue for apoCaM and red for CaCaM). Inspection of the data for apoCaM reveals a DEER waveform with dampened oscillations, consistent with a broad distance distribution and thus disorder. Indeed, determination of the distance distribution reveals the presence of two overlapping populations with the center distances of one

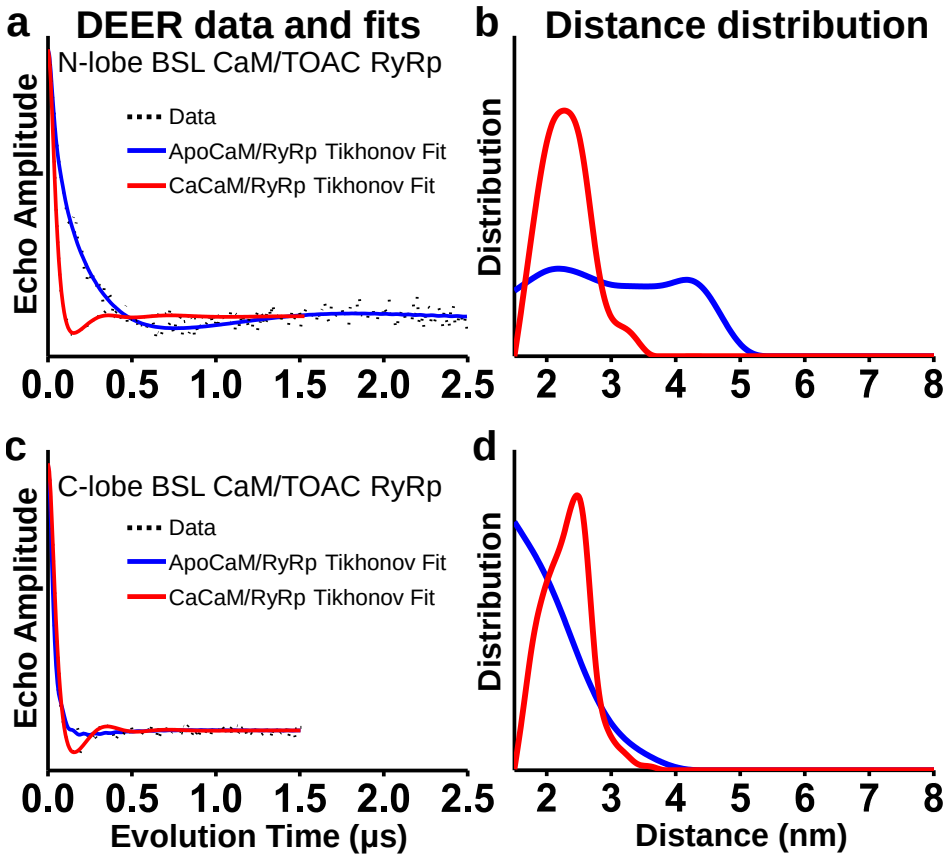

Fig. 25. Intermolecular (between CaM and RyRp) DEER distance measurements resolving the Ca-dependent structural states of the CaM/RyRp complex**,** in the absence of Ca (blue, apo, Fig. 22f) or presence of saturating Ca (red, Ca, Fig. 22e). Distance measurements were made between 5-TOAC-RyRp and N-lobe BSL-CaM (a and b), and 5-TOAC-RyRp and C-lobe BSL-CaM (c and d).

between 2 and 3 nm, and the other between 4 and 5 nm (Fig. 25b, blue). The addition of Ca resulted in a much faster initial decay and a shorter period of oscillation (Fig. 25a, red), indicating decreased distance and increased order. Analysis revealed one predominant compact state with a center distance between 2 and 3 nm (Fig. 25b, red), consistent with the shorter of the two populations observed in the absence of Ca (Fig. 25b, blue). Thus, supporting the conformational selection model, Ca stabilizes the pre-existing compact state, probably by increased binding of the N-lobe of CaM to RyRp.

C-lobe of CaM Binds to RyRp Independent of Ca. We performed analogous experiments with BSL on the C-lobe of CaM and TOAC on RyRp (Fig. 25c and d). In contrast with the N-lobe experiments, the effect of Ca is small, with rapid decays indicating short distances in both cases, although there is more disorder in the absence of Ca. Thus, our DEER results are consistent with the hypothesis that the C-lobe of CaM remains bound to RyRp independent of Ca [71, 42, 91], and the largest effect of Ca is mainly to increase the order of the C-lobe with respect to RyRp.

Dipolar CW EPR Confirms the Existence of Populations with Short Interprobe Distances. Intermolecular DEER measurements between BSL-CaM and TOAC-RyRp resulted in populations near or below the 2.0 nm limit of DEER sensitivity (Fig. 25b and d). To evaluate whether there were significant populations below this limit, we performed dipolar CW EPR on all BSL-CaM/TOAC-RyRp samples (Fig. S33). N-lobe BSL-CaM in complex with TOAC-RyRp reveals minimal broadening in the dipolar spectrum in the presence of Ca (Fig. S33, red), while no significant broadening was observed in its

absence (Fig. S33a, blue). With BSL on the C-lobe, minimal broadening was observed in the absence of Ca but not in its presence (Fig. S33d), and no distances substantially shorter than 2 nm were detected. These results are entirely consistent with the DEER results discussed above, indicating that DEER accurately captured all relevant structural states in this system.

5.4 DISCUSSION

This is the first report in which two different stereospecific spin labels have been used together in a single EPR study. We used peptide synthesis and mutagenesis to introduce TOAC and BSL, respectively. We demonstrated that these spin labels, which offer *rigid and specific attachment relative to the protein backbone*, are powerful probes to detect and resolve structural states. TOAC reflects backbone dynamics directly [88, 89, 100, 91]. BSL is an alternative to TOAC that can be applied to larger proteins, as long as Cys residues can be engineered at i and i+4 on an α-helix [93, 76, 101, 94]. These labels provide a substantial advantage over conventional methods of site-directed spin labeling, in which the attachment of probes to single Cys side chains leave several flexible bonds between the α-carbon and the nitroxide group, thus leaving considerable ambiguity about the interpretation of the spectra.

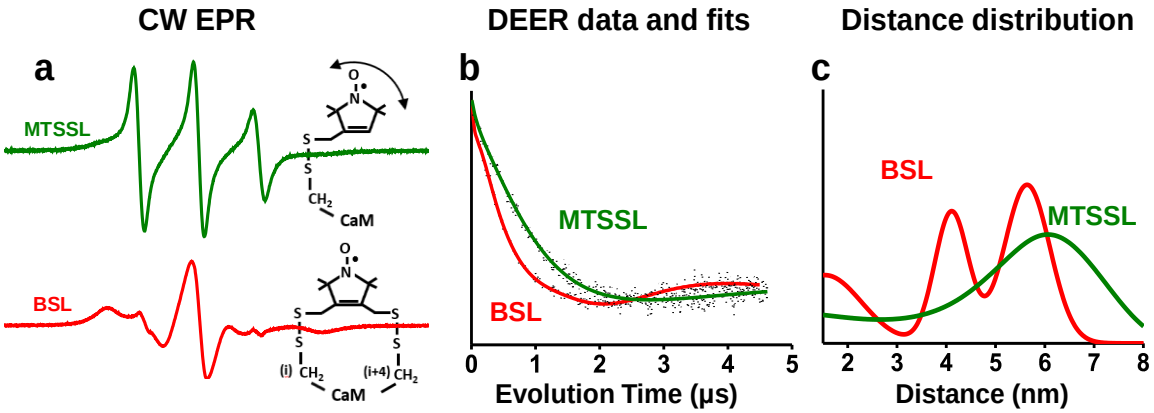

Fig. 26. Comparison of MTSSL (green) and BSL (red) in detecting backbone dynamics and distance distributions within CaM. (a) CW EPR spectra at 4 °C, showing that BSL (labeled at position T34CS38C) is strongly immobilized (broad spectrum) on CaM, accurately detecting backbone dynamics, while MTSSL (labeled at position T34C) is weakly immobilized, indicating spin label flexibility (double-headed arrow). (b) Background-corrected DEER echo decay of double BSL-CaCaM (T34CS38C-R106CT110C) and double MTSSL-CaCaM (T34C-T110C). (c) DEER distance distributions demonstrating the resolving power of BSL. MTSSL reveals two unresolved, broad distance distributions (green) while BSL reveals three distinct distance populations (red). CW EPR spectra in A were obtained with a 120 G scan width, then normalized to unit spin concentration by dividing by the double integral.

These points are illustrated clearly in Fig. 26, which compares the CW EPR and DEER results for MTSSL-CaM with those of BSL-CaM labeled at the same position. The BSL CW spectrum is much broader than that of MTSSL, indicating greatly reduced nanosecond probe motion and disorder (Fig. 26a). The spectrum of BSL-CaM indicates a rotational correlation time of 8 ± 2 ns, consistent with the global tumbling of CaM [102] and the rigid attachment of the probe to the peptide backbone. The spectrum of MTSSL-CaM indicates a rotational correlation time less than 1 ns [102], consistent with flexible attachment of the probe. The DEER waveform of BSL-CaM shows clear oscillations (Fig. 26b, red) and resolves three distinct structural states (Fig. 26c, red), while MTSSL shows no discernable oscillation (Fig. 26b, green) and yields a broad distance distribution (Fig. 26c, green). Thus BSL is clearly superior to MTSSL for accurately reflecting the dynamics and locations of backbone atoms, and resolving the structural states of the complex.

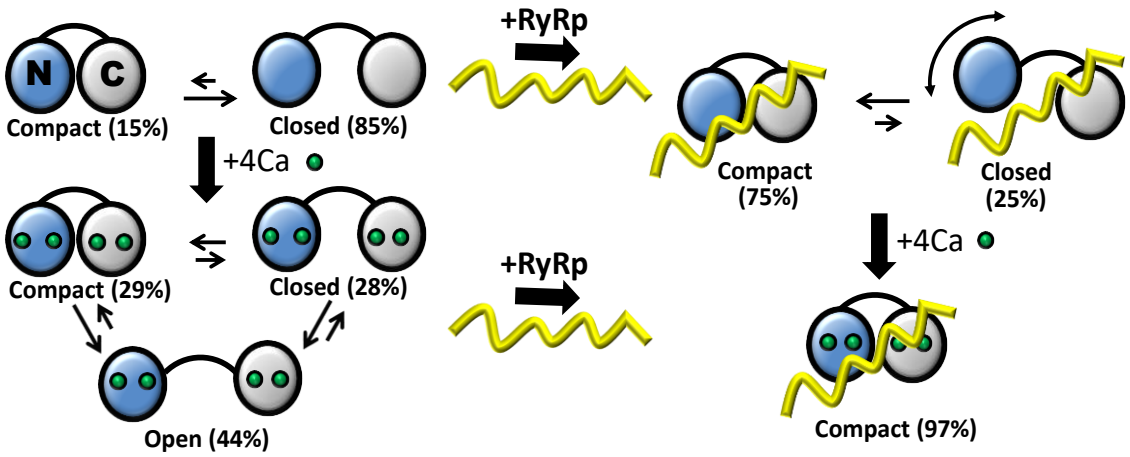

Fig. 27. Schematic of structural models based on DEER distance measurements (Fig. 24**,** Fig. 25). Blue, N-lobe of CaM; gray, C-lobe of CaM; yellow, RyRp; green, Ca ion. In the absence of RyRp and Ca (upper left) CaM is primarily in the closed structural state. Ca binding to CaM (bottom left) populates all three states (open, closed, compact), with the open state predominant. In the presence of RyRp and the absence of Ca (upper right), the complex is in dynamic equilibrium between the compact state, and a closed-like state with the N-lobe potentially being highly mobile and not bound to RyRp. Ca binding to CaM (bottom right) shifts the complex almost completely to the compact state by increasing binding of the N-lobe to RyRp.

Fig. 27 illustrates a model for the conformational selection mechanism of CaM binding to RyRp, as supported by our intraCaM DEER results (Fig. 24) and previous studies of CaM binding to other target peptides [103-105]. In addition, we report for the first time direct high-resolution structural measurements on the apoCaM/RyRp complex (Fig. 24c and d, blue; Fig. 25 blue), allowing us to propose a structural model for this complex (Fig. 22d and f), providing new structural insight into the Ca-dependent interaction of CaM and RyR.

As the resultant distributions reveal distinct subpopulations, we further parameterized the waveforms by fitting the background-corrected echo decays to a sum of Gaussians model, in order to extract mole fractions and ascertain the uncertainty of the fit parameters, as described in *Materials and Methods* and in *Supplemental Information* (Fig. S29 Fig. S30 Fig. S32**;** Table S4 Table S5). While quantitative analyses from Gaussian modeling may yield numerical values with high uncertainty, especially for distances near the sensitivity limits of DEER, they do nevertheless provide valuable

insight into the observed population changes caused by Ca and RyRp binding. In addition to uncertainty found in the error surface of the fit (Fig. S32 and Table S4 Table S5) and the appropriateness of model choice, several experimental factors warrant interpreting both the parameterized and Tikhonov distance distributions with caution. In the case of short distances (≤ 3 nm), limits in our excitation bandwidth result in errors in population center and fraction due to incomplete excitation of short distance spin-pairs [106]. For longer distances, experimental constraints limit our maximal evolution time (which determines the maximum resolvable distance [97], see Fig. S29 Fig. S30 Fig. S31), allowing for the potential of un-resolved populations and errors in population width and therefore fraction near the sensitivity limit.

In the absence of RyRp and Ca, apoCaM exists in equilibrium between a predominantly closed state (85%, consistent with the NMR structure [77]) and a weakly-populated compact state (15%) (Fig. 27, top left). Ca shifts this distribution to a more complex one (Fig. 27, bottom left), in which CaCaM exists in structural equilibrium among three distinct structural states: compact (29%), closed (28%) and open (44%). CaCaM has a diverse array of binding modes to over 300 targets [107]; probably facilitated by the complex conformational equilibrium reported here. RyRp binding to CaCaM induced an almost complete structural equilibrium shift toward a compact structure (Fig. 27, bottom right) consistent with the X-ray crystal structure CaCaM/RyRp complex [30]. Fig. 27 (top right), illustrates the new proposed structural model of the apoCaM/RyRp complex, which is primarily in equilibrium between compact (75%) and closed (25%) structural states, while addition of Ca shifts the equilibrium almost completely toward the compact state (97%). The compact state of CaCaM/RyRp was

previously reported by X-ray crystallography [30], but here, we show directly for the first time the structural transition from the compact (75%) and closed (25%) states in the absence of Ca to a single compact state (97%) of the CaM/RyRp complex upon addition of Ca.

At first glance, the addition of RyRp has no effect on the lobe-lobe distance in apoCaM (Fig. 24b and d, blue; Table S4), suggesting that RyRp may not be binding CaM in the absence of Ca. However, two lines of evidence indicate that there is at least partial binding between apoCaM and RyRp, and Ca is required for maximum binding, as supported by our DEER measurements. First, binding has been detected in the absence of Ca by several investigations at a lower affinity than in the presence of Ca [71, 42, 43]. Second, we have previously shown by CW EPR that TOAC-labeled RyRp was only partially immobilized by apoCaM while CaCaM led to complete immobilization of the peptide [91]. These observations led us to try to detect the presence of binding, although potentially weak, by labeling the lobes of CaM individually with BSL and the RyRp with TOAC through peptide synthesis. In this system, if there were no binding in the absence of Ca, we would not be able to measure any inter-protein DEER distances (Fig. 25, blue), therefore at least some fraction of RyRp is bound to apoCaM. Thus, it is possible that a large fraction of the double BSL apoCaM/RyRp sample is uncomplexed proteins (giving it a distance distribution similar to apoCaM alone), and the DEER signal coming from the BSL N-lobe CaM/TOAC RyRp sample is from a smaller bound fraction (with the labeled CaM and RyRp not in complex contributing merely to the background signal).

Previous investigations by us [91] and others [108, 42, 43], suggest that the N-lobe of CaM is involved in tight binding of CaM to RyRp, and this is important for regulation of

RyR [71]. Our DEER distance measurement between the N-lobe of CaM and RyRp revealed the flexibility and structural heterogeneity of this complex, with two broad distance populations in the absence of Ca (Fig. 25b, blue and Table S5); the major population (75%) corresponds to the compact state. The longer distance population is too long to be explained by the compact state of CaM, so this population probably represents a state where the N-lobe is not bound tightly to RyRp. Addition of Ca shifted the equilibrium to one predominant population with a short distance (Fig. 25b, red and Table S5), indicating complete binding of the N-lobe to RyRp in a compact state. In contrast, distance measurement between the C-lobe of CaM and RyRp indicate that the C-lobe is tightly bound to RyRp independent of Ca (Fig. 25d), with Ca only slightly decreasing the disorder (Table S5). These results are consistent with our previous report in which complete immobilization of the C-terminal region of TOAC-labeled RyRp (by CaM N-lobe) was Ca-dependent, whereas the N-terminal region of RyRp was completely immobilized (by the C-lobe of CaM) independent of Ca [91]. Thus, we present further structural evidence that supports the hypothesis that CaM functions as a subunit of RyR through binding of the C-lobe, and complete interaction of the N-lobe of CaM (in response to increased cytosolic Ca levels) is responsible for maximum inhibition of RyR.

5.5 CONCLUSION

We report a unique approach utilizing a combination of BSL, TOAC, and DEER, to resolve and quantitate the structural states of CaM as affected by Ca and RyRp binding. Our results directly support a conformational selection model of CaM binding to RyRp, which occurs by RyRp shifting the structural equilibrium of CaM toward pre-existing states. We were also able to directly detect and resolve structural states of CaM/RyRp

even in the absence of Ca with sub-nanometer precision, while such high-resolution information is not available from X-ray crystallography or NMR. We detected structural changes in each CaM lobe with respect to RyRp binding, and showed that the N-lobe/RyRp interaction was much more sensitive to Ca than the C-lobe, providing unique structural insight into the mechanism of Ca-dependent CaM-mediated RyR regulation. Finally, we have demonstrated the power of TOAC and BSL in measurement of protein backbone rotational dynamics and interspin distance (Fig. 26). This establishes the power of DEER spectroscopy with stereospecific spin labels as a tool that complements conventional structural techniques. This approach will be powerful in future studies of CaM and other Ca-binding proteins, with important implications for molecular pathology and therapeutic development for muscle disorders.

5.6 METHODS

Computational Approach

The Discovery Studio Visualizer software (windows version 2.5.5.9350) was used to optimize BSL-CaM labeling sites in the N-lobe and C-lobe. For this purpose, PDB files (Fig. 22a. 1CFD, B. 1CLL, C. 2BCX) were individually opened by the software. In the second step two amino acids in the N-lobe and C- lobe at i and i+4 positions were chosen to be mutated to Cys. In the modified PDB files, BSL was attached in the N-lobe (T34CS38C) and C-lobe (R106CT110C). The distances from nitrogen to nitrogen between the attached BSL labels in the N-lobe and C-lobe were determined (Fig. 22a-d). The shorter distance from the singly labeled BSL- CaM mutant (T34CS38C) to 5-TOAC-RyRp (TOAC substituted for Ala5) was accomplished in a similar way, by using the

modified PDB file 2BCX (Fig. 22e and f). The estimated distances were then used to simulate the expected DEER waveforms (Fig. 23) using WACY, an in-house laboratory developed EPR software (Edmund Howard).

CaM Mutagenesis and Purification

Tetra-Cys CaM was engineered containing two Cys in the N-lobe (T34CS38C) and C-lobe (R106CT110C) followed by cross linking with BSL to measure intra-molecular distances by DEER. Di-Cys CaM mutants (T34CS38C or R106CT110C) were also expressed and purified for experiments involving inter-protein distance measurement with TOAC labeled RyRp. In detail, recombinant human CaM was expressed in *Escherichia coli* using the pET-7 vector [109]. Mutations targeting the Cys labeling sites were introduced using the QuikChange mutagenesis kit (Stratagene, La Jolla, CA), and the mutation was verified by DNA sequencing. Following induction with isopropyl β-D-1-thiogalactopyraoside, di- and tetra-Cys-CaM were purified via phenyl-Sepharose chromatography [110]. Protein concentrations were determined by the bicinchoninic acid procedure (Pierce, Rockford, IL) using bovine brain CaM as the standard [111].

BSL-CaM Spin Labeling

BSL-CaM spin labeling was accomplished by first reducing the protein with 5 mM DTT for one hour at room temperature. DTT was removed using Zeba Spin desalting columns (Thermo Scientific) and the reduced CaM sample then incubated with 4x molar excess BSL (Toronto Research Chemicals) at 4 °C overnight. Excess BSL was removed and the protein was exchanged into EPR buffer (20mM MOPS, 5mM Ca or 5 mM EGTA, pH

7.4) using a Zeba Spin desalting column. Spin counting results showed that ≥80 of BSL-CaM were labeled.

Synthesis of TOAC-RyRp and RyRp

RyRp and TOAC-RyRp (with TOAC substituted for Ala5) were synthesized by solid-phase peptide synthesis (SPPS) as previously described [91]. Spin counting results showed that ≥60 of TOAC-RyRp were labeled. Cys22 was replaced with α-amino-n-butyric acid (Abu) to prevent disulfide exchange with BSL labeled CaM. EPR studies of BSL labeled CaM with WT-RyRp (Cys 22 instead of Abu) caused the appearance of a highly mobile spectral component, corresponding to free spin label. BSL labeled CaM showed only 41% spin labeling efficiency. The most likely interpretation of the free BSL label is that the Cys residue of WT-RyRp participates in disulfide exchange with BSL-CaM as previously reported [112]. BSL is a sulfhydryl-reactive cross linker and linked by disulfide bonds to the –SH peptide side chain. The reaction between pairs of free or reduced sulfhydryl groups (-SH) is selective and precise. To control the number of free –SH groups we replaced Cys22 with Abu.

CD Spectroscopy

CD spectra were acquired at 22 °C with a JASCO J-815 spectrophotometer, scanning from 190 nm to 260 nm with a scan rate of 50 nm/min, 0.1 nm bandwidth. Spectra were signal-averaged five times and baseline subtracted. Reported spectra are expressed as mean residue ellipticity, [θ]. Linear combinations of α-helix, β-sheet and random coil bases spectra were used to determine secondary contributions from fits to acquired CD

spectra [113, 68]. Samples for CD consisted of 20 μM CaM, BSL-CaM or double BSL-CaM in 10 mM Na_2HPO_4, pH 7.4, loaded into quartz cuvettes with a path length of 0.1 cm. We previously reported that TOAC labeling of RyRp does not significantly alter its secondary structure and how it responds to the alpha-helix inducer TFE [91]. We performed CD on BSL labeled CaM mutants and show that single (T34CS38C) and double labeled BSL-CaM (T34CS38CR106CT110C) does not significantly alter the secondary structure compared to wild-type CaM (Fig. S28). The linear fit of the CD spectrum yielded 90.3% α-helix for WT-CaM, 89.8% for single BSL-CaM and 88.1% for double BSL-CaM (Fig. S28).

EPR Spectroscopy and Data Analysis

We performed DEER to measure distances from 2 to 6 nm, and dipolar CW-EPR for distances from 0.5 to 2 nm. DEER signals were acquired with an Elexsys E580 spectrometer (Bruker) operating at Q-band (34 GHz) equipped with a EN5107 resonator using a four-pulse DEER sequence [97] with a 12 ns π/2 pulse and a 24 ns ELDOR pulse. The spacing between the echo forming π/2 and π pulses was incremented in 8 steps of 16 ns to average out D_2O artifacts [97]. The pump frequency was assigned to the maximum of the nitroxide absorption spectrum and the observe frequency placed at a 24 Gauss higher magnetic field strength on the field swept absorption spectrum. Data was acquired at 65 K and lasted 16–24 hours. All DEER samples contained 90-100 μM CaM in 20 mM MOPS, pH 7.4, 95% D_2O. 10% glycerol was added for cryoprotection. Samples containing RyRp had a ratio of 1.25:1 (peptide:CaM). DEER waveforms were analyzed using custom software written in Mathematica based on DeerAnalysis [114] and DEFit

[115] (github.com/thompsar). Background corrected waveforms were analyzed using Tikhonov regularization, with choice of smoothing parameter informed by both the l-curve and leave one out cross validation (LOOCV) criteria [116]. After stable populations were identified via a systematic variation of the region fit for the background component (similar to DeerAnalysis' validation tool), highly unstable populations that were well separated from the primary distribution (and beyond the sensitivity range afforded by acquired evolution time) were suppressed by repeating background correction with the appropriate spectral components included as a correction to the initial homogeneous background model, followed again by Tikhonov regularization. The resultant filtered Tikhonov distribution (which showed no distortion beyond the suppression of the unstable components) was then used as seed for a Monte Carlo fit of the waveform using a sum of Gaussians model, $\rho_j(R)$, determining population centers, widths and mole fractions as well as their respective uncertainties with respect to the error surface of the fit (Fig. S32):

$$\rho_j(R) = \frac{1}{\sigma_j\sqrt{2\pi}}\, exp\left(\frac{-\left[R - R_j\right]^2}{2\sigma_j^2}\right) \quad \text{Eq. 4}$$

$$\sigma_j = FWHM_j/\left(2\sqrt{2\, ln\, 2}\right) \quad \text{Eq. 5}$$

where σ is the standard deviation and FWHM is the full width at half maximum of the distribution. The minimal number of Gaussians necessary to produce a satisfactory fit was determined by both a comparison of RMSDs with the Tikhonov fit as well as using Bayesian information criterion [117], which in our experience performs better than the Akaike information criterion [118] at picking the most parsimonious model.

For dipolar CW-EPR measurements of BSL-CaM to 5-TOAC-RyRp, samples were prepared in 20 mM MOPS, pH 7.4, 95% D_2O at a concentration of 90 μM of spin-labeled protein. All CW-EPR spectra were recorded at X-band (9.6 GHz) with a Bruker E500 Elexsys spectrometer equipped with an ER 4122 SHQ resonator. For dipolar EPR spectra acquisition, temperature was maintained at 200 K with a quartz dewar insert and nitrogen gas flow temperature controller. All frozen spectra were acquired using 0.6 mW power to prevent spin saturation, and 200 G sweep width. All spectra were baseline correct then normalized to the double integral prior to analysis. For determination of spin-spin distance from dipolar CW-EPR spectra of BSL-CaM/5-TOAC-RyRp, spectral simulation and least-square fits were performed as previously described (Fig. S33) [119]. Essentially, experimental spectra were fit to a model corresponding to a sum of Gaussian distance distributions. CW EPR spectra of BSL-CaM at 4 °C were analyzed to determine the rotational correlation time according to Eq. 3 [65]. Each spectrum was analyzed to determine the order parameters S,

$$S = (T_{//}' - T_0)/(T_{//} - T_0), \qquad \text{Eq. 6}$$

where $T_{\|}'$ = splitting between the outer extrema, $T_{\|}$ = the rigid-limit value of $T_{\|}'$ and T_0 = the fast-limit value of $T_{\|}'$. Results indicate no significant detectable differences in CW EPR dynamics between the N- and C-lobes (Table S5).

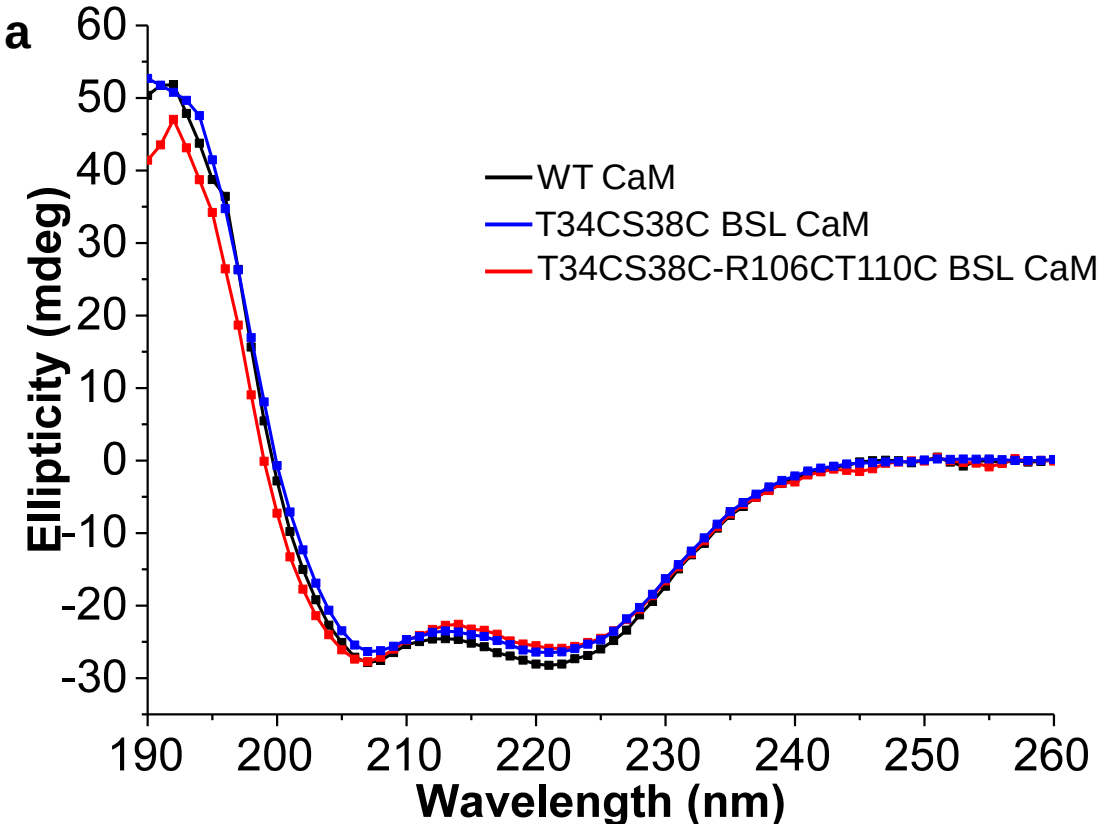

b

Protein	WT unlabeled CaM	T34CS38C BSL CaM	T34CS38C R106CT110C BSL CaM
% α-helix	90.3 ± 0.5 %	89.8 ± 0.6 %	88.1 ± 1.0 %

Fig. S28. CD reveals BSL did not significantly perturb the secondary structure of CaM. **(**a) CD spectra of WT CaM (black), single BSL-CaM (blue) and double BSL-CaM (red). (b) Percent α-helix were determined from data simulation and fitting assuming a linear combination of α-helix, β-sheet and random coil. In either case, BSL labeling did not significantly disrupt the secondary structure of CaM.

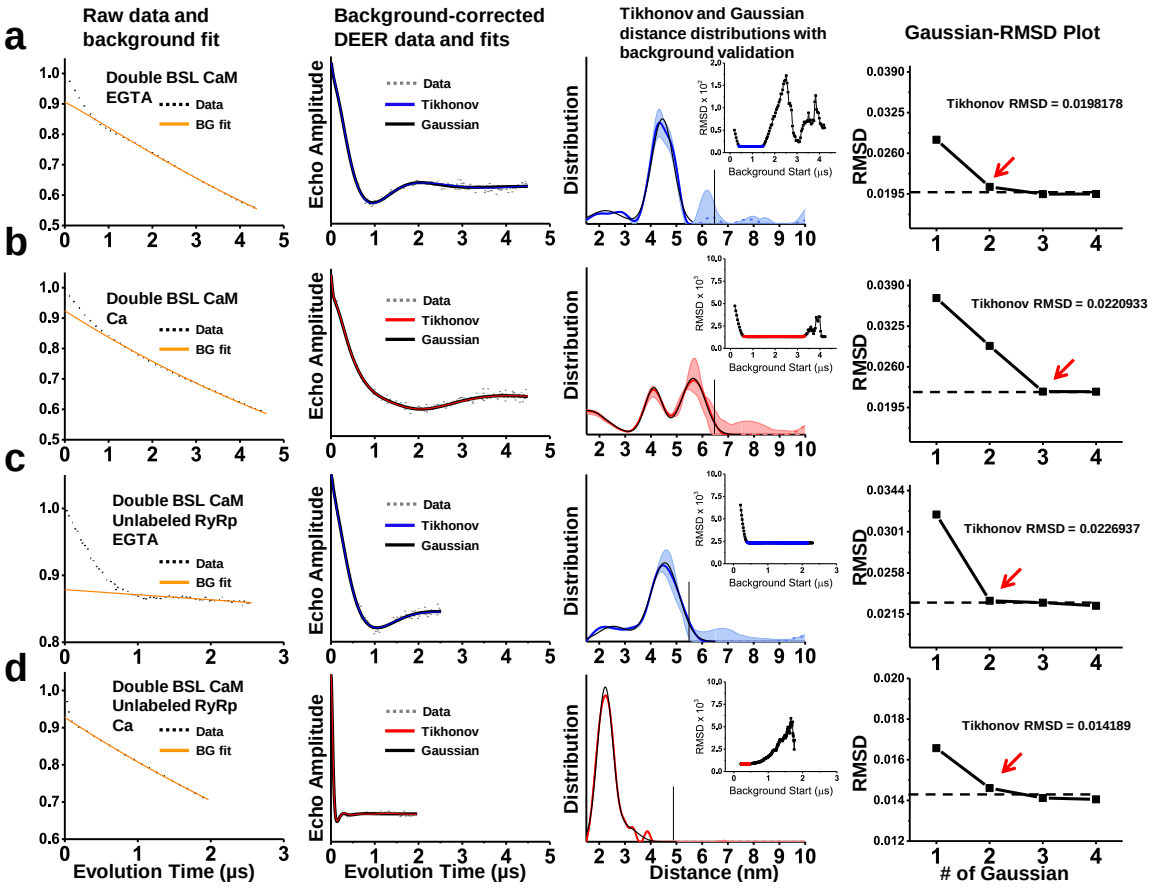

Fig. S29. Analysis of double BSL CaM DEER in the absence of Ca (**a**), presence of saturating Ca (**b**), presence of unlabeled RyRp and no Ca (**c**), and presence of unlabeled RyRp and saturating Ca (**d**). *First column* shows the raw data (black dots) and background fit (orange). *Second column* shows the background-corrected data (gray dots, using the shown homogenous background model augmented with the selected long range distance components), Tikhonov fits (red/blue), and best Gaussian fits (black). *Third column* shows Tikhonov distance distribution (red/blue), 95% CIs from background validation (shaded), and Monte Carlo sum of Gaussians model (black). Unstable populations (dashed) were suppressed from the primary distribution (solid) by a via modification of the background model as described with no distortion to the primary distribution shown here and in Fig. 24 in the manuscript. The primary Tikhonov distribution was then used as a seed for a Monte Carlo fit of the waveform using a sum of Gaussians model shown here (black). Insets show range of background validation RMSD with selections in red/blue. The vertical line indicates the maximum reliable mean detectible distance given the waveform's evolution time (Ref. 31 in main text). *Fourth column* shows the refinement of the Gaussian model, with the red arrow in the RMSD-Gaussian plot showing the number of Gaussians sufficient to fit the data (n), at which n + 1 did not significantly improve the fit, informed by Bayesian information criterion. See Materials and Methods for more details.

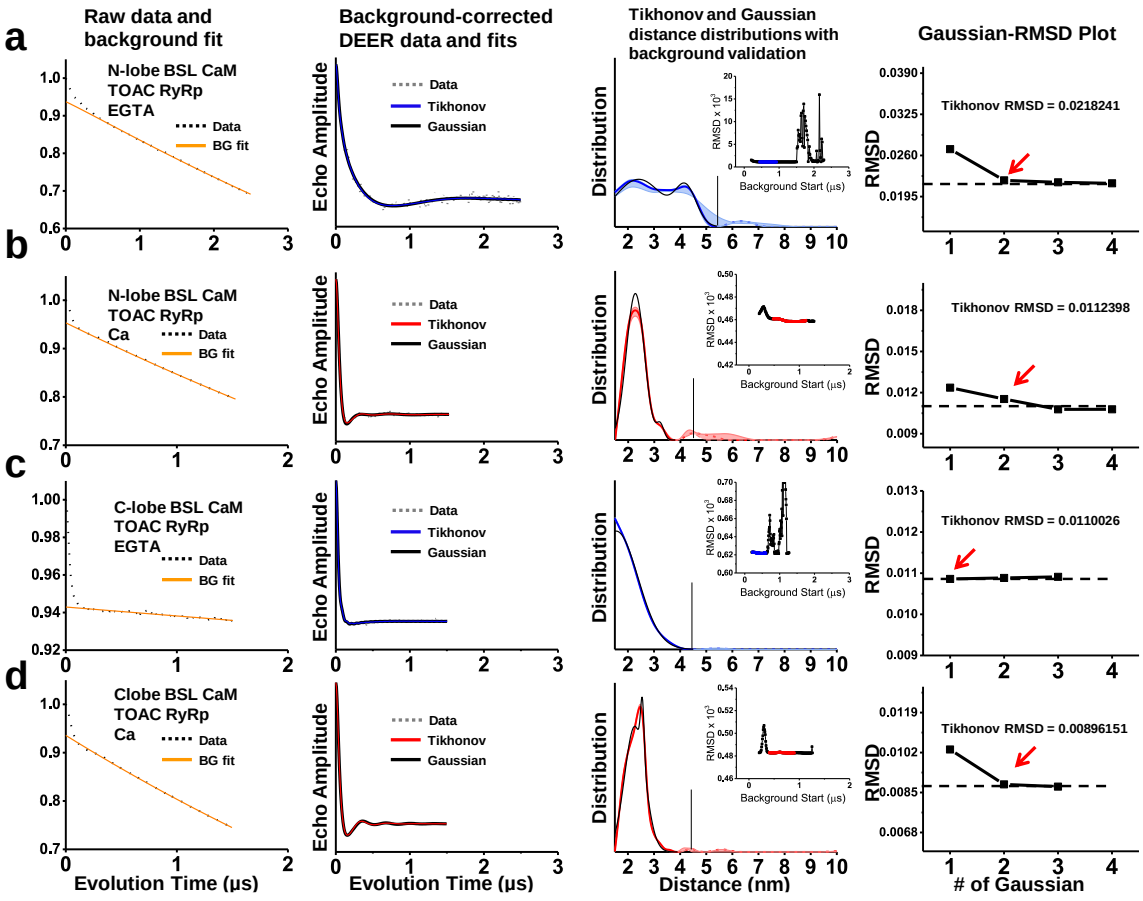

Fig. S30. Analysis of BSL-CaM/TOAC-RyRp DEER. Distances measured were between N-lobe BSL CaM and TOAC RyRp in the absence of Ca (**a**), N-lobe BSL CaM and TOAC RyRp in the presence of saturating Ca (**b**), C-lobe BSL CaM and TOAC RyRp in the absence of Ca (**c**), and C-lobe BSL CaM and TOAC RyRp in the presence of saturating Ca (**d**). *First column* shows the raw data (black dots) and background fit (orange). *Second column* shows the background-corrected data (gray dots, using the shown homogenous background model augmented with the selected long range distance components), Tikhonov fits (red/blue), and best Gaussian fits (black). *Third column* shows Tikhonov distance distribution (red/blue), 95% CIs from background validation (shaded), and Monte Carlo sum of Gaussians model (black). Unstable populations (dashed) were suppressed from the primary distribution (solid) by a via modification of the background model as described with no distortion to the primary distribution shown here and in Fig. 25 in the manuscript. The primary Tikhonov distribution was then used as a seed for a Monte Carlo fit of the waveform using a sum of Gaussians model shown here (black). Insets show range of background validation RMSD with selections in red/blue. The vertical line indicates the maximum reliable mean detectible distance given the waveform's evolution time (Ref. 31 in main text). *Fourth column* shows the refinement of the Gaussian model, with the red arrow in the RMSD-Gaussian plot showing the number of Gaussians sufficient to fit the data (n), at which n + 1 did not significantly improve the fit, informed by Bayesian information criterion. See Materials and Methods for more details.

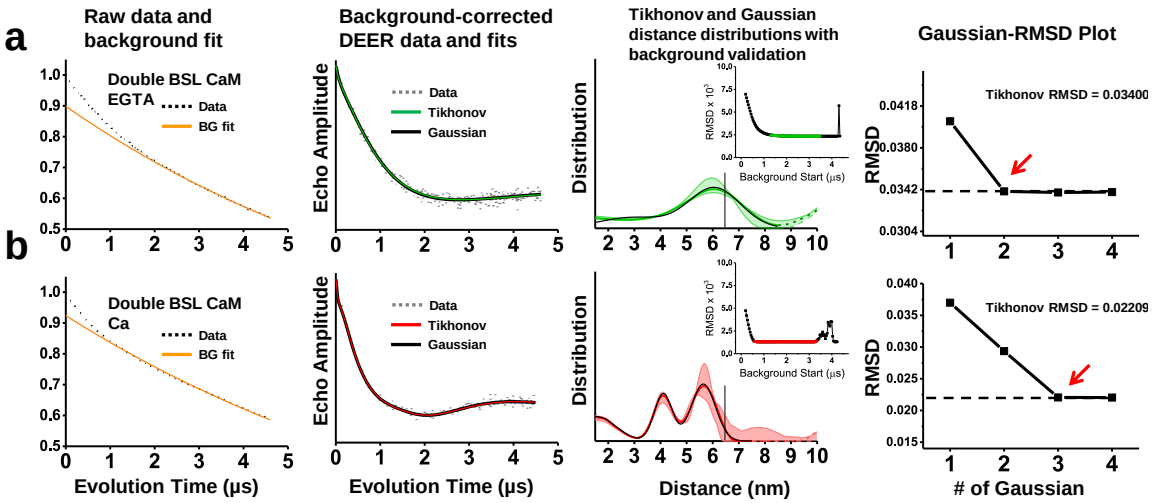

Fig. S31. Analysis of DEER distances measurement of MTSSL CaM and BSL CaM. Analysis hows data for presence of saturating Ca for double MTSSL CaM (**a**) and double BSL CaM (**b**). *First column* shows the raw data (black dots) and background fit (orange). *Second column* shows the background-corrected data (gray dots, using the shown homogenous background model augmented with the selected long range distance components), Tikhonov fits (green/red), and best Gaussian fits (black). *Third column* shows Tikhonov distance distribution (green/red), 95% CIs from background validation (shaded), and Monte Carlo sum of Gaussians model (black). Unstable populations (dashed) were suppressed from the primary distribution (solid) by a via modification of the background model as described with no distortion to the primary distribution shown here and in the manuscript. The primary Tikhonov distribution was then used as a seed for a Monte Carlo fit of the waveform using a sum of Gaussians model shown here (black). Insets show range of background validation RMSD with selections in red/blue. The vertical line indicates the maximum reliable mean detectible distance given the waveform's evolution time (Ref. 31 in main text). *Fourth column* shows the refinement of the Gaussian model, with the red arrow in the RMSD-Gaussian plot showing the number of Gaussians sufficient to fit the data (n), at which n + 1 did not significantly improve the fit, informed by Bayesian information criterion. See Materials and Methods for more details.

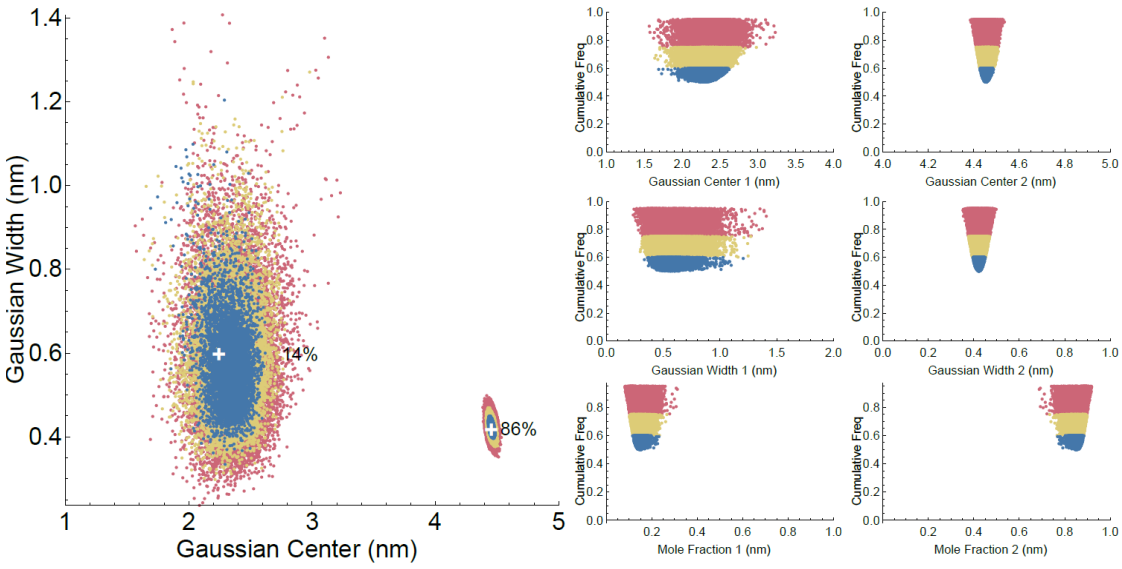

Fig. S32. The Monte Carlo error surface for a 2-Gaussian fit of the double BSL apoCaM sample data, with the centers, widths and mole fractions simultaneously being varied. The 60%, 75% and 95% confidence intervals (blue, yellow, and red, respectively) were determined by a taking a ratio of the residual sum of squares of all fits with the residual sum of square of the best found fit using the cumulative distribution function of the F-ratio distribution with the appropriate degrees of freedom given the amount of data and the number of varied parameters. White crosses denote the location of the best found fit with the listed mole fractions.

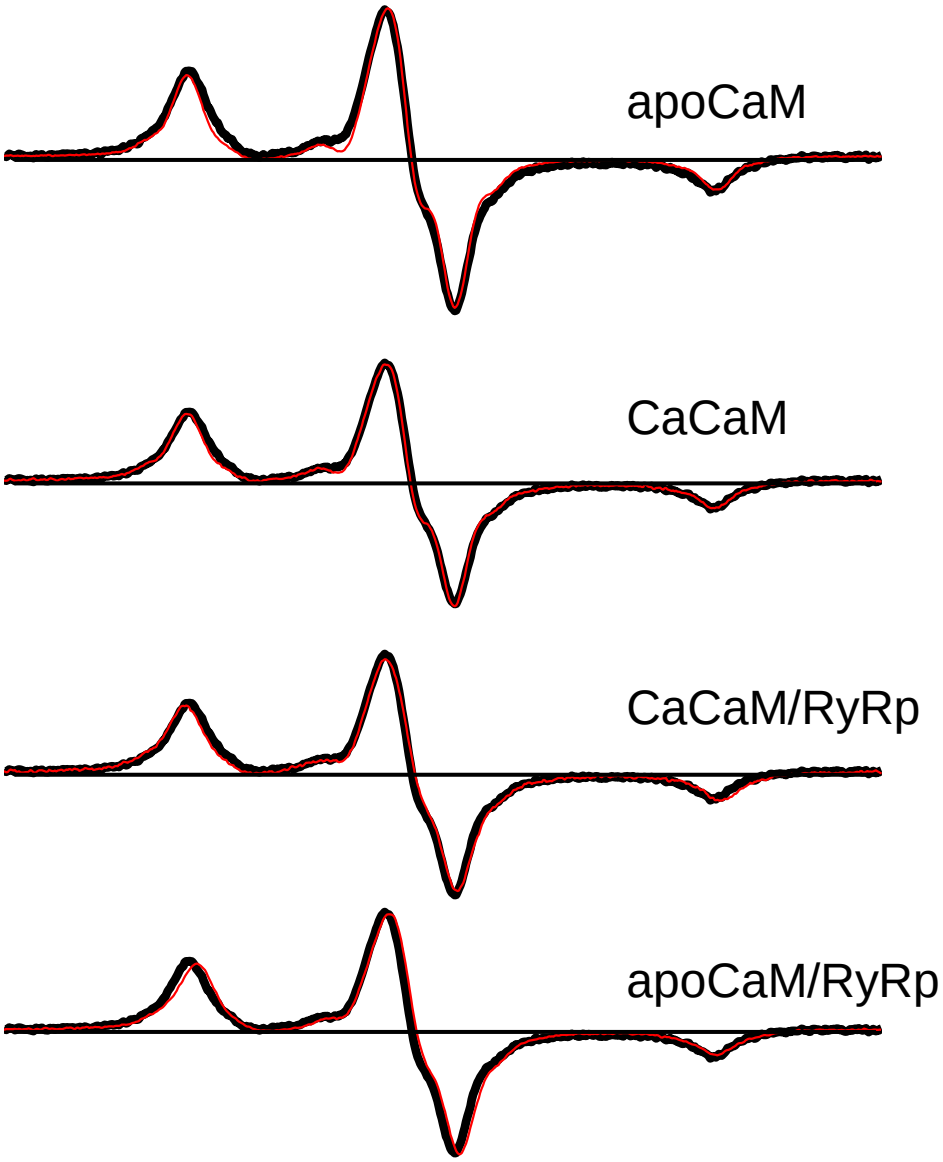

Fig. S33. Dipolar CW EPR of double BSL labeled CaM at positions T34CS38C in the N-lobe and R106CS110C in the C-lobe. Overlay shows double labeled construct (red) with single labeled construct (black), obtained by averaging spectra of the two single labeled samples. The lack of broadening indicates that there is no spin-spin interaction within 2.0 nm in each of the experimental conditions, indicating that all structural states populated by CaM were captured in the DEER measurements. Experiments were performed at 200 K. All spectra are normalized to the spin concentration by dividing by the double integral. Scan width obtained at 200 G (shown as 120 G).

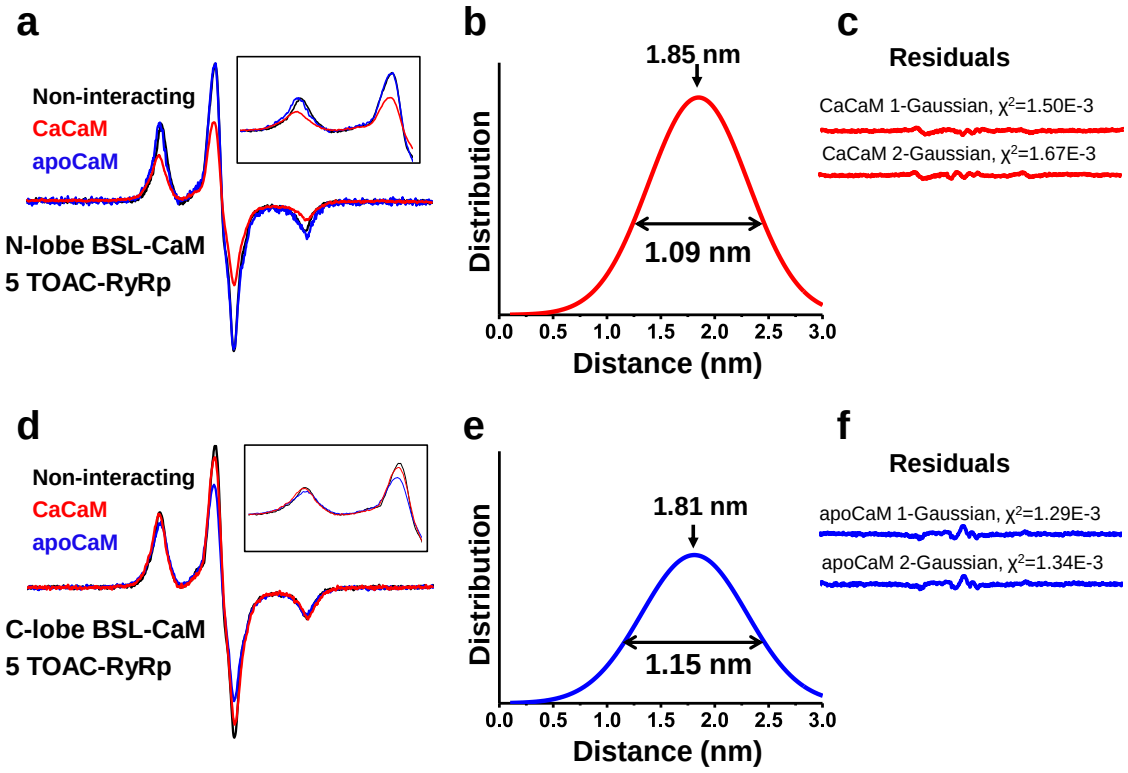

Fig. S34. Analysis of the dipolar CW EPR data of N-lobe (top) or C-lobe (bottom) BSL-CaM/TOAC-RyRp. (a and d) Representative EPR spectra shown at 200 G scan width. Each spectrum has been normalized to the same number of spins by dividing by the double integral. Inset shows expanded view of a 50-G portion of the low-field. The non-interacting spectrum was obtained by averaging spectra of the two singly-labeled samples, prepared from single-Cys mutants. Only the spectrum that showed broadening was analyzed. (b and e) Distance distribution from fits to EPR spectra. (c and f) Residuals show that the data was best fitted to 1-Gaussian distribution in both cases.

Table S4. Interprobe center distances R, FWHM, and percent mole fractions observed in each biochemical state of double labeled BSL-CaM, detected by DEER

Parameter	apoCaM	CaCaM	CaCaM/RyRp	apoCaM/RyRp
Fraction$_1$ (%)	15 ± 12	29 ± 11	87 ± 13	17 ± 11
R_1 (nm)	2.4 ± 0.8	1.6 ± 0.3	2.2 ± 0.1	2.4 ± 0.7
FWHM$_1$ (nm)	1.4 ± 1.4	1.6 ± 0.8	0.7 ± 0.2	1.5 ± 1.2
Fraction$_2$ (%)	85 ± 12	28 ± 10	13 ± 13	83 ± 11
R_2 (nm)	4.5 ± 0.1	4.1 ± 0.2	3.0 ± 0.8	4.5 ± 0.1
FWHM$_2$ (nm)	1.0 ± 0.2	0.8 ± 0.4	1.2 ± 1.2	1.3 ± 0.2
Fraction$_3$ (%)	n/a	44 ± 7	n/a	n/a
R_3 (nm)	n/a	5.7 ± 0.1	n/a	n/a
FWHM$_3$ (nm)	n/a	1.1 ± 0.2	n/a	n/a

R, mean distance; FWHM; full width of the Gaussian distribution at half maximum (*see Materials and Methods* Eq. 5 Eq. 6); Fraction, percent of mole fraction of CaM occupying a given structural state. Subscript indicates population number. Errors represent 95% confidence interval obtained from an F-test of the Monte Carlo search results (see Fig. S32). Experimental conditions are described in *Materials and Methods.*

Table S5. Interprobe center distances R, FWHM, and percent mole fractions observed in each biochemical state of single labeled N-lobe or C-lobe BSL CaM complexed with 5 TOAC RyRp, detected by DEER

Population Parameters	N-lobe -Ca	N-lobe +Ca	C-lobe -Ca	C-lobe +Ca
Fraction$_1$ (%)	75 ± 18	97 ± 8	100 ± 0	89 ± 9
R_1 (nm)	2.3 ± 0.6	2.3 ± 0.1	1.5 ± 0.2	2.2 ± 0.1
FWHM$_1$ (nm)	2.4 ± 1.3	0.8 ± 0.1	2.0 ± 0.3	0.9 ± 0.1
Fraction$_2$ (%)	25 ± 18	3 ± 8	n/a	11 ± 9
R_2 (nm)	4.2 ± 0.2	3.3 ± 0.9	n/a	2.5 ± 0.1
FWHM$_2$ (nm)	1.1 ± 0.5	0.4 ± 0.9	n/a	0.3 ± 0.2

R, mean distance; FWHM; full width of the Gaussian distribution at half maximum (*see Materials and Methods* Eq. 5 Eq. 6.); Fraction, mole fraction of CaM occupying a given structural state. Subscript indicates population number. Errors represent 95% confidence interval obtained from an F-test of the Monte Carlo search results (see Fig. S32). Experimental conditions are described in *Materials and Methods.*

CHAPTER 6: SUMMARY AND FUTURE DIRECTIONS

6.1 SUMMARY

My thesis work has advanced the knowledge of the crucial CaM-RyR interaction. More specifically, the structural mechanism of this interaction was previously vague and not well understood. Below, I go into more details regarding the main discoveries of each of my publication and discuss how it impacted the fields of EPR, CaM-RyR and structural biology in general.

First, in chapter 4 we set out to investigate the structural dynamics of RyRp, the a peptide corresponding to the CaM-binding site on RyR. We synthesized various TOAC-labeled RyRp derivatives and showed using CD that TOAC did not significantly perturb the secondary structure of RyRp. By using conventional EPR, we also characterized the dynamics of the peptide and showed that there was an increasing gradient of dynamics from the N-terminal region to the C-terminal region. Most importantly in this work, we discovered a Ca-dependent effect of binding of CaM to RyRp. By detecting the rotational dynamics of TOAC at various location of RyRp, we were able to propose a structural binding model in which Ca caused further immobilization of the C-terminal region of the peptide (bound by N-lobe of CaM). Interestingly, the N-terminal region of RyRp (bound by C-lobe of CaM) was less significantly affected by Ca. Thus, we proposed that Ca functions to increase interaction of the N-lobe of CaM with RyR to decrease the activity of the Ca channel.

In chapter 5, our aims were two-fold: 1) to obtain structural measurement of the CaM/RyRp complex as a function of Ca binding and 2) demonstrate the power of bifunctional spin labels BSL compared to its monofunctional counterpart. In this work,

we labeled CaM with two BSL (one in each lobe) and performed DEER distance measurement as a function of RyRp and Ca binding. The first challenge was finding suitable BSL sites on CaM, as CaM is a relatively small protein with limit ideal locations for spin labeling. We demonstrate that if BSL were placed at positions 34.38 in the N-lobe and 106.110 in the C-lobe, we could use DEER to resolve the relevant structures of CaM (open, closed and compact) as each of them gave unique distances between the spin labels. Consistent with this, our DEER measurement revealed a drastic effect of Ca on the distance distribution, which corresponds to direct structural change. In the absence of Ca, apoCaM is in dynamic equilibrium between a predominant closed state and a minor compact state. Upon addition of Ca, the population rearranges and we observed formation of a third open state at longer distance. Interestingly, we showed that the effect of RyRp binding to CaM is greatest when Ca was present where addition of unlabeled RyRp shifted the equilibrium completely towards the compact state, consistent with the crystal structure of the CaCaM/RyRp complex. We also measure the distance between each of the BSL's on CaM and TOAC on RyRp, which to our knowledge, is the first time both spin labels have been used to measure the same protein system. These measurements allowed us to refine our previously proposed model where Ca induces complete binding of the N-lobe of CaM to RyR. Thus, we have obtained direct structural evidence to suggest that a structural change in the CaM-RyR is responsible for the inhibitory effect of Ca on channel activity. More specifically, our structural data support the hypothesis that CaM functions as a subunit of RyR through binding of the C-lobe, and complete interaction of the N-lobe of CaM (in response to increased cytosolic Ca levels) is responsible for max inhibition of RyR.

6.2 PATHOLOGICAL MUTATIONS AND OXIDATION OF CALMODULIN

As mentioned at the beginning, the cycling of Ca between the SR and cytosol is essential to the processes of muscle contraction and relaxation which are largely regulated by RyR and SERCA, respectively. One hallmark of heart diseases is the so-called SR Ca "leak" through the RyR, where Ca is released from the SR in an untimely and unregulated fashion. This results in increased resting cytosolic Ca concentration giving rise to disease conditions. Given this, the RyR channel is now a leading therapeutic target to prevent these often deadly diseases and restore normal Ca handling. One can imagine that perturbations to the RyR can result in such conditions, since it is the main protein involved in release Ca. However, more recently, mutations in CaM have been found in arrhythmia patients [41, 120-122], reiterating the importance of this small protein. The next logical step of this project would be to repeat the structural measurements presented here on these disease-causing CaM mutants and see how they compare to the healthy states.

Protein oxidation is inevitable in metabolic and aerobic respiratory processes but rapid accumulation of reactive oxygen species has been implicated in aging [123-125] and some pathological conditions [123, 126]. Oxidative damage of proteins can lead to structural perturbations with serious adverse molecular and physiological consequences. For example, actin-activated myosin ATPase activity is inhibited by peroxide treatment [127], resulting in slowing of muscle movement and losses of muscle mass and contractile force [125]. Methionine oxidation and subsequent reduction by methionine sulfoxide reductase have implications in metabolic, cardiovascular, neurological and other types of dysfunctions [128-130]. CaM is an oxidatively sensitive Ca regulatory

protein that contains 9 methionine residues, an unusually high percentage (6%) compared to the average protein [131]. All 9 methionine residues are vulnerable to oxidation to methionine sulfoxide, and CaM contains no cysteines, making CaM an ideal model for studying methionine oxidation. The CaM/RyRp complex crystal structure reveals that the residues Trp3620 and Phe3636 on RyRp serve as hydrophobic anchors and make extensive contact with multiple methionine residues on CaM [30]. Oxidation of all methionine residues on CaM eliminated binding with RyRp, and incomplete oxidation decreased binding affinity [38]. Thus, studying CaM oxidation not only has relevance in the general field of protein methionine oxidation, but CaM-mediated RyR regulation as well.

BIBLIOGRAPHY

1. Bers, D.M. 2002. Cardiac excitation-contraction coupling. *Nature*. 415: 198-205.
2. Chin, D., and A.R. Means. 2000. Calmodulin: a prototypical calcium sensor. *Trends Cell Biol*. 10: 322-328.
3. Chattopadhyaya, R., W.E. Meador, A.R. Means, and F.A. Quiocho. 1992. Calmodulin structure refined at 1.7 A resolution. *Journal of molecular biology*. 228: 1177-1192.
4. Kuboniwa, H., N. Tjandra, S. Grzesiek, H. Ren, C.B. Klee, and A. Bax. 1995. Solution structure of calcium-free calmodulin. *Nat Struct Biol*. 2: 768-776.
5. Babu, Y.S., J.S. Sack, T.J. Greenhough, C.E. Bugg, A.R. Means, and W.J. Cook. 1985. Three-dimensional structure of calmodulin. *Nature*. 315: 37-40.
6. Barbato, G., M. Ikura, L.E. Kay, R.W. Pastor, and A. Bax. 1992. Backbone dynamics of calmodulin studied by 15N relaxation using inverse detected two-dimensional NMR spectroscopy: the central helix is flexible. *Biochemistry*. 31: 5269-5278.
7. Wilson, M.A., and A.T. Brunger. 2000. The 1.0 A crystal structure of Ca(2+)-bound calmodulin: an analysis of disorder and implications for functionally relevant plasticity. *J Mol Biol*. 301: 1237-1256.
8. Chou, J.J., S. Li, C.B. Klee, and A. Bax. 2001. Solution structure of Ca(2+)-calmodulin reveals flexible hand-like properties of its domains. *Nature structural biology*. 8: 990-997.
9. Wang, B., S.R. Martin, R.A. Newman, S.L. Hamilton, M.A. Shea, P.M. Bayley, and K.M. Beckingham. 2004. Biochemical properties of V91G calmodulin: A calmodulin point mutation that deregulates muscle contraction in Drosophila. *Protein Sci*. 13: 3285-3297. PMCPMC2287309.
10. Ikura, M., S. Spera, G. Barbato, L.E. Kay, M. Krinks, and A. Bax. 1991. Secondary structure and side-chain 1H and 13C resonance assignments of calmodulin in solution by heteronuclear multidimensional NMR spectroscopy. *Biochemistry*. 30: 9216-9228.
11. van der Spoel, D., B.L. de Groot, S. Hayward, H.J. Berendsen, and H.J. Vogel. 1996. Bending of the calmodulin central helix: a theoretical study. *Protein Sci*. 5: 2044-2053. PMCPMC2143272.
12. Yang, C., G.S. Jas, and K. Kuczera. 2001. Structure and dynamics of calcium-activated calmodulin in solution. *J Biomol Struct Dyn*. 19: 247-271.
13. Crivici, A., and M. Ikura. 1995. Molecular and structural basis of target recognition by calmodulin. *Annual review of biophysics and biomolecular structure*. 24: 85-116.
14. Zalk, R., O.B. Clarke, A. des Georges, R.A. Grassucci, S. Reiken, F. Mancia, W.A. Hendrickson, J. Frank, and A.R. Marks. 2015. Structure of a mammalian ryanodine receptor. *Nature*. 517: 44-49. PMCPMC4300236.
15. Samso, M., and T. Wagenknecht. 2002. Apocalmodulin and Ca2+-calmodulin bind to neighboring locations on the ryanodine receptor. *J Biol Chem*. 277: 1349-1353.
16. Ludtke, S.J., Serysheva, II, S.L. Hamilton, and W. Chiu. 2005. The pore structure of the closed RyR1 channel. *Structure*. 13: 1203-1211. PMCPMC2983469.

17. Samso, M., T. Wagenknecht, and P.D. Allen. 2005. Internal structure and visualization of transmembrane domains of the RyR1 calcium release channel by cryo-EM. *Nat Struct Mol Biol*. 12: 539-544. PMCPMC1925259.
18. Yan, Z., X. Bai, C. Yan, J. Wu, Z. Li, T. Xie, W. Peng, C. Yin, X. Li, S.H.W. Scheres, Y. Shi, and N. Yan. 2015. Structure of the rabbit ryanodine receptor RyR1 at near-atomic resolution. *Nature*. 517: 50-55. PMCPMC4338550.
19. Peng, W., H. Shen, J. Wu, W. Guo, X. Pan, R. Wang, S.R. Chen, and N. Yan. 2016. Structural basis for the gating mechanism of the type 2 ryanodine receptor RyR2. *Science*. 354.
20. Yang, H.C., M.M. Reedy, C.L. Burke, and G.M. Strasburg. 1994. Calmodulin interaction with the skeletal muscle sarcoplasmic reticulum calcium channel protein. *Biochemistry*. 33: 518-525.
21. Tripathy, A., L. Xu, G. Mann, and G. Meissner. 1995. Calmodulin activation and inhibition of skeletal muscle Ca2+ release channel (ryanodine receptor). *Biophys J*. 69: 106-119. PMCPMC1236229.
22. Moore, C.P., G. Rodney, J.Z. Zhang, L. Santacruz-Toloza, G. Strasburg, and S.L. Hamilton. 1999. Apocalmodulin and Ca2+ calmodulin bind to the same region on the skeletal muscle Ca2+ release channel. *Biochemistry*. 38: 8532-8537.
23. Fruen, B.R., J.M. Bardy, T.M. Byrem, G.M. Strasburg, and C.F. Louis. 2000. Differential Ca(2+) sensitivity of skeletal and cardiac muscle ryanodine receptors in the presence of calmodulin. *Am J Physiol Cell Physiol*. 279: C724-733.
24. Balshaw, D.M., L. Xu, N. Yamaguchi, D.A. Pasek, and G. Meissner. 2001. Calmodulin binding and inhibition of cardiac muscle calcium release channel (ryanodine receptor). *J Biol Chem*. 276: 20144-20153.
25. Buratti, R., G. Prestipino, P. Menegazzi, S. Treves, and F. Zorzato. 1995. Calcium dependent activation of skeletal muscle Ca2+ release channel (ryanodine receptor) by calmodulin. *Biochem Biophys Res Commun*. 213: 1082-1090.
26. Ikemoto, T., M. Iino, and M. Endo. 1995. Enhancing effect of calmodulin on Ca(2+)-induced Ca2+ release in the sarcoplasmic reticulum of rabbit skeletal muscle fibres. *J Physiol*. 487 (Pt 3): 573-582. PMCPMC1156646.
27. Meissner, G. 1994. Ryanodine receptor/Ca2+ release channels and their regulation by endogenous effectors. *Annu Rev Physiol*. 56: 485-508.
28. Rodney, G.G., B.Y. Williams, G.M. Strasburg, K. Beckingham, and S.L. Hamilton. 2000. Regulation of RYR1 activity by Ca(2+) and calmodulin. *Biochemistry*. 39: 7807-7812.
29. Rodney, G.G., C.P. Moore, B.Y. Williams, J.Z. Zhang, J. Krol, S.E. Pedersen, and S.L. Hamilton. 2001. Calcium binding to calmodulin leads to an N-terminal shift in its binding site on the ryanodine Receptor. *The Journal of biological chemistry*. 276: 2069-2074.
30. Maximciuc, A.A., J.A. Putkey, Y. Shamoo, and K.R. Mackenzie. 2006. Complex of calmodulin with a ryanodine receptor target reveals a novel, flexible binding mode. *Structure*. 14: 1547-1556.
31. Yamaguchi, N., C. Xin, and G. Meissner. 2001. Identification of apocalmodulin and Ca2+-calmodulin regulatory domain in skeletal muscle Ca2+ release channel, ryanodine receptor. *The Journal of biological chemistry*. 276: 22579-22585.

32. Yamaguchi, N., L. Xu, D.A. Pasek, K.E. Evans, and G. Meissner. 2003. Molecular basis of calmodulin binding to cardiac muscle Ca(2+) release channel (ryanodine receptor). *The Journal of biological chemistry*. 278: 23480-23486.
33. Meador, W.E., A.R. Means, and F.A. Quiocho. 1992. Target enzyme recognition by calmodulin: 2.4 A structure of a calmodulin-peptide complex. *Science*. 257: 1251-1255.
34. Fill, M., and J.A. Copello. 2002. Ryanodine receptor calcium release channels. *Physiological reviews*. 82: 893-922.
35. Tripathy, A., L. Xu, G. Mann, and G. Meissner. 1995. Calmodulin activation and inhibition of skeletal muscle Ca2+ release channel (ryanodine receptor). *Biophysical journal*. 69: 106-119. PMC1236229.
36. Meissner, G., and J.S. Henderson. 1987. Rapid calcium release from cardiac sarcoplasmic reticulum vesicles is dependent on Ca2+ and is modulated by Mg2+, adenine nucleotide, and calmodulin. *The Journal of biological chemistry*. 262: 3065-3073.
37. Fruen, B.R., J.M. Bardy, T.M. Byrem, G.M. Strasburg, and C.F. Louis. 2000. Differential Ca(2+) sensitivity of skeletal and cardiac muscle ryanodine receptors in the presence of calmodulin. *American journal of physiology. Cell physiology*. 279: C724-733.
38. Balog, E.M., L.E. Norton, R.A. Bloomquist, R.L. Cornea, D.J. Black, C.F. Louis, D.D. Thomas, and B.R. Fruen. 2003. Calmodulin oxidation and methionine to glutamine substitutions reveal methionine residues critical for functional interaction with ryanodine receptor-1. *The Journal of biological chemistry*. 278: 15615-15621.
39. McCarthy, M.R., A.R. Thompson, F. Nitu, R.J. Moen, M.J. Olenek, J.C. Klein, and D.D. Thomas. 2015. Impact of methionine oxidation on calmodulin structural dynamics. *Biochemical and biophysical research communications*. 456: 567-572.
40. Xu, X., M. Yano, H. Uchinoumi, A. Hino, T. Suetomi, M. Ono, H. Tateishi, T. Oda, S. Okuda, M. Doi, S. Kobayashi, T. Yamamoto, Y. Ikeda, N. Ikemoto, and M. Matsuzaki. 2010. Defective calmodulin binding to the cardiac ryanodine receptor plays a key role in CPVT-associated channel dysfunction. *Biochemical and biophysical research communications*. 394: 660-666. PMC2858291.
41. Nyegaard, M., M.T. Overgaard, M.T. Sondergaard, M. Vranas, E.R. Behr, L.L. Hildebrandt, J. Lund, P.L. Hedley, A.J. Camm, G. Wettrell, I. Fosdal, M. Christiansen, and A.D. Borglum. 2012. Mutations in calmodulin cause ventricular tachycardia and sudden cardiac death. *American journal of human genetics*. 91: 703-712. PMC3484646.
42. Newman, R.A., B.R. Sorensen, A.M. Kilpatrick, and M.A. Shea. 2014. Calcium-dependent energetics of calmodulin domain interactions with regulatory regions of the Ryanodine Receptor Type 1 (RyR1). *Biophysical chemistry*. 193-194: 35-49. PMC4208696.
43. Lau, K., M.M. Chan, and F. Van Petegem. 2014. Lobe-specific calmodulin binding to different ryanodine receptor isoforms. *Biochemistry*. 53: 932-946.
44. Porter Moore, C., J.Z. Zhang, and S.L. Hamilton. 1999. A role for cysteine 3635 of RYR1 in redox modulation and calmodulin binding. *The Journal of biological chemistry*. 274: 36831-36834.

45. Boschek, C.B., H. Sun, D.J. Bigelow, and T.C. Squier. 2008. Different conformational switches underlie the calmodulin-dependent modulation of calcium pumps and channels. *Biochemistry*. 47: 1640-1651.
46. Karim, C.B., T.L. Kirby, Z. Zhang, Y. Nesmelov, and D.D. Thomas. 2004. Phospholamban structural dynamics in lipid bilayers probed by a spin label rigidly coupled to the peptide backbone. *Proc Natl Acad Sci U S A*. 101: 14437-14442.
47. Karim, C.B., Z. Zhang, E.C. Howard, K.D. Torgersen, and D.D. Thomas. 2006. Phosphorylation-dependent Conformational Switch in Spin-labeled Phospholamban Bound to SERCA. *J Mol Biol*. 358: 1032-1040.
48. Karim, C.B., L.M. Espinoza-Fonseca, Z.M. James, E.A. Hanse, J.S. Gaynes, D.D. Thomas, and A. Kelekar. 2015. Structural Mechanism for Regulation of Bcl-2 protein Noxa by phosphorylation. *Scientific reports*. 5: 14557. PMC4585961.
49. Sheppard, R. 2003. The fluorenylmethoxycarbonyl group in solid phase synthesis. *Journal of peptide science : an official publication of the European Peptide Society*. 9: 545-552.
50. Toniolo, C., E. Valente, F. Formaggio, M. Crisma, G. Pilloni, C. Corvaja, A. Toffoletti, G.V. Martinez, M.P. Hanson, G.L. Millhauser, and et al. 1995. Synthesis and conformational studies of peptides containing TOAC, a spin-labelled C alpha, alpha-disubstituted glycine. *J Pept Sci*. 1: 45-57.
51. Monaco, V., F. Formaggio, M. Crisma, C. Toniolo, P. Hanson, G. Millhauser, C. George, J.R. Deschamps, and J.L. Flippen-Anderson. 1999. Determining the occurrence of a 3(10)-helix and an alpha-helix in two different segments of a lipopeptaibol antibiotic using TOAC, a nitroxide spin-labeled C(alpha)-tetrasubstituted alpha-aminoacid. *Bioorg Med Chem*. 7: 119-131.
52. Karim, C.B., Z. Zhang, and D.D. Thomas. 2007. Synthesis of TOAC spin-labeled proteins and reconstitution in lipid membranes. *Nat Protoc*. 2: 42-49.
53. Fields, G.B., and R.L. Noble. 1990. Solid phase peptide synthesis utilizing 9-fluorenylmethoxycarbonyl amino acids. *International journal of peptide and protein research*. 35: 161-214.
54. Ferrer, M., C. Woodward, and G. Barany. 1992. Solid-phase synthesis of bovine pancreatic trypsin inhibitor (BPTI) and two analogues. A chemical approach for evaluating the role of disulfide bridges in protein folding and stability. *International journal of peptide and protein research*. 40: 194-207.
55. Karim, C.B., M.G. Paterlini, L.G. Reddy, G.W. Hunter, G. Barany, and D.D. Thomas. 2001. Role of cysteine residues in structural stability and function of a transmembrane helix bundle. *J Biol Chem*. 276: 38814-38819.
56. Andreu, D., F. Albericio, N.A. Sole, M.C. Munson, M. Ferrer, and G. Barany. 1994. Formation of disulfide bonds in synthetic peptides and proteins. *Methods in molecular biology*. 35: 91-169.
57. Sun, J., C. Xin, J.P. Eu, J.S. Stamler, and G. Meissner. 2001. Cysteine-3635 is responsible for skeletal muscle ryanodine receptor modulation by NO. *Proceedings of the National Academy of Sciences of the United States of America*. 98: 11158-11162. PMC58700.
58. Bui, T.T., F. Formaggio, M. Crisma, V. Monaco, C. Toniolo, R. Hussain, and G. Siligardi. 2000. TOAC: a useful C-alpha -tetrasubstituted -amino acid for peptide

conformational analysis by CD spectroscopy in the visible region. *J. Chem. Soc., Perkin Trans.* 2: 1043-1046.
59. McNulty, J.C., D.A. Thompson, M.R. Carrasco, and G.L. Millhauser. 2002. Dap-SL: a new site-directed nitroxide spin labeling approach for determining structure and motions in synthesized peptides and proteins. *FEBS Lett*. 529: 243-248.
60. Schreier, S., J.C. Bozelli, Jr., N. Marin, R.F. Vieira, and C.R. Nakaie. 2012. The spin label amino acid TOAC and its uses in studies of peptides: chemical, physicochemical, spectroscopic, and conformational aspects. *Biophysical reviews*. 4: 45-66. PMC3271205.
61. King, D.S., C.G. Fields, and G.B. Fields. 1990. A cleavage method which minimizes side reactions following Fmoc solid phase peptide synthesis. *International journal of peptide and protein research*. 36: 255-266.
62. Balog, E.M., E.L. Lockamy, D.D. Thomas, and D.A. Ferrington. 2009. Site-specific methionine oxidation initiates calmodulin degradation by the 20S proteasome. *Biochemistry*. 48: 3005-3016. PMC3664458.
63. Tsien, R., and T. Pozzan. 1989. Measurement of cytosolic free Ca2+ with quin2. *Methods in enzymology*. 172: 230-262.
64. Keith, A., G. Bulfield, and W. Snipes. 1970. Spin-labeled Neurospora mitochondria. *Biophysical journal*. 10: 618-629. PMC1367786.
65. Goldman, S.A., G.V. Bruno, and J.H. Freed. 1972. Estimating slow-motional rotational correlation times for nitroxides by electron spin resonance. *J Phys Chem*. 76: 1858-1860.
66. Durer, Z.A., D.S. Kudryashov, M.R. Sawaya, C. Altenbach, W. Hubbell, and E. Reisler. 2012. Structural states and dynamics of the D-loop in actin. *Biophysical journal*. 103: 930-939. PMC3433612.
67. Adler, A.J., N.J. Greenfield, and G.D. Fasman. 1973. Circular dichroism and optical rotatory dispersion of proteins and polypeptides. *Methods in enzymology*. 27: 675-735.
68. Lockwood, N.A., R.S. Tu, Z. Zhang, M.V. Tirrell, D.D. Thomas, and C.B. Karim. 2003. Structure and function of integral membrane protein domains resolved by peptide-amphiphiles: application to phospholamban. *Biopolymers*. 69: 283-292.
69. Shiraki, K., K. Nishikawa, and Y. Goto. 1995. Trifluoroethanol-induced stabilization of the alpha-helical structure of beta-lactoglobulin: implication for non-hierarchical protein folding. *Journal of molecular biology*. 245: 180-194.
70. Palepu, R., and J. Clarke. 1989. Viscosities and densities of 2,2,2-trifluoroethanol + water at various temperatures. *Thermochimica Acta*. 156: 359-363.
71. Xiong, L.W., R.A. Newman, G.G. Rodney, O. Thomas, J.Z. Zhang, A. Persechini, M.A. Shea, and S.L. Hamilton. 2002. Lobe-dependent regulation of ryanodine receptor type 1 by calmodulin. *J Biol Chem*. 277: 40862-40870.
72. Newman, R.A., B.R. Sorensen, A.M. Kilpatrick, and M.A. Shea. 2014. Calcium-dependent energetics of calmodulin domain interactions with regulatory regions of the Ryanodine Receptor Type 1 (RyR1). *Biophys Chem*. 193-194: 35-49. PMCPMC4208696.
73. Zhang, H., J.Z. Zhang, C.I. Danila, and S.L. Hamilton. 2003. A noncontiguous, intersubunit binding site for calmodulin on the skeletal muscle Ca2+ release channel. *J Biol Chem*. 278: 8348-8355.

74. Huang, X., Y. Liu, R. Wang, X. Zhong, A. Koop, S.R. Chen, T. Wagenknecht, and Z. Liu. 2013. Two potential calmodulin-binding sequences in the ryanodine receptor contribute to a mobile, intra-subunit calmodulin-binding domain. *J Cell Sci*. 126: 4527-4535. PMCPMC3784825.
75. Sondergaard, M.T., A.B. Sorensen, L.L. Skov, K. Kjaer-Sorensen, M.C. Bauer, M. Nyegaard, S. Linse, C. Oxvig, and M.T. Overgaard. 2014. Calmodulin mutations causing catecholaminergic polymorphic ventricular tachycardia confer opposing functional and biophysical molecular changes. *The FEBS journal*.
76. Binder, B.P., S. Cornea, A.R. Thompson, R.J. Moen, and D.D. Thomas. 2015. High-resolution helix orientation in actin-bound myosin determined with a bifunctional spin label. *Proceedings of the National Academy of Sciences of the United States of America*.
77. Kuboniwa, H., N. Tjandra, S. Grzesiek, H. Ren, C.B. Klee, and A. Bax. 1995. Solution structure of calcium-free calmodulin. *Nature structural biology*. 2: 768-776.
78. Fill, M., and J.A. Copello. 2002. Ryanodine receptor calcium release channels. *Physiol Rev*. 82: 893-922.
79. Fallon, J.L., and F.A. Quiocho. 2003. A closed compact structure of native Ca(2+)-calmodulin. *Structure*. 11: 1303-1307.
80. Finn, B.E., J. Evenas, T. Drakenberg, J.P. Waltho, E. Thulin, and S. Forsen. 1995. Calcium-induced structural changes and domain autonomy in calmodulin. *Nature structural biology*. 2: 777-783.
81. Zhang, M., T. Tanaka, and M. Ikura. 1995. Calcium-induced conformational transition revealed by the solution structure of apo calmodulin. *Nature structural biology*. 2: 758-767.
82. Forsen, S., S. Linse, T. Drakenberg, J. Kordel, M. Akke, P. Sellers, C. Johansson, E. Thulin, I. Andersson, P. Brodin, and et al. 1991. Ca2+ binding in proteins of the calmodulin superfamily: cooperativity, electrostatic contributions and molecular mechanisms. *Ciba Foundation symposium*. 161: 222-236.
83. Linse, S., and S. Forsen. 1995. Determinants that govern high-affinity calcium binding. *Advances in second messenger and phosphoprotein research*. 30: 89-151.
84. Malmendal, A., J. Evenas, S. Forsen, and M. Akke. 1999. Structural dynamics in the C-terminal domain of calmodulin at low calcium levels. *Journal of molecular biology*. 293: 883-899.
85. Evenas, J., A. Malmendal, and M. Akke. 2001. Dynamics of the transition between open and closed conformations in a calmodulin C-terminal domain mutant. *Structure*. 9: 185-195.
86. Lin, A.Y., E. Prochniewicz, Z. James, B. Svensonn, and D.D. Thomas. 2011. Large-scale opening of utrophin's tandem CH domains upon actin binding, by an induced-fit mechanism. *Proc Natl Acad Sci U S A*: accepted.
87. Kast, D., L.M. Espinoza-Fonseca, C. Yi, and D.D. Thomas. 2010. Phosphorylation-induced structural changes in smooth muscle myosin regulatory light chain. *Proc Natl Acad Sci U S A*. 107: 8207-8212.
88. Karim, C.B., T.L. Kirby, Z. Zhang, Y. Nesmelov, and D.D. Thomas. 2004. Phospholamban structural dynamics in lipid bilayers probed by a spin label

rigidly coupled to the peptide backbone. *Proceedings of the National Academy of Sciences of the United States of America*. 101: 14437-14442. PMC521948.
89. Karim, C.B., Z. Zhang, and D.D. Thomas. 2007. Synthesis of TOAC spin-labeled proteins and reconstitution in lipid membranes. *Nature protocols*. 2: 42-49.
90. Toniolo, C., E. Valente, F. Formaggio, M. Crisma, G. Pilloni, C. Corvaja, A. Toffoletti, G.V. Martinez, M.P. Hanson, G.L. Millhauser, and et al. 1995. Synthesis and conformational studies of peptides containing TOAC, a spin-labelled C alpha, alpha-disubstituted glycine. *J Pept Sci*. 1: 45-57.
91. Her, C., J.E. McCaffrey, D.D. Thomas, and C.B. Karim. 2016. Calcium-Dependent Structural Dynamics of a Spin-Labeled RyR Peptide Bound to Calmodulin. *Biophys J*. 111: 2387-2394. PMC5154373.
92. Losel, R.M., R. Philipp, T. Kalai, K. Hideg, and W.E. Trommer. 1999. Synthesis and application of novel bifunctional spin labels. *Bioconjugate chemistry*. 10: 578-582.
93. Fleissner, M.R., M.D. Bridges, E.K. Brooks, D. Cascio, T. Kalai, K. Hideg, and W.L. Hubbell. 2011. Structure and dynamics of a conformationally constrained nitroxide side chain and applications in EPR spectroscopy. *Proceedings of the National Academy of Sciences of the United States of America*. 108: 16241-16246. PMC3182725.
94. Thompson, A.R., B.P. Binder, J.E. McCaffrey, B. Svensson, and D.D. Thomas. 2015. Bifunctional Spin Labeling of Muscle Proteins: Accurate Rotational Dynamics, Orientation, and Distance by EPR. *Methods in enzymology*. 564: 101-123.
95. Schmidt, T., M.A. Walti, J.L. Baber, E.J. Hustedt, and G.M. Clore. 2016. Long distance measurements up to 160 Å in the GroEL tetradecamer using Q-band DEER EPR spectroscopy. *Angewandte Chemie International Edition*. 55: 15905-15909.
96. Pannier, M., S. Veit, A. Godt, G. Jeschke, and H.W. Spiess. 2000. Dead-time free measurement of dipole-dipole interactions between electron spins. *Journal of magnetic resonance*. 142: 331-340.
97. Jeschke, G. 2012. DEER distance measurements on proteins. *Annual review of physical chemistry*. 63: 419-446.
98. Rabenstein, M.D., and Y.K. Shin. 1995. Determination of the distance between two spin labels attached to a macromolecule. *Proceedings of the National Academy of Sciences of the United States of America*. 92: 8239-8243. PMC41132.
99. Henzler-Wildman, K., and D. Kern. 2007. Dynamic personalities of proteins. *Nature*. 450: 964-972.
100. Zhang, Z., H.A. Remmer, D.D. Thomas, and C.B. Karim. 2007. Backbone dynamics determined by electron paramagnetic resonance to optimize solid-phase peptide synthesis of TOAC-labeled phospholamban. *Biopolymers*. 88: 29-35.
101. McCaffrey, J.E., Z.M. James, B. Svensson, B.P. Binder, and D.D. Thomas. 2015. A bifunctional spin label reports the structural topology of phospholamban in magnetically-aligned bicelles. *Journal of magnetic resonance*. 262: 50-56.
102. Thomas, D.D. 1978. Large-scale rotational motions of proteins detected by electron paramagnetic resonance and fluorescence. *Biophys J*. 24: 439-462.

103. Gsponer, J., J. Christodoulou, A. Cavalli, J.M. Bui, B. Richter, C.M. Dobson, and M. Vendruscolo. 2008. A coupled equilibrium shift mechanism in calmodulin-mediated signal transduction. *Structure*. 16: 736-746. PMCPMC2428103.
104. Hoang, J., and R.S. Prosser. 2014. Conformational selection and functional dynamics of calmodulin: a (19)F nuclear magnetic resonance study. *Biochemistry*. 53: 5727-5736.
105. Erwin, N., S. Patra, and R. Winter. 2016. Probing conformational and functional substates of calmodulin by high pressure FTIR spectroscopy: influence of Ca2+ binding and the hypervariable region of K-Ras4B. *Physical chemistry chemical physics : PCCP*. 18: 30020-30028.
106. Banham, J.E., C.M. Baker, S. Ceola, I.J. Day, G.H. Grant, E.J. Groenen, C.T. Rodgers, G. Jeschke, and C.R. Timmel. 2008. Distance measurements in the borderline region of applicability of CW EPR and DEER: a model study on a homologous series of spin-labelled peptides. *J Magn Reson*. 191: 202-218.
107. Tidow, H., and P. Nissen. 2013. Structural diversity of calmodulin binding to its target sites. *FEBS J*. 280: 5551-5565.
108. Boschek, C.B., T.E. Jones, T.C. Squier, and D.J. Bigelow. 2007. Calcium occupancy of N-terminal sites within calmodulin induces inhibition of the ryanodine receptor calcium release channel. *Biochemistry*. 46: 10621-10628.
109. Wang, S., S.E. George, J.P. Davis, and J.D. Johnson. 1998. Structural determinants of Ca2+ exchange and affinity in the C terminal of cardiac troponin C. *Biochemistry*. 37: 14539-14544.
110. Gopalakrishna, R., and W.B. Anderson. 1982. Ca2+-induced hydrophobic site on calmodulin: application for purification of calmodulin by phenyl-Sepharose affinity chromatography. *Biochemical and biophysical research communications*. 104: 830-836.
111. Fruen, B.R., E.M. Balog, J. Schafer, F.R. Nitu, D.D. Thomas, and R.L. Cornea. 2005. Direct detection of calmodulin tuning by ryanodine receptor channel targets using a Ca2+-sensitive acrylodan-labeled calmodulin. *Biochemistry*. 44: 278-284.
112. Kirby, T.L., C.B. Karim, and D.D. Thomas. 2004. Electron paramagnetic resonance reveals a large-scale conformational change in the cytoplasmic domain of phospholamban upon binding to the sarcoplasmic reticulum Ca-ATPase. *Biochemistry*. 43: 5842-5852.
113. Adler, A.J., N.J. Greenfield, and G.D. Fasman. 1973. Circular dichroism and optical rotatory dispersion of proteins and polypeptides. *Methods Enzymol*. 27: 675-735.
114. Jeschke, G., V. Chechek, P. Ionita, A. Godt, H. Zimmermann, J.E. Banham, C.R. Timmel, D. Hilger, and H. Jung. 2006. DeerAnalysis 2006 - a Comprehensive Software Package for Analyzing Pulsed ELDOR Data. *Appl. Magn. Reson.* 30: 473-498.
115. Sen, K.I., T.M. Logan, and P.G. Fajer. 2007. Protein dynamics and monomer-monomer interactions in AntR activation by electron paramagnetic resonance and double electron-electron resonance. *Biochemistry*. 46: 11639-11649.
116. Edwards, T.H., and S. Stoll. 2016. A Bayesian approach to quantifying uncertainty from experimental noise in DEER spectroscopy. *Journal of magnetic resonance*. 270: 87-97. PMCPMC4996738.
117. Priestley, M.B. 1981. Spectral Analysis and Time Series. 375.

118. Stein, R.A., A.H. Beth, and E.J. Hustedt. 2015. A Straightforward Approach to the Analysis of Double Electron-Electron Resonance Data. *Methods in enzymology*. 563: 531-567. PMCPMC5231402.
119. Klein, J.C., A.R. Burr, B. Svensson, D.J. Kennedy, J. Allingham, M.A. Titus, I. Rayment, and D.D. Thomas. 2008. Actin-binding cleft closure in myosin II probed by site-directed spin labeling and pulsed EPR. *Proceedings of the National Academy of Sciences of the United States of America*. 105: 12867-12872. PMC2529091.
120. Crotti, L., C.N. Johnson, E. Graf, G.M. De Ferrari, B.F. Cuneo, M. Ovadia, J. Papagiannis, M.D. Feldkamp, S.G. Rathi, J.D. Kunic, M. Pedrazzini, T. Wieland, P. Lichtner, B.M. Beckmann, T. Clark, C. Shaffer, D.W. Benson, S. Kaab, T. Meitinger, T.M. Strom, W.J. Chazin, P.J. Schwartz, and A.L. George, Jr. 2013. Calmodulin mutations associated with recurrent cardiac arrest in infants. *Circulation*. 127: 1009-1017. PMCPMC3834768.
121. Hwang, H.S., F.R. Nitu, Y. Yang, K. Walweel, L. Pereira, C.N. Johnson, M. Faggioni, W.J. Chazin, D. Laver, A.L. George, Jr., R.L. Cornea, D.M. Bers, and B.C. Knollmann. 2014. Divergent regulation of ryanodine receptor 2 calcium release channels by arrhythmogenic human calmodulin missense mutants. *Circ Res*. 114: 1114-1124. PMCPMC3990285.
122. Yang, Y., T. Guo, T. Oda, A. Chakraborty, L. Chen, H. Uchinoumi, A.A. Knowlton, B.R. Fruen, R.L. Cornea, G. Meissner, and D.M. Bers. 2014. Cardiac myocyte Z-line calmodulin is mainly RyR2-bound, and reduction is arrhythmogenic and occurs in heart failure. *Circ Res*. 114: 295-306. PMCPMC4004530.
123. Berlett, B.S., and E.R. Stadtman. 1997. Protein oxidation in aging, disease, and oxidative stress. *The Journal of biological chemistry*. 272: 20313-20316.
124. Stadtman, E.R. 2006. Protein oxidation and aging. *Free radical research*. 40: 1250-1258.
125. Moen, R.J., J.C. Klein, and D.D. Thomas. 2014. Electron paramagnetic resonance resolves effects of oxidative stress on muscle proteins. *Exercise and sport sciences reviews*. 42: 30-36. PMC3934098.
126. Baraibar, M.A., L. Liu, E.K. Ahmed, and B. Friguet. 2012. Protein oxidative damage at the crossroads of cellular senescence, aging, and age-related diseases. *Oxidative medicine and cellular longevity*. 2012: 919832. PMC3483731.
127. Klein, J.C., R.J. Moen, E.A. Smith, M.A. Titus, and D.D. Thomas. 2011. Structural and functional impact of site-directed methionine oxidation in myosin. *Biochemistry*. 50: 10318-10327. PMC3228272.
128. Bigelow, D.J., and T.C. Squier. 2011. Thioredoxin-dependent redox regulation of cellular signaling and stress response through reversible oxidation of methionines. *Mol Biosyst*. 7: 2101-2109.
129. Cui, Z.J., Z.Q. Han, and Z.Y. Li. 2012. Modulating protein activity and cellular function by methionine residue oxidation. *Amino Acids*. 43: 505-517.
130. Kim, G., S.J. Weiss, and R.L. Levine. 2014. Methionine oxidation and reduction in proteins. *Biochim Biophys Acta*. 1840: 901-905. PMCPMC3766491.
131. O'neil, K.T., and W.F. DeGrado. 1990. How calmodulin binds its targets: sequence independent recognition of amphiphilic alpha-helices. *Trends in Biochemical Sciences*. 2: 59-64.